Since 1955

Strojniški vestnik
Journal of Mechanical Engineering

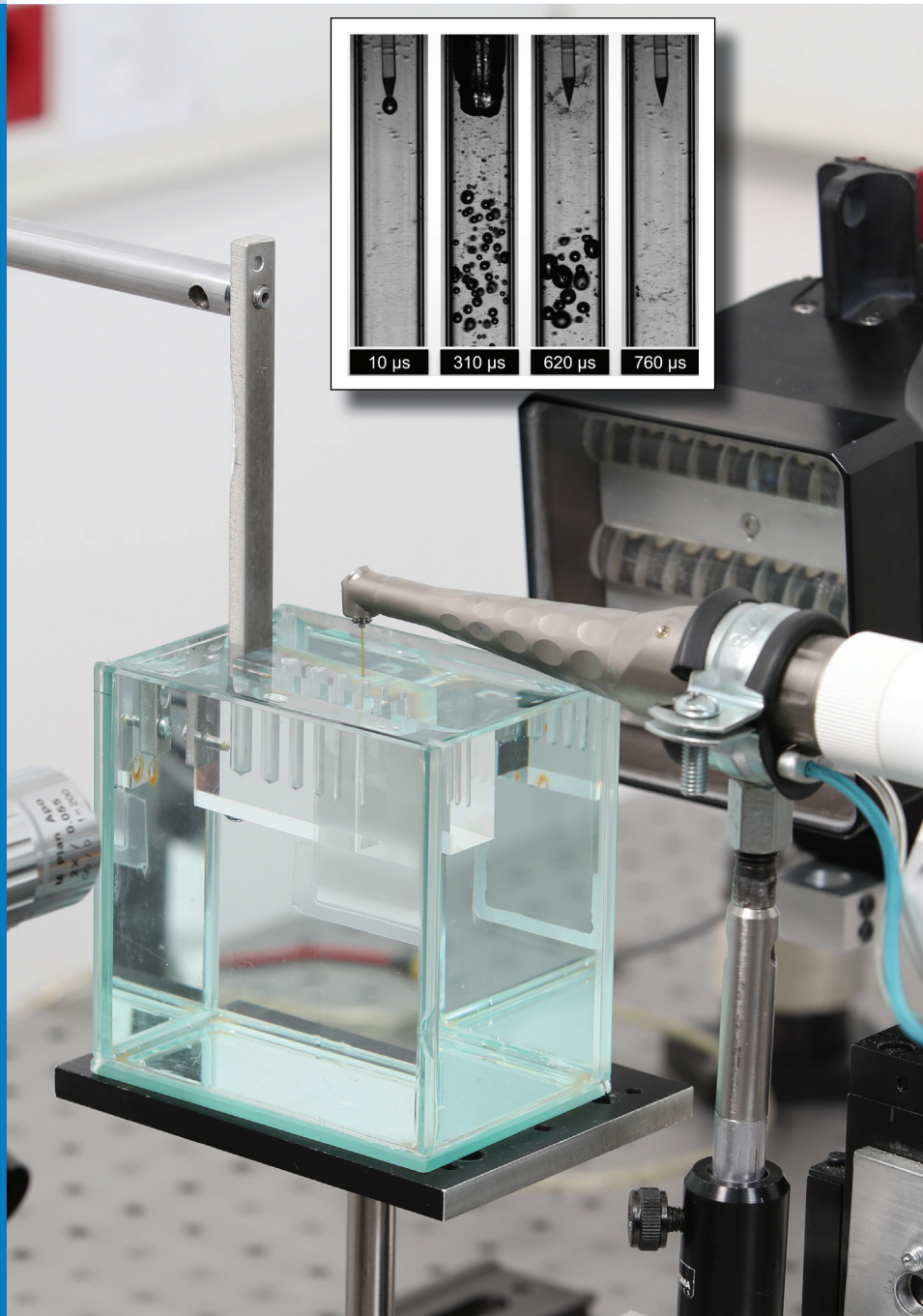

no. 12
year 2022
volume 68

Strojniški vestnik – Journal of Mechanical Engineering (SV-JME)

Aim and Scope
The international journal publishes original and (mini)review articles covering the concepts of materials science, mechanics, kinematics, thermodynamics, energy and environment, mechatronics and robotics, fluid mechanics, tribology, cybernetics, industrial engineering and structural analysis.
The journal follows new trends and progress proven practice in the mechanical engineering and also in the closely related sciences as are electrical, civil and process engineering, medicine, microbiology, ecology, agriculture, transport systems, aviation, and others, thus creating a unique forum for interdisciplinary or multidisciplinary dialogue.
The international conferences selected papers are welcome for publishing as a special issue of SV-JME with invited co-editor(s).

Editorial Office
University of Ljubljana, Faculty of Mechanical Engineering
SV-JME, Aškerčeva 6, SI-1000 Ljubljana, Slovenia
Phone: 386 (0)1 4771 137
Fax: 386 (0)1 2518 567
info@sv-jme.eu, http://www.sv-jme.eu

Print: Demat d.o.o., printed in 250 copies

Founders and Publishers
University of Ljubljana, Faculty of Mechanical Engineering, Slovenia
University of Maribor, Faculty of Mechanical Engineering, Slovenia
Association of Mechanical Engineers of Slovenia
Chamber of Commerce and Industry of Slovenia, Metal Processing Industry Association

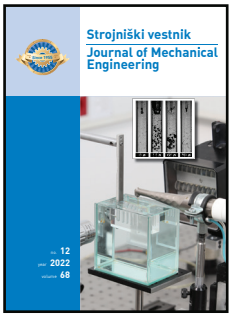

Cover:
The cover image shows an experimental system for studying laser-induced cavitation in a confined volume. Here, an Er:YAG laser is used whose light is very well absorbed in water. The laser light is passed through the fiber tip, where a primary cavitation bubble forms with each pulse, and upon its collapse, secondary cavitation forms throughout the volume. This type of phenomenon is used in biomedical applications to clean and irrigate complex structures, such as root canals.

Image Courtesy:
Laboratory for laser techniques LASTEH, University of Ljubljana, Faculty of Mechanical Engineering, Slovenia

General information
Strojniški vestnik – Journal of Mechanical Engineering is published in 11 issues per year (July and August is a double issue).

Institutional prices include print & online access: institutional subscription price and foreign subscription €100,00 (the price of a single issue is €10,00); general public subscription and student subscription €50,00 (the price of a single issue is €5,00). Prices are exclusive of tax. Delivery is included in the price. The recipient is responsible for paying any import duties or taxes. Legal title passes to the customer on dispatch by our distributor. Single issues from current and recent volumes are available at the current single-issue price. To order the journal, please complete the form on our website. For submissions, subscriptions and all other information please visit: *http://www.sv-jme.eu.*

You can advertise on the inner and outer side of the back cover of the journal. The authors of the published papers are invited to send photos or pictures with short explanation for cover content.

We would like to thank the reviewers who have taken part in the peer-review process.

ISSN 0039-2480, ISSN 2536-2948 (online)

The journal is subsidized by Slovenian Research Agency.

SV-JME is indexed / abstracted in: SCI-Expanded, Compendex, Inspec, ProQuest-CSA, SCOPUS, TEMA. The list of the remaining bases, in which SV-JME is indexed, is available on the website.

Strojniški vestnik - Journal of Mechanical Engineering is available on *https://www.sv-jme.eu*.

Contents

Strojniški vestnik - Journal of Mechanical Engineering
volume 68, (2022), number 12
Ljubljana, December 2022
ISSN 0039-2480

Published monthly

Papers

Strojniški vestnik - Journal of Mechanical Engineering 68(2022)12, 725-734
DOI:10.5545/sv-jme.2022.349
Original Scientific Paper
Received for review: 2022-08-29
Received revised form: 2022-10-26
Accepted for publication: 2022-11-03

Multi-Objective Optimization of the Chebyshev Lambda Mechanism

Daniel Miler* – Dominik Birt – Matija Hoić
University of Zagreb, Faculty of Mechanical Engineering and Naval Architecture, Croatia

Walking mechanisms are a solution for cases in which wheels are not applicable, such as uneven or stepped surfaces and surfaces with obstacles. Furthermore, it is possible to tailor mechanism footpaths to expected working conditions through optimization. Thus, in this paper, a mechanism optimization process was proposed, focusing on single-leg performance. Numerical Simulink calculations were used to determine objective function values, which were then input to a non-dominated sorting genetic algorithm (NSGA-II) for optimization. In each following generation, NSGA-II provided a new set of units for evaluation. The procedure was applied to the single leg of the Chebyshev lambda mechanism to better illustrate it, enabling a comprehensive analysis of candidates. Four objective functions (i.e., length in the x-direction, trajectory height variation, maximum foot acceleration, and foot speed fluctuation) were used to carry out a multi-objective optimization. The calculation time was approximately 2 s/unit.
Keywords: Chebyshev lambda mechanism, optimization, synthesis, walking mechanism

Highlights
- *A procedure for the optimization of walking mechanisms was presented.*
- *Simscape mechanism model was embedded within the NSGA-II; approx. calculation time was 2 s per unit*
- *Four objective functions were used to optimize the Chebyshev lambda mechanism.*
- *The proposed procedure can be applied to other types of walking mechanisms.*

0 INTRODUCTION

Walking mechanisms imitate the leg motion of walking creatures and are comprised of linkages and joints. Despite their shortcomings compared to wheeled drives, including the lower efficiency, stride height variations, and higher complexity, they are useful in special applications [1]. Walking mechanisms can be used while traversing uneven or stepped surfaces [2] where wheeled mechanisms cannot be used. Also, they are applicable in regular flat surfaces with obstacles [3], e.g., a warehouse with sensitive cables on the floor or propelling devices through water via paddles [4]. Many types of walking mechanisms are available, each with a specific trajectory and number of joints and linkages. Thus, the mechanism type can be selected depending on the desired outputs. Examples include the Chebyshev lambda, Klann, and Jansen mechanisms [5] to [7].

The above-listed mechanisms can be applied in multiple ways, either using the default linkage values or optimizing them for a specific purpose. Komoda and Wagatsuma [5] compared the performances of the Chebyshev, Klann, and Jansen mechanisms regarding energy consumption and trajectory. It was found that the simplest of the three (Chebyshev) yielded the roughest trajectory, while the most complex one (Jansen) resulted in a finer trajectory and had higher efficiency. The authors concluded that walking mechanisms behave similarly to biological evolution based on such results. Moreover, Kim et al. [8] compared the performances of three walking mechanisms (i.e., four-bar, Klann, and Watt-I) using water running as a case. Following the kinematic analysis, the former two yielded higher propulsion.

Additionally, the same mechanism might have multiple purposes, given that it is reconfigurable, i.e., that linkage lengths can be varied during the operation. Sheba et al. [9] presented the reconfigurable Klann mechanism to generate various gait cycles: digitigrade locomotion, jam avoidance, step climbing, hammering, and digging. Foot trajectories were obtained analytically, and link dimensions and the total number of links were varied. Similarly, Nansai et al. [6] and [10] studied and designed a reconfigurable Jansen linkage to produce several gait types: digitigrade locomotion, obstacle avoidance, jam avoidance, step climbing, and drilling motion. Hence, it can be concluded that many mechanism types are used, while the linkage lengths are often varied, especially in reconfigurable mechanisms.

For this reason, the need to adapt the existing walking mechanisms to specialized engineering problems is evident. This problem can be easily solved via optimization, which will, in addition to ensuring a feasible solution, yield additional benefits for regular and reconfigurable mechanisms. Several studies were carried out on the optimization of walking

*Corr. Author's Address: University of Zagreb, Faculty of Mechanical Engineering and Naval Architecture, Ivana Lučića 5, 10002 Zagreb, Croatia, daniel.miler@fsb.hr

mechanisms, especially when developing novel types. For example, Desai et al. [11] presented an eight-link walking mechanism of the planar Peaucellier-Lipkin type. Once the mechanism geometry was outlined, the authors used the genetic algorithm to find the optimal linkage lengths. Variation in the foot path was used as the sole objective function and was minimized, while the transmission angle and stride height were limited. The results were verified experimentally.

Similarly, Erkaya [12] used the genetic algorithm to find the Jansen mechanism linkage lengths that will result in the minimum foot trajectory variations. While developing a legged closed-chain passive-locomotion platform, Wei et al. [13] optimized the foot trajectory. Two objectives were introduced, vertical variation and the longitudinal force between foot and ground. The multi-objective optimization was carried out via a weighted objective function.

A new mechanism optimization process simplifies the mechanism design and improves its outcomes. The non-dominated sorting genetic algorithm (NSGA-II) was used for optimization, while objective functions were evaluated through Simscape Multibody (Matlab subroutine). The mechanism's multi-objective optimization was carried out for three objective function pairs. Furthermore, boundary conditions were included based on Grashof's law to ensure feasibility. The utility of the optimization process was exhibited using the Chebyshev's lambda mechanism as an example. Its performance concerning the trajectory length (in *x*-direction), height variation, foot speed flux, and foot acceleration was assessed.

The primary scientific contribution of this paper is the optimization process; the numerical Simulink calculations were used to determine objective function values, which were then input to NSGA-II for optimization. In each following generation, NSGA-II provides a new set of units for the Simulink evaluation. The paper is outlined as follows: the problem and the associated optimization process were outlined in Section 2, along with design variables, objective functions, and boundary conditions. Algorithm settings were also provided. Further, the Simscape model of the mechanism was shown in Section 3. Next, the optimization process results were presented and discussed in Section 4, while Section 5 provided key findings and limitations of the presented work and a future outlook.

1 METHODS

The Chebyshev lambda mechanism is a simple four-bar linkage mechanism that converts the rotational motion into straight motion. Due to its low trajectory height variability, it is a suitable solution for walking mechanisms. In this paper, it was studied through optimization via the genetic algorithm and Simulink Multibody. Due to its symmetry, one-half of the mechanism was observed in this paper (see Fig. 1).

The multi-objective optimization of the mechanism was carried out using the genetic algorithm; the NSGA-II was used to find the optimal results (for more details, see Section 2.1). Four objective functions were used: length in the x-direction, trajectory height variation, speed fluctuation, and maximum acceleration. The latter two were observed for the output point of the mechanism (i.e., its foot). However, due to the complexity of analytical expressions and to obtain more comprehensive results, Simscape Multibody was used to obtain the values of objective functions numerically. Hence, objective functions and the associated Simscape calculation procedures were outlined in Section 2.2. The optimization process overview is shown in Fig. 2.

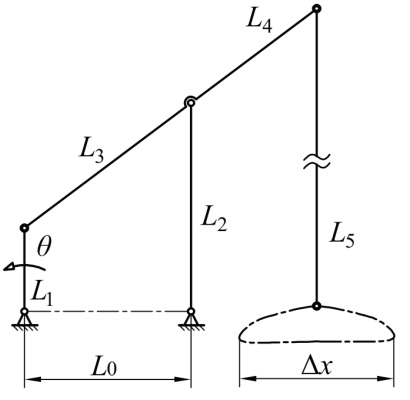

Fig. 1. *Chebyshev's Lambda mechanism – annotations*

The mechanism studied in this paper consists of five linkages, with linkages denoted L_1 to L_5 with default values of {100, 250, 250, 250, 1000} mm. The distance between the anchors was L_0 (see Fig. 1), with a default value of 200 mm. Linkages L_1 and L_2 were anchored, and L_1 served as the mechanism actuator. It should be added that both anchors are located at the same height. The sum of default linkage lengths L_{SUM} = 2050 mm was used as an input parameter, while the lengths were varied (including L_0). Finally, the design variable vector was written as:

$$\mathbf{x} = \{L_0\ L_1\ L_2\ L_3\ L_4\}, \tag{1}$$

while L_5 was calculated by subtracting the design variable vector sum from the L_{SUM}. The values of

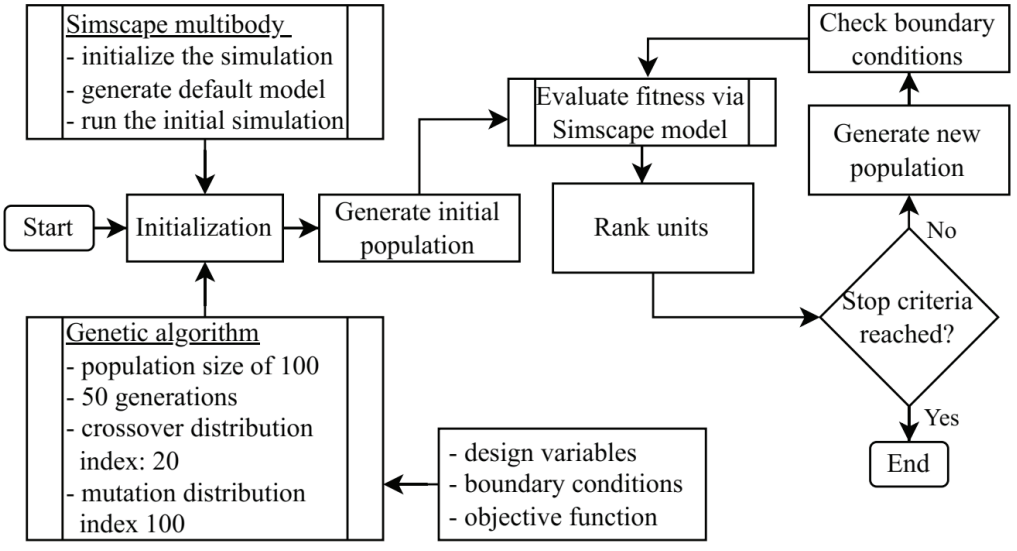

Fig. 2. *Optimization process overview*

design variables L_0, L_1, L_2, and L_4 were varied with respect to the default values used for this type of mechanism. Ranges were set to [0.9…1.1] of default values. This approach was not applied to L_3, as it was necessary to ensure that selected lengths would result in a mechanism that can be assembled for each unit within the population (i.e., mechanism feasibility). Thus, Grashof's criterion was used to find the L_3 boundary:

$$L_3 > L_0 + L_1 - L_2. \tag{2}$$

2.1 Optimization Algorithm Properties

Optimal solutions were found using the NSGA-II [14]. The NSGA-II is a non-dominated sorting genetic algorithm extensively used in engineering due to its ensured convergence and absence of sharing parameters [15]. As such, it was widely applied in multiple engineering fields, with examples including materials design [16], design of mechanical components [17], and energy consumption management [18].

The crossover and mutation rates were defined through the crossover distribution index and the mutation distribution index. Default values provided by the algorithm authors were used; 20 for the crossover and 100 for the mutation distribution index. It was also necessary to select the population size and the number of generations. The selected population size of 100 units was improved through 50 generations to retain reasonable computational time. Moreover, to ensure that the results are near the global optimal, the optimization procedure was verified by repeating the process using the significantly larger population size and the number of generations. The first verification was carried out by increasing the number of generations to 500 while keeping the population size constant. The second verification was the opposite; a large population size (1000 units) was used while the number of generations was kept constant. Finally, algorithm properties were the same for each of the observed objective function sets.

2.2 Calculating the Objective Function Values

As noted earlier, this study considered four objective functions: the length in the x-direction, trajectory height variation, foot speed fluctuation, and maximum foot acceleration. As shown in Fig. 1, the genetic algorithm exported the linkage lengths for each of the units in the population, which were then automatically imported into Simscape.

The Simscape mechanism model was developed as follows: the Chebyshev lambda mechanism consisting of linkages, joints, and anchors was modelled. Linkage properties were defined, including their cross-section and material properties; additionally, linkages were connected using pins, which were also fully defined. The relations between the linkages were achieved using joints, for which it was necessary to define degrees of freedom. Measurements were carried out at point 5 (mechanism foot), located on the free end of the linkage L_5 (Fig. 2). Its position, velocity, and acceleration were output for

each position during the cycle. The top-level schema of the Simscape model is shown in Fig. 3.

Simscape Multibody simulation was carried out next and provided all the necessary information; foot positions, velocities, and accelerations were calculated for the mechanism cycle. The resulting points were then used to obtain the values of objective functions. The stride cycle was discretized into 3024 points, and the leg foot positions and accelerations were calculated for each point. Hence, the calculation step was 0.12°.

2.2.1 Length in the x-Direction

Length in the x-direction (also denoted as Length Δx) was selected as the base objective and was thus considered in each of the optimization processes. It should be noted that it is possible to increase the device speed by maximizing the x-direction length (given the constant input rotational speed). It was calculated based on the leg foot trajectories obtained through Simscape simulation. Once the trajectories were exported, their minimum and maximum values in the x-axis were found and subtracted. Hence, the first objective function f1(x) was obtained as:

$$f_1(\mathbf{x}) = \Delta x = x_{\max} - x_{\min}. \tag{3}$$

2.2.2 Trajectory Height Variation

Trajectory height variation was used as the second objective function and was minimized. Firstly, it

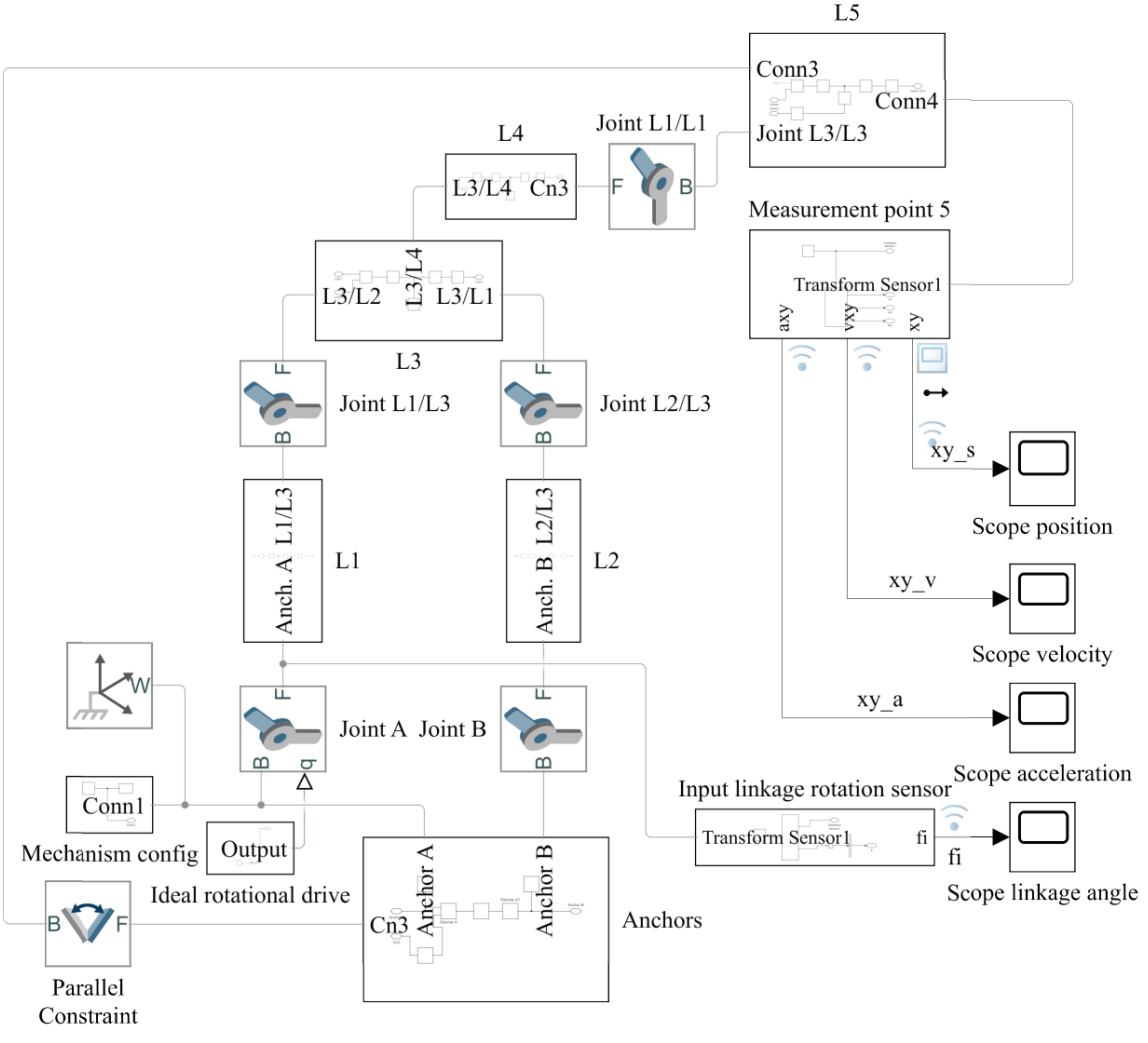

Fig. 3. *Simscape simulation schematic*

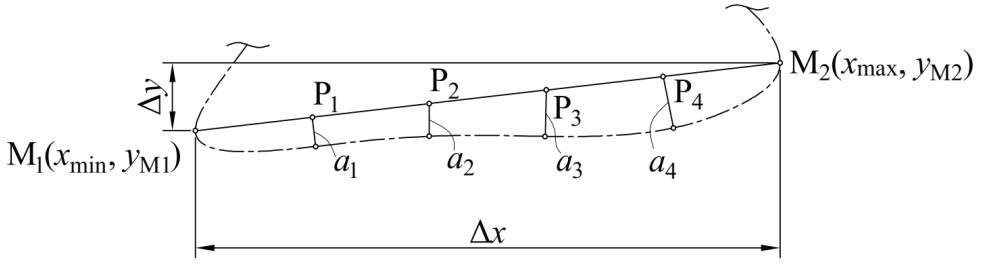

Fig. 4. *The trajectory height variation minimization*

was necessary to determine the points outlining the maximum length in the *x*-direction – $M_1(x_{min}, y_{M1})$ and $M_2(x_{max}, y_{M2})$. The trajectory height variation denoted as H_{var} was minimized between M_1 and M_2 to reduce the changes in the vertical direction (Fig. 4). It was necessary to reduce the change in height between points M_1 and M_2 (i.e., to reduce $|y_{M1} - y_{M2}|$), as well as to reduce the changes in the *x*-direction length.

Thus, the objective function was created; the difference between y_{M1} and y_{M2} was squared and multiplied by the sum of the distances between points P_1, P_2, P_3, and P_4, and the foot trajectory. The difference was squared to emphasize the role of the difference between heights of points M_1 and M_2 while also ensuring that it will always be positive. Hence, in combination with the distances between the points and the foot trajectory, which are always positive, trajectory height variation will always be positive. Finally, trajectory height variation was expressed as the objective function $f_2(\mathbf{x})$ and minimized:

$$f_2(\mathbf{x}) = H_{var} = (y_{M1} - y_{M2})^2 \cdot \cdot \left[\min(a_1) + \min(a_2) + \min(a_3) + \min(a_4)\right], \quad (4)$$

where *n* denotes the number of discrete points within the interval.

The height variation function presented above has no physical meaning; it is merely a function providing the lowest variations in trajectory height. While the difference between the overall maximum and minimum *y*-axis position is simpler to calculate and can also be used, it would not guarantee steady movement. In this case, the resulting curves had low quality and did not result in an industrially viable mechanism.

2.2.3 Speed Fluctuation

The speed fluctuation was selected as the third objective function. Minimizing the foot speed fluctuation will result in reduced accelerations throughout the cycle. This will, in turn, reduce inertial forces during the cycle, resulting in a smoother operation **[19]**. In this study, the foot speed fluctuation was taken as:

$$f_3(\mathbf{x}) = \frac{\sum_{i=1}^{n} \left| v_i - v_{avg} \right|}{n}, \quad (5)$$

where *n* is the number of discrete points observed during one cycle (in this article, $n = 3024$), v_i is the resultant speed in each of the points, and v_{avg} is the average speed of all the points.

2.2.4 Maximum Foot Acceleration

While reducing the speed fluctuation will result in a more uniform acceleration during the stride, it will not directly affect its maximum value. However, reducing the maximum foot acceleration will result in a lower maximum inertial force, often used as an input while sizing the drive mechanism. Hence, foot acceleration was used as the fourth objective function. The maximum acceleration was obtained from the Simscape data as a result of *x*-axis and *y*-axis accelerations and was minimized:

$$f_4(\mathbf{x}) = a_{max}. \quad (6)$$

3 RESULTS AND DISCUSSION

The optimization processes were carried out for three sets of objective functions according to the method outlined in Section 2. Objective function sets were as follows: length in the *x*-direction and trajectory height variation (set 1), length in the *x*-direction and speed fluctuation (set 2), and length in the *x*-direction and acceleration (set 3). Furthermore, it should be noted that optimization was carried out using a personal computer with an i7-4810MQ processor (2.86 GHz)

and 32 GB of RAM. The time needed to evaluate units from each set was similar, regardless of the objective function, meaning that the Simscape simulation had a significantly higher computational cost compared to NSGA-II operations. The average calculation time was approx. 2 s per unit. Additionally, validation was carried out using set 1 as an example (for more details on the validation, see Section 2.1).

3.1 Length Δx and Trajectory Height Variation

The optimization process was first carried out using the length in the *x*-direction and trajectory height variation as objective functions. Four Pareto optimal solutions were obtained, as shown in Fig. 5. The solutions were labelled as "Height" and index ranging between 1 and 4, with lower indices representing larger strides (and higher variations in trajectory height). Hence, the highest *x*-direction length was obtained for Height 1, 584.2 mm, with a height variation value of 955.6. The lowest trajectory variation was obtained for the solution labelled Height 4, 0.01833, with the corresponding Δx = 483.6 mm.

Compared to other optimization processes (see Sections 3.2. and 3.3.), only four solutions were found on the Pareto front; all remaining final population solutions were dominated by the four solutions presented in Fig. 5. and Table 1.

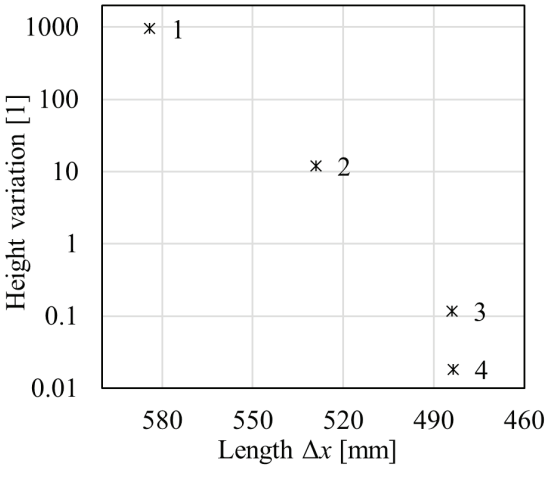

Fig. 5. *The x-direction length and height variation*

The range between the extreme Pareto solutions for Δx was 100.6 mm (17.22 % of the highest obtained value). Solution height variations could not be compared in a similar manner as the change was not linear (see fitness function f_2). Thus, to better illustrate changes in the height variation and the importance of measurement, strides were plotted for all the Pareto optimal solutions (Fig. 6).

Table 1. *Set 1 solutions – values*

No.	L_0	L_1	L_2	L_3	L_4	L_5
1	180.8	108.4	237.7	234.3	272.2	1197
2	189.3	98.67	269.4	270.2	261.5	1150
3	187.9	98.97	235	232.2	252.2	1232
4	186	101.5	231.8	231	237.1	1248

Linkage lengths measured in mm

As shown in Fig. 6, paths obtained for solutions Height 1 and Height 2, with respective height variation values of 955.6 and 12.03, resulted in a curved bottom segment of the leg trajectory. Since the bottom segment corresponds with the period during which the foot is in contact with the surface, both solutions will require larger torque to operate. Changes in height will require the driver to lift the device body and provide movement in the horizontal direction. In contrast, the bottom trajectory segments of solutions Height 3 and Height 4, with height variations of 0.118 and 0.018, respectively, were remarkably straight. While the variations were slightly more prominent in the Height 3 trajectory, as shown in Fig. 6, it can be concluded that both solutions will not require an increase in required input torque. Moreover, it can be concluded that the height variation of 0.12 is acceptable, but the value is strictly limited to the optimization of similarly sized mechanisms.

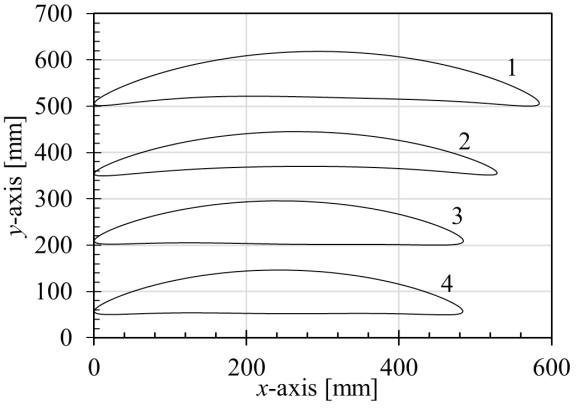

Fig. 6. *Foot paths of Pareto optimal solutions*

Finally, none of the variables constituting Pareto optimal solutions were in the vicinity of the design variable range boundaries. Similarly, the same design variables were also not restricted by Grashoff's criterion. Therefore, it was concluded that the selected design variable ranges were appropriate for optimizing

the Chebyshev Lambda mechanism considering the Δx length and height variation.

3.2 Change in the x-direction and Speed Fluctuation

The optimization process was carried out for the Δx length and speed fluctuation along the stride. Solutions on the Pareto front and the associated linkage lengths are provided in Fig. 7 and Table 2. Similarly to Section 3.1, Pareto optimal solutions were indexed from 1 to 11, starting with the solution having the longest Δx length. Additionally, the label "Speed" was included before the index. The highest obtained Δx was 487.3 mm; the same solution yielded a speed fluctuation of 7426 (Speed 1). On the other side of the Pareto front, the lowest speed fluctuation of 6861 was obtained, for which Δx = 464.7 mm (Speed 11).

3.3 Change in the x-direction and Acceleration

The x-direction length and maximum foot acceleration were selected as the third pair of objective functions. This combination was to provide a mechanism that will result in a steady and fast movement, and the results are presented in Fig. 8 and Table 3. Eleven Pareto optimal solutions were found, labelled as "Acceleration" 1 to 11, with lower indices associated with larger Δx values and higher accelerations; the opposite was true for higher indices. The largest Δx length of 445.1 mm was obtained for the solution Acceleration 1, corresponding to the highest acceleration between the solutions (122.7 m/s^2). In contrast, the lowest acceleration of 117.3 m/s^2 was obtained for Acceleration 11 (Δx = 432.7 mm). The ranges between the extreme Pareto solutions were

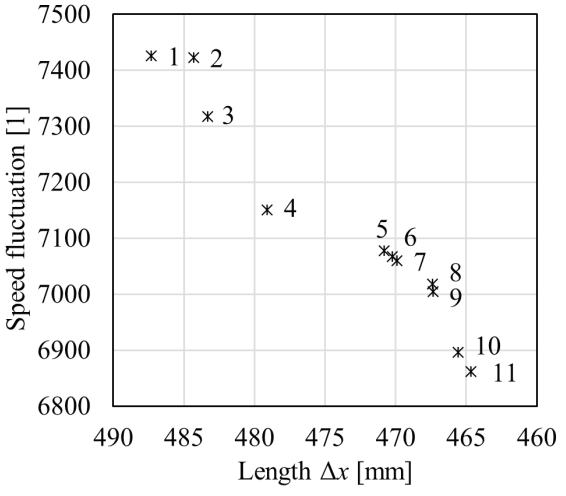

Fig. 7. *The x-direction length and speed fluctuation*

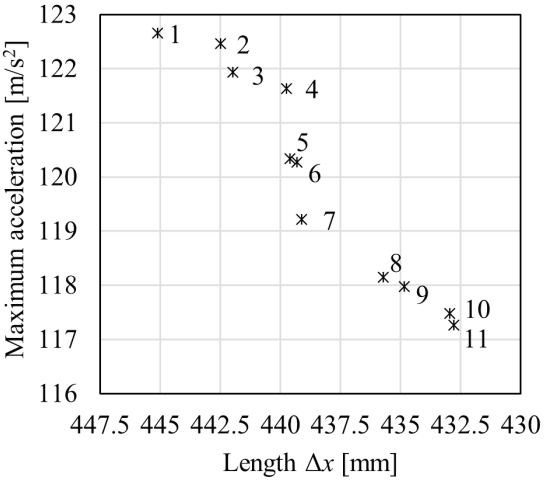

Fig. 8. *Length Δx and maximum acceleration*

Table 2. *Set 2 solutions – values*

No.	L_0	L_1	L_2	L_3	L_4	L_5
1	206.4	97.18	270.2	172.5	241.5	1268
2	206.6	97.37	272.0	177.0	240.8	1263
3	206.6	97.13	269.5	172.6	240.3	1271
4	207.3	96.44	268.6	169.6	240.0	1275
5	191.0	90.17	252.6	160.8	234.9	1312
6	191.2	90.38	252.5	162.2	235.4	1310
7	189.6	90.16	252.5	165.0	235.0	1307
8	191.7	90.12	251.0	159.9	235.1	1314
9	191.4	90.09	251.0	160.3	235.1	1314
10	218.6	97.95	270.2	161.3	237.8	1283
11	217.2	97.51	271.2	164.8	238.1	1278

Linkage lengths measured in mm

Table 3. *Set 3 solutions – values*

No.	L_0	L_1	L_2	L_3	L_4	L_5
1	216	90.63	250.5	157.2	265.5	1286
2	215.8	90.64	251.1	158.1	263.1	1287
3	216.5	90.67	249.8	156.1	263.4	1290
4	216.3	91.12	249.3	159.2	263.6	1287
5	215.8	90.80	251.5	160.2	261.9	1286
6	215.8	90.83	251.4	160.7	261.9	1285
7	216.4	90.58	249.1	156.8	263.3	1290
8	216	90.15	251.0	159.5	261.6	1288
9	216.5	90.20	248	156.4	262.6	1298
10	216.6	90.02	247.8	156.1	262.1	1294
11	217.3	90.13	248.8	156.8	262.1	1292

Linkage lengths measured in mm

12.34 mm for the Δx length (2.77 % of the highest obtained value) and 4.4 m/s^2 for the acceleration (4.4 %). Thus, it can be concluded that changes in acceleration were more prominent when observing the Pareto front.

Regarding the variable boundary ranges, the only active condition was for the lower L_1 value, which was set to 90 mm. All the Pareto-optimal solutions stemmed toward the lower variable boundary, implying that when aiming to increase the Δx length and decrease the foot acceleration, the L_1 range should be increased further. The distance between the anchors L_0 in optimal solutions ranged between 215.8 mm and 217.3 mm, illustrating a rather low variance. Linkage L_2 length was practically equal to the default value, while the lengths of linkages L_3 differed the most with respect to the defaults.

Obtained accelerations are theoretical and much higher than their experimental counterparts. This is due to the fixed rotational velocity at the mechanism input. The constant rotational velocity implies infinite torque; in other words, realistic loads stemming from the mechanism operation will not slow down the motor. Hence, high acceleration values were obtained, resulting in significant inertial forces within the system. In a realistic case, if operated via motor, such large accelerations would not occur as the increased inertial forces would slow down the motor.

3.4 Comparison to the Default Mechanism

Furthermore, to compare previously obtained Pareto fronts to the default mechanism, its characteristics were determined next. The default mechanism x-direction length was 470.4 mm. A trajectory height variation of 0.2799 was also obtained, while the speed fluctuation was 4.32e4. Finally, the maximum acceleration of the default mechanism foot was 2.27e5 m/s^2.

The default value was compared to designated solutions from the Pareto optimal fronts for each pair of objective functions, as shown in Fig. 9. The objective function outputs for each of the solutions in the diagram were divided with the corresponding value obtained for the default solution. The only exception was the trajectory height variation, normalized to a [0, 1] interval via min-max normalization supplemented with a logarithmic operator. This was necessary to retain clarity, as the objective function outputs for trajectory height variation were exponential. They were normalized as follows:

$$H'_{\mathrm{var}\,i} = \frac{\log H_{\mathrm{var}\,i} - \min\left(\log H_{\mathrm{var}}\right)}{\max\left(\log H_{\mathrm{var}}\right) - \min\left(\log H_{\mathrm{var}}\right)}. \quad (7)$$

As shown in the figure, solutions obtained while optimizing for length Δx and trajectory height variation (Height 1 and 4) yielded larger values than the default solution. While Height 1 Δx was significantly larger compared to the default solution, so was its height variation. In contrast, Height 4 Δx was 13.2 mm longer, having lower height variation, speed fluctuation, and slightly higher maximum acceleration. Compared to other solutions (barring Height 4), the default one had a significantly lower trajectory height variation. Thus, it is recommended to include the height variation as a boundary condition when designing a walking mechanism.

Moreover, when considering the speed fluctuation criterion, the default solution resulted in the second-highest value (behind the Height 1 solution). Solutions

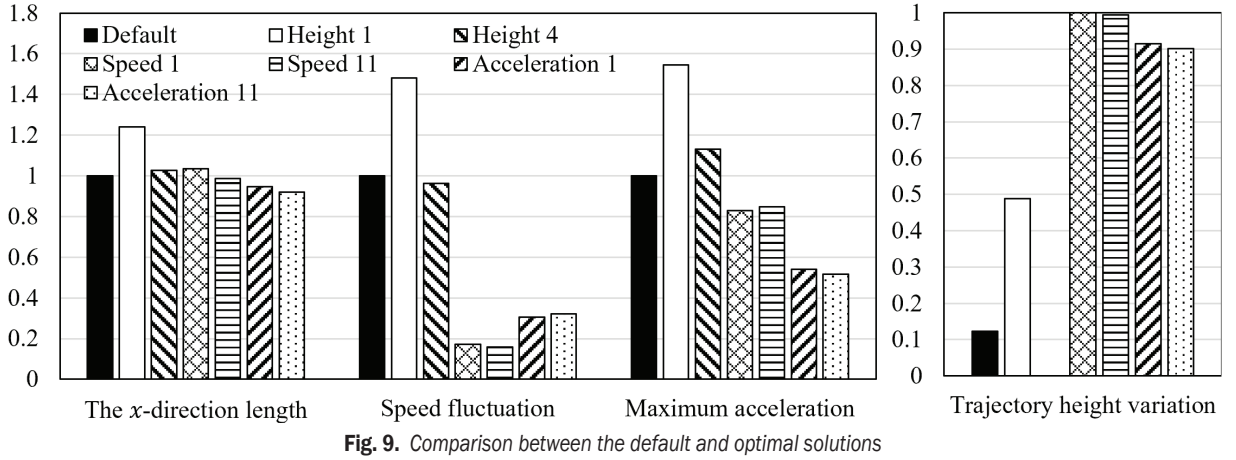

Fig. 9. *Comparison between the default and optimal solutions*

obtained when minimizing the acceleration had a low-speed fluctuation, as expected. Similarly, solutions obtained when aiming to reduce the speed fluctuation (Speed 1 and Speed 11, for more details, see Section 3.2.) resulted in low maximum acceleration values. Such behaviour was expected, as speed fluctuation and maximum acceleration are linked indirectly.

Finally, it should be clarified that in Fig. 9, a higher Δx length is considered positive, while higher speed fluctuation, maximum acceleration, and trajectory height variation values imply a lower-quality solution. Moreover, in the trajectory height variation graph, the solution Height 4 column is missing; it had the lowest value of all the seven observed solutions and was normalized to 0.

4 CONCLUSIONS

The procedure for multi-objective optimization of walking mechanisms based on the Simscape Simulation embedded within the NSGA-II was presented. The simplest of the mechanisms, the Chebyshev Lambda mechanism, was used as an example and was optimized. The proposed method also applies to both 6-bar and 8-bar linkages, with slight differences in integration. A new computer-aided design (CAD) model should be created, and corresponding design variables and boundary conditions should be selected.

The variable ranges were set based on the default mechanism, and Grashoff's criterion was used to ensure that the resultant solutions would be viable. Optimal solutions were found for three pairs of objective functions: Δx length/height variation, Δx length/speed fluctuation, and Δx length/maximum foot acceleration. Based on the presented results, the following conclusions were made:

- The presented procedure enabled a timely and comprehensive analysis of the candidate mechanisms; the calculation time was approximately 2 s per unit.
- Considering the length in the x-direction and height variation, notable advancements were made. For the Pareto optimal solution with the highest length, the increase with respect to the default solution was 24.2 %. Moreover, all the Pareto optimal solutions had higher Δx lengths than the default solution.
- It is recommended to introduce the trajectory height variation as a boundary condition when aiming to use the Chebyshev Lambda mechanism as a walking mechanism.

However, the limitations of the presented study should be addressed as well. The proposed method considers the walking mechanism without taking into account its surroundings. A device utilizing walking mechanisms for movement will include multiple such mechanisms; hence, influences of operating conditions and gaits (e.g., biped, quadruped, hexapod) should also be considered. Furthermore, when using the results of this study, it is necessary to acknowledge that a minimal number of boundary conditions was used as the authors primarily observed the effects of objective functions on the solution characteristics. Hence, some of the Pareto solutions would result in sub-optimal walking mechanisms due to variations in length in the x-direction.

For this reason, in the future study, we plan to generate a mechanism through multi-objective optimization by simultaneously introducing all the objective functions (instead of pairs, which were considered here). Finally, it should be added that this study only considered the mechanism kinematics; hence, the viability of the optimal mechanism should be verified by either simulating its dynamics or experimentally.

5 REFERENCES

[1] Wu, J., Yao, Y. (2018). Design and analysis of a novel walking vehicle based on leg mechanism with variable topologies. *Mechanism and Machine Theory*, vol. 128, p. 663-681, **DOI:10.1016/j.mechmachtheory.2018.07.008**.

[2] Kulandaidaasan Sheba, J., Elara, M., Martínez-García, E., Tan-Phuc, L. (2016). Trajectory generation and stability analysis for reconfigurable Klann mechanism based walking robot. *Robotics*, vol. 5, no. 3, art. ID. 13, **DOI:10.3390/robotics5030013**.

[3] Singh, R., Bera, T.K. (2020). Walking model of Jansen mechanism-based quadruped robot and application to obstacle avoidance. *Arabian Journal for Science and Engineering*, vol. 45, p. 653-664, **DOI:10.1007/s13369-019-04135-8**.

[4] Kim, H., Jeong, K., Seo, T. (2017). Analysis and experiment on the steering control of a water-running robot using hydrodynamic forces. *Journal of Bionic Engineering*, vol. 14, p. 34-46, **DOI:10.1016/S1672-6529(16)60376-1**.

[5] Komoda, K., Wagatsuma, H. (2017). Energy-efficacy comparisons and multibody dynamics analyses of legged robots with different closed-loop mechanisms. *Multibody System Dynamics*, vol. 40, p. 123-153, **DOI:10.1007/s11044-016-9532-9**.

[6] Nansai, S., Elara, M.R., Iwase, M. (2013). Dynamic analysis and modeling of Jansen mechanism. *Procedia Engineering*, vol. 64, p. 1562-1571, **DOI:10.1016/j.proeng.2013.09.238**.

[7] Sheba, J.K., Martinez-Garcia, E., Elara, M.R., Tan-Phuc, L. (2015). Design and evaluation of reconfigurable Klann mechanism based four legged walking robot. *10th International*

Conference on Information, Communications and Signal Processing, p. 1-5, **DOI:10.1109/ICICS.2015.7459939**.

[8] Kim, H., Lee, S., Lim, E., Jeong, K., Seo, T. (2016). Comparative study of leg mechanisms for fast and stable water-running. *International Journal of Precision Engineering and Manufacturing*, vol. 17, p. 379-385, **DOI:10.1007/s12541-016-0047-3**.

[9] Sheba, J.K., Rajesh, M., Mart, E., Tan-phuc, L. (2017). Synthesizing reconfigurable foot traces using a Klann mechanism. *Robotica*, vol. 35, no. 1, p. 189-205, **DOI:10.1017/S0263574715000089**.

[10] Nansai, S., Rojas, N., Elara, M.R., Sosa, R., Iwase, M. (2015). On a Jansen leg with multiple gait patterns for recon-figurable walking platforms. *Advances in Mechanical Engineering*, vol. 7, no. 3, **DOI:10.1177/1687814015573824**.

[11] Desai, S.G., Annigeri, A.R., TimmanaGouda, A. (2019). Analysis of a new single degree-of-freedom eight link leg mechanism for walking machine. *Mechanism and Machine Theory*, vol. 140, p. 747-764, **DOI:10.1016/j.mechmachtheory.2019.06.002**.

[12] Erkaya, S. (2013). Trajectory optimization of a walking mechanism having revolute joints with clearance using ANFIS approach. *Nonlinear Dynamics*, vol. 71, p. 75-91, **DOI:10.1007/s11071-012-0642-5**.

[13] Wei, C., Sun, H., Liu, R., Yao, Y., Wu, J., Liu, Y., Lu, Y. (2022). Analysis and experiment of thrust-propelled closed-chain legged platform with passive locomotion ability. *Mechanism and Machine Theory*, vol. 167, art. ID 104506, **DOI:10.1016/j.mechmachtheory.2021.104506**.

[14] Deb, K., Pratap, A., Agarwal, S., Meyarivan, T. (2002). A fast and elitist multi-objective genetic algorithm: NSGA-II. *IEEE Transactions on Evolutionary Computation*, vol. 6, no. 2, p. 182-197, **DOI:10.1109/4235.996017**.

[15] Miler, D., Hoić, M., Škec, S., Žeželj, D. (2020). Optimisation of polymer spur gear pairs with experimental validation. *Structural and Multidisciplinary Optimization*, vol. 62, p. 3271-3285, **DOI:10.1007/s00158-020-02686-1**.

[16] Zhang, P., Qian, Y., Qian, Q. (2021). Multi-objective optimization for materials design with improved NSGA-II. *Materials Today Communications*, vol. 28, art. ID 102709, **DOI:10.1016/j.mtcomm.2021.102709**.

[17] Miler, D., Hoić, M. (2021). Optimisation of cylindrical gear pairs: A review. *Mechanism and Machine Theory*, vol. 156, art. ID 104156, **DOI:10.1016/j.mechmachtheory.2020.104156**.

[18] Ghaderian, M., Veysi, F. (2021). Multi-objective optimization of energy efficiency and thermal comfort in an existing office building using NSGA-II with fitness approximation: A case study. *Journal of Building Engineering*, vol. 41, art. ID 102440, **DOI:10.1016/j.jobe.2021.102440**.

[19] Ingram, A.J. (2006). *A New Type of Mechanical Walking Machine* (PhD thesis). University of Johannesburg, Johannesburg.

Strojniški vestnik - Journal of Mechanical Engineering 68(2022)12, 735-745
DOI:10.5545/sv-jme.2022.306
Original Scientific Paper
Received for review: 2022-08-01
Received revised form: 2022-11-10
Accepted for publication: 2022-11-28

Investigation of Laser Ablative Micromachining of Al/TiB_2 Nanocomposite

Pratheesh Kumar Manikandan Rajam* – Jayakrishnan Nampoothiri
PSG College of Technology, Department of Production Engineering, India

Laser beam machining (LBM) is used to machine a variety of materials economically and to obtain the required quality metrics. The quality of the surface finish of laser-machined components is affected by the improper selection of process parameters during machining. In this paper, microchannels were machined on Al/TiB_2 nanocomposite using an Nd: YAG laser system. An atomic force microscope was used to obtain the surface roughness of microchannels. The aim of this process is to identify the influence of the individual and interactive effect of the process parameters on the surface roughness of the microchannels and to identify the optimum combination of the process parameters for minimum surface roughness. Taguchi's L9 orthogonal array-based Design of Experiment (DoE) was implemented to conduct the experimental study. A statistical analysis of the results was performed for the experimental data. The results are presented in detail.
Keywords: Laser micromachining, surface roughness, nanocomposite, parameter optimization, Taguchi methodology, Nd: YAG Laser

Highlights
- *Al/TiB_2 nanocomposite processing, characterization, and laser micromachining of Al/TiB_2 is explained in detail.*
- *Measurement of surface roughness (Ra) of microchannels using atomic force microscope and the optimum combination of the LBM parameters is determined.*
- *Analysis of the influence of the interaction effect of the laser-machining process parameters on Ra is presented.*

0 INTRODUCTION

Unconventional machining processes have gained a significant amount of research attention owing to their ruggedness and efficiency. Such machining processes are being utilized to machine high-strength materials with complex shapes in an easy manner. The conventional machining processes require cutting tools harder than the workpiece. These processes also result in the poor surface finish of the workpiece at the micro level due to abrasion. Advanced ceramic materials, such as aluminium oxide, zirconia, aluminium titanate, magnesium oxide, and silicon carbide have a variety of applications due to their thermo-physical and mechanical characteristics [1]. The laser can be utilized to cut such high-strength alloys to obtain the required shape and dimension. The concentrated energy of the laser beam is highly intended to melt high-strength materials due to its high-power density [2]. Laser beam machining (LBM) process is preferred over the other unconventional machining processes owing to its high ablation rate and the ability to yield a good surface finish. The laser is used for generating complex 2D and 3D patterns at micromachining domains [3] to [5]. The schematic diagram of a typical laser beam machining system is shown in Fig. 1. The scope to explore the laser micromachining of anisotropic metal matrix composites is very high.

Kibria et al. [6] machined micro-grooves on aluminium oxide ceramic to study the effect of successive spot and circumferential overlap of the laser beam on the roughness of the machined surface. Different spot overlaps have been used along with the other input parameters. The results showed that surface roughness decreases with the increase of both the overlap factors. Yue and Lau [7] investigated the pulsed laser cutting of an Al-Li/SiC metal matrix composite and concluded that it is possible to minimize the heat-affected zone (HAZ) and improve the machined surface quality with proper control of process parameters. It was found that proper control over the machining parameters is required to improve the surface finish and minimize the HAZ.

Qiao et al. [8] used a Nd: DPSS laser system with a repetition frequency of 20 kHz to 120 kHz and a maximum power of 25 W to investigate the effects of water jet guided laser micro-machining on surface topography, greatest aspect ratio evolution, and kerf edge fluctuations. The experimental findings showed no signs of oxidation or cracks on the kerf edge or other surfaces. The kerf aspect ratio ranged up to 12.7, indicating that the kerf is extremely steep. A form of water-conducting laser processing technique was developed by Zhihe et al. [9]. The basis of laser water-jet coupling technology was used to construct a set of water-conducting laser processing system. Studies on water-conducting laser processing were conducted on a variety of metal materials. The work

*Corr. Author's Address: PSG College of Technology, Coimbatore 641004, India, mrpratheesh@gmail.com

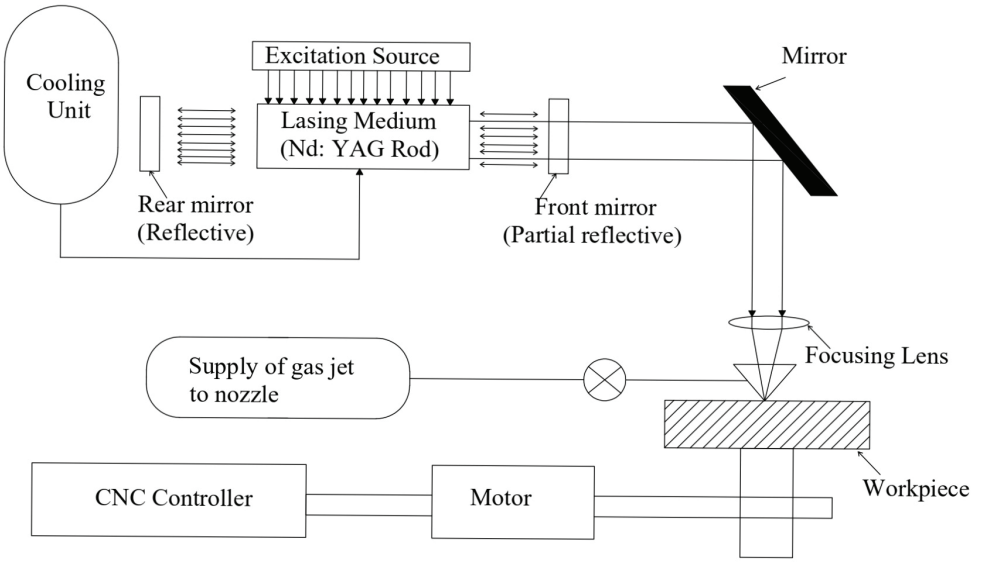

Fig. 1. *Typical laser beam machining system*

surfaces were examined using a digital microscope. The edges of grooves and blind holes were straight, burr-free, and regular in two different types of materials. Neither material had a heat-affected zone. The water-conducting laser processing technique was practicable, according to experiments on precision metal machining. Yongfei et al. [10] examined how different settings of Water Guided Laser Machining (WGLM) affected the micro-morphology of materials and the way that lasers interact with materials. During the tests, thin samples of 316L stainless steel were machined with slots and grooves using the WGLM technology. After experiments, the 2D and 3D micro-topography was examined. The results of the studies showed that the machining time and the number of machining times have no effect on the breadth of deposition layers.

The glass material was coated to increase its absorptivity and the impact of coating and the laser machining parameters, such as laser power, laser scanning speed, and angle of inclination of the workpiece on the depth and width of the slot, aspect ratio, and material removal rate (MRR) using a 2k factorial design and analysis of variance (ANOVA) by Posa et al [11]. The depth of the slot increased four times, the breadth of the slot increased twice, and the MRR increased seven times when coated glass work samples were compared to uncoated glass work samples. Demarbaix et al. [12] investigated the effects of laser settings on roughness, local sintering, and machining depth during laser machining of Yttrium Oxide Tetragonal Zirconia Polycrystalline ceramic material. The spot overlap, which was related to the repetition rate and feed rate, was discovered to be a factor in roughness and local sintering. The average power had very little impact on sintering, in contrast to the spot overlap. The optimal settings were determined to be an average power of 15 W, a feed rate of 1100 mm/s, a repetition rate of 15 kHz, and a slice of 5 m. When paired with other process variables, including average power, duty cycle, pulse repetition rate, and scanning speed, Pramanik et al. [13] examined the impact of sawing angle on the diameter deviation of Monel sheet metal. The input parameter sawing angle had a crucial influence in the top and bottom diameter variation when drilling 0.7 mm thick Monel K-500 alloy sheet using a low fibre laser beam. By adjusting the controllable process parameters to achieve the required diameter deviation, the proposed model was found to be valid. Regression analysis was used to create a model that forecasts how different process parameters would affect the quality of laser cuts. The optimization process in this paper used the teaching-learning algorithm. Muthuramalingam et al. [14] optimised the effects of process factors on surface performance measures when milling titanium alloy using a Taguchi-Grey relational technique. They found that laser power significantly affects the quality measurements of surface roughness and taper angle in LBM due to the relevance of plasma energy. The ideal process parameter set of laser power (3 kW), nozzle distance (1.5 mm), focal length (2 mm), and gas pressure (2 bar) was chosen due to its ability to produce reduced plasma energy with a precision of

2.2 %. Lower surface roughness was produced by the reduced nozzle distance and higher laser power due to the formation of micro-craters and decreased particle adhesion. Regression modelling and particle swarm optimization (PSO) were combined in a hybrid technique by Shrivatsava et al. [15] to optimise the process parameters during the laser cutting of Inconel-718 sheet. The trials made use of four machining parameters: cutting speed, laser power, standoff distance, and assist gas pressure. The kerf width and kerf taper were employed as output quality characteristics. The L27 orthogonal array was used to conduct the studies. When the experimental results were contrasted with the ideal outcomes, it became clear that there had been individual improvements in the output quality attributes of kerf width and kerf taper of roughly 10 % and 57 %, respectively. There was an improvement of 46 % in overall performance during the optimization. Also addressed was the effect of various process parameters on performance measures.

Deng et al. [16] attempted a novel material processing in which laser surface melting modification combined with precision milling was done to improve the surface integrity and machinability. The surface modification using a laser was done between 1397 °C and 2000 °C. This process, along with the controlled parametric setting of the precision milling, resulted in the improvement of surface finish by 90.36 % and tool life by 61.03 %. The influence of the CO_2 laser parameters, such as the cutting speed and laser power on the surface roughness parameter of the low-carbon steel was studied using ANOVA by Boujelbene [17]. Boujelbene et al. [18] investigated the effect of laser cutting conditions, such as cutting speed, laser power, and gas pressure on the surface roughness of titanium specimens using the Taguchi method. It was found that surface roughness decreases with faster cutting speeds and increases with the evolution of thermal energy by laser power. The optimum cutting conditions for the minimum value of Ra and Rt were found.

The experimental study conducted by Cekic et al. [19] showed that the surface roughness (*Ra*) value decreases with the use of N_2 as an assist gas and at a higher cutting speed. Kim et al. [20] explored the possibilities to machine AlSiC composites using a hybrid-hybrid system of a combination of ultrasonic and laser-assisted turning processes. The cutting force developed, and the surface roughness of the machined components was comparatively less than that of the conventional machining forces. The surface topography of the machined surface is an interesting parameter in tribology and fluid mechanics for the effective movement and separation of the fluid in the microfluidic chips of the micromechanical systems [20]. As the presence of ceramic particles in the metal matrix composites (MMCs) accelerates tool wear, thus increasing the cutting force developed and surface roughness of the finished components, laser machining and hybrid laser machining are the solutions for this problem [22].

This research on finding the individual and interactive effect of the process parameters on surface roughness of microchannel machined using LBM will be useful in understanding the laser machining of Al/TiB_2 composites, which are used in different applications. Experiments were carried out using a Taguchi L9 orthogonal array, and ANOVA was used to investigate the impact of process factors on surface roughness. The surface roughness of microchannels was measured using an atomic force microscope.

1 MATERIALS AND METHODS

In this study, Al A356 alloy and TiB_2 ceramic particles were selected as the matrix and reinforcement materials for the in-situ synthesis of composite samples. The preparation of the nanocomposite material was done by melting 500 g of aluminium A356 alloy in a carbon crucible at 725 °C with the help of an electric furnace, and a pre-weighed mixture of K_2TiF_6 and KBF_4 salts were added to the melt. Then the melt was raised to a temperature of 800 °C and allowed to undergo aluminothermic reactions for a duration of one hour with intermittent stirring at a regular interval of 10 min. The slag floated on the top surface of the melt was removed, and the composite melt was transferred to a preheated clay graphite crucible for treatment with ultrasonic vibrations of 20.1 kHz frequency. A Ti-6Al-4V sonotrode of 40 mm diameter was employed for the effective transfer of ultrasonic vibrations. The composite melt was cast into a pre-heated mould of a diameter of 18 mm and length of 110 mm. A detailed description of nanocomposite fabrication is discussed in [23] to [25]. The X-Ray diffractograph obtained from the composite samples was indexed with the help of Joint Committee on Powder Diffraction Standards (JCPDS) software; the indexed pattern is presented in Fig. 2a. The indexed pattern presented in Fig. 2a. closely matches the standard pattern of aluminium (JCPDS-No: 040787), Si (JCPDS-No: 271402) and TiB_2 particles (JCPDS-No: 350741). The indexing of the diffractograph confirmed the formation of TiB_2 particles and the absence of any other intermetallic phases and/or slag infusion.

To ensure the formation of TiB_2 particles, a sample of the thickness of 10 mm was cut and analysed using Cu-Kα radiation in a Shimadzu XD-D1 XRD analyser. Further, to analyse the particle size, a small disc of ~500 µm thick nanocomposite sample was sliced and further thinned with help of disc grinding, dimple grinding, and Argon ion milling. The ion-milled nanocomposite disc was analysed using a JEOL JEM 2100 Transmission Electron Microscope (TEM) operated at 200 kV. The TEM micrograph of the ultrasonic treated A356/2TiB_2 composite sample is shown in Fig. 2b, and it confirms that the particles are in the nano-regime (<100 nm) and the average particle size is 29 nm ± 12 nm. The TEM micrograph further confirms that the hexagonal disc-shaped TiB_2 nanoparticles are dispersed uniformly in the α-Al matrix.

The Al/TiB_2 nanocomposite exhibits an average ultimate tensile strength of 290 MPa in as-cast and 330 MPa in T6 conditions. The hardness of the nanocomposite is in the range of 160 VHN to 180 VHN [26] and [27]. The presence of TiB_2 particles in the aluminium matrix impedes the propagation of dislocation through the matrix phases. The resistance to dislocation propagation increases the strength of the composite material and the presence of the reinforcement reduces its plasticity. This property modification in turn increases the cutting force requirement, cutting temperature, and tool wear during conventional machining.

Literature reveals that the presence of nano-sized TiB_2 particles induces abrasive wear on cutting tools due to the scratching effect of hard nano-sized particles [28]. In general, the conventional machining of composite material with TiB_2 particles may result in machining issues such as smearing, micro-scratches, and pits on the machined surfaces. In the case of a spark-machining method like EDM, the presence of nano-sized particles reduces the electrical conductivity of the composite and also adversely affects the debris removal and spark gap. Not only the mechanical property-related challenges but also the physical property challenges and process difficulties makes Al/TiB_2 hard to machine. LBM is more preferable for

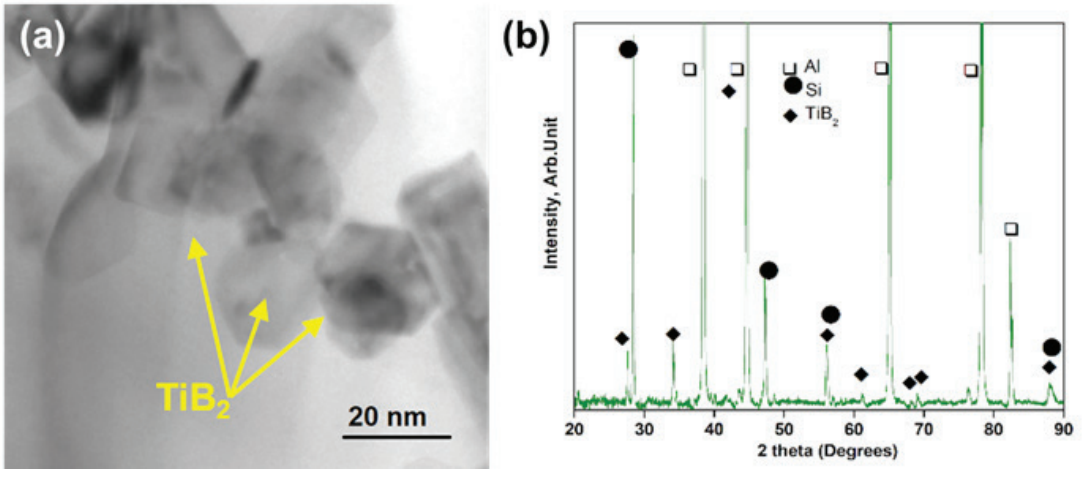

Fig. 2. *a) Bright field TEM microstructure, and b) X-ray diffraction (XRD) pattern of A356/2TiB2 composite sample*

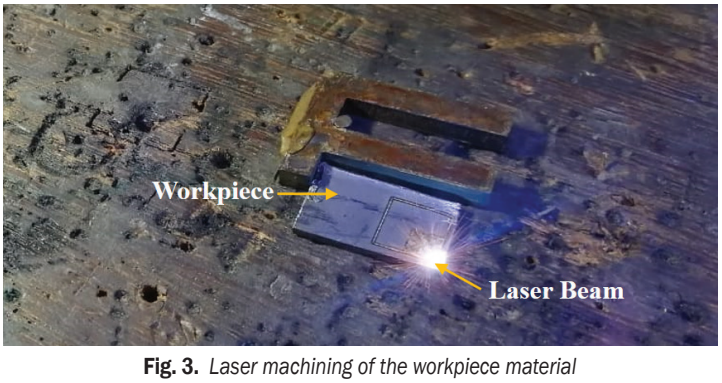

Fig. 3. *Laser machining of the workpiece material*

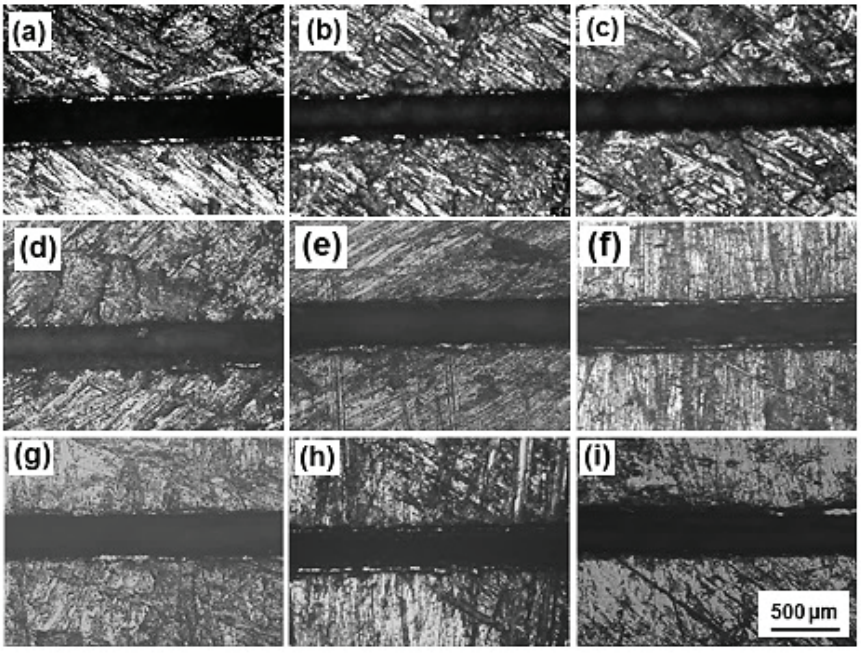

Fig. 4. *Top view of the microchannels obtained for various combinations of LBM parameters; a) experiment 1, b) experiment 2, c) experiment 3, d) experiment 4, e) experiment 5, f) experiment 6, g) experiment 7, h) experiment 8, and i) experiment 9*

generating micro-features with low material removal, high accuracy in dimension, and good surface finish. The heating source in this noncontact machining process is used to heat, melt, and vaporize the material from the work pieces. The advantages of this process are the absence of tool wear, no force exerted on the workpiece, fast processing, and precision machining. Therefore, LBM is chosen for machining microchannels in Al/TiB_2 composite.

Microchannels were machined on the nano-composite samples using the Nd: YAG Q switched laser beam machining system made by Lee Lasers, USA. This laser machine uses argon as the assist gas that passes coaxially with the laser beam through a conical nozzle. The parameters including nozzle diameter, focal length of the lens, and nozzle stand-off distance were all kept constant during the experiments. Laser machining of the workpiece material is shown in Fig. 3.

The input process parameters that were varied while conducting the experiments are laser power, frequency, assist gas pressure, and cutting speed. The input process parameters and their levels are given in Table 1.

2 RESULTS

The bright field optical micrograph of the microchannels machined using LBM is shown in Fig. 4 and the cross-sectional view of the same are shown in Fig. 5. This microscope is a polarized light microscope with a charge-coupled device (CCD) camera and has a magnification in the range of 100× to 1000×.

Table 1. *Input process parameters and their levels*

Factor	Designation of input parameters	Level		
		1	2	3
Power [kW]	A	5	7	9
Frequency [kHz]	B	3	4	5
Gas pressure [bar]	C	2	4	6
Cutting speed [mm/min]	D	100	150	200

The laser beam machined microchannels were examined using an atomic force microscope (AFM) to obtain the profile and value of surface roughness. The surface roughness profile images are shown in Fig. 6.

Taguchi's standard orthogonal array (OA) was used to establish the experimental design of a combination of process parameters [29]. The quality loss function used in these experiments is based on "the smaller the better" as the objective of this

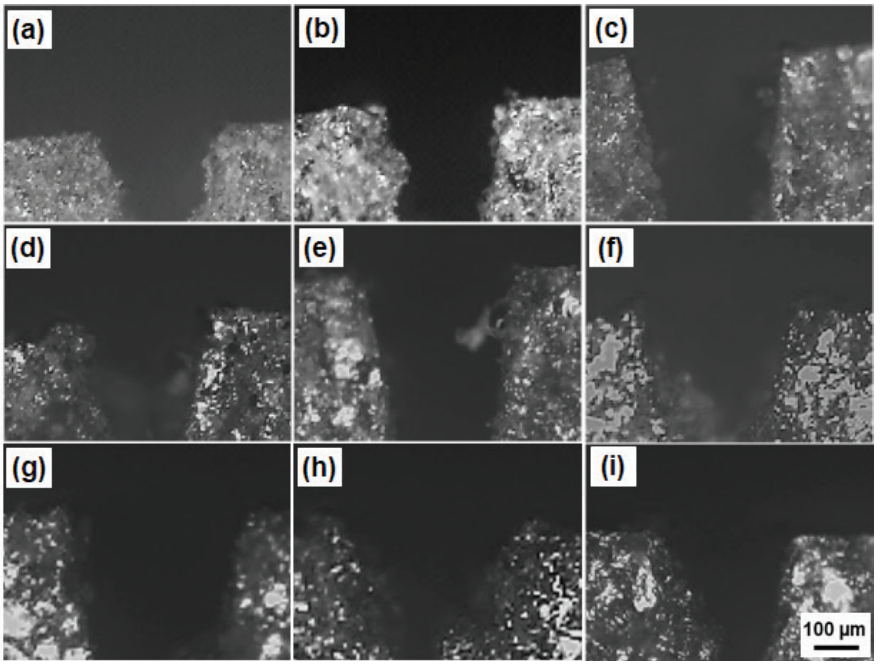

Fig. 5. *Cross-sectional view of microchannels obtained for various combinations of LBM parameters; a) experiment 1, b) experiment 2, c) experiment 3, d) experiment 4, e) experiment 5, f) experiment 6, g) experiment 7, h) experiment 8, and i) experiment 9*

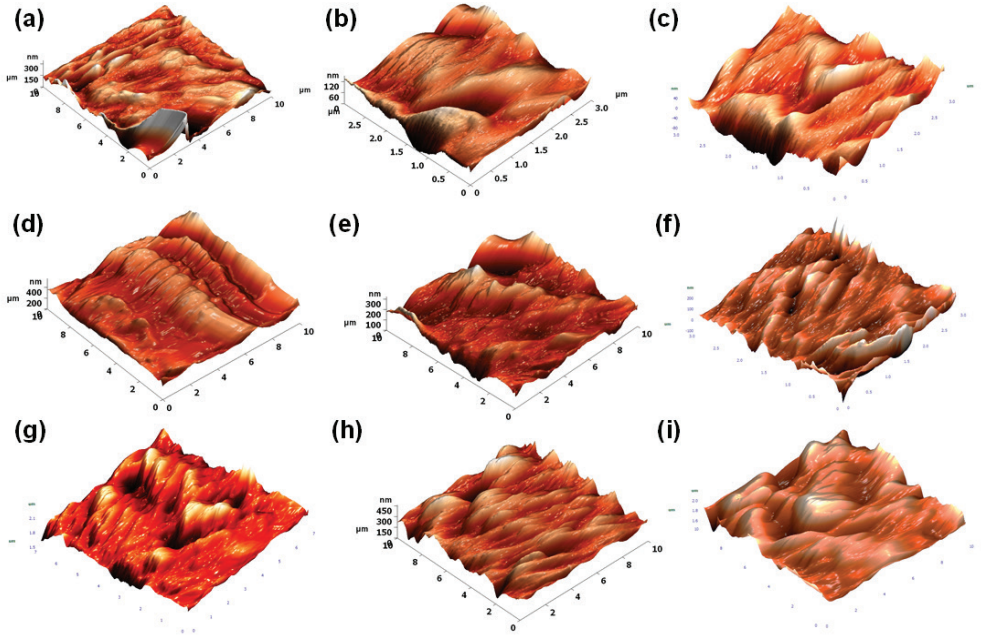

Fig. 6. Surface roughness image of microchannels measured using the AFM; *a) experiment 1, b) experiment 2, c) experiment 3, d) experiment 4, e) experiment 5, f) experiment 6, g) experiment 7, h) experiment 8, and i) experiment 9*

work is to obtain minimum surface roughness of microchannels. The experimental combination of machining parameters and response value (surface roughness) achieved are given in Table 2. The L9 experimental values were statistically examined using the Minitab software based on Taguchi's methodology. A regression equation was obtained for the data to determine the relationship between the input process parameters and the response parameter surface roughness (*Ra*), which is given in Eq. (1).

$$Ra = 349 - 52.9\,A - 81.6\,B - 41.0\,C + 0.329\,D + 10.86\,AB + 4.97\,AC + 3.18\,BC. \quad (1)$$

The predicted values of surface roughness Ra were obtained using Eq. (1) are shown in Table 2. The very low percentage error between the predicted and experimental values of Ra shown in this table indicates the high reliability of the experimental data.

2.1 Analysis of Variance (ANOVA) for Surface Roughness

The following Table 3 shows the ANOVA calculations for surface roughness. The percentage contribution in this table shows that the laser power influences surface roughness to the maximum extent and is then followed by other parameters, such as cutting speed, frequency, and gas pressure. The effect of interaction between the process parameters on *Ra* in the descending order of their effect is power × frequency, power × gas pressure, and frequency × gas pressure. The statistical analysis yielded an R^2 value of 95.13 %, which shows the high accuracy of the experimental data.

2.2. Main Effect Plot for Means for Surface Roughness

The main effect plot for means for surface roughness obtained through the statistical analysis shown in Fig. 7. which shows that the minimum surface roughness of the microchannel is obtained at Level 3 of cutting speed (200 mm/min), Level 1 of gas pressure (2 bar), Level 2 of frequency (4 kHz) and Level 1 (5 kW) of laser power. The main effect plots for means show the trend of the influence of the individual input process parameters on surface roughness. The surface roughness is also influenced by the effect of interaction between the input process parameters also. Thus, the contour plots were obtained for this purpose and the effect of the interaction of two process parameters on surface roughness when the other input parameters are kept constant at their optimum level was studied.

2.3 Contour Plots and Parametric Studies for Surface Roughness

The contour plots shown in Fig. 8 are used to study the influence of interaction between the input process parameters on surface roughness (*Ra*). The effect of interaction between cutting speed and pulse frequency

Table 2. *Experimental combination of machining parameters, experimental and predicted values of Ra and error in percentage*

Experiment number	Input parameter				Response value [nm]		Error [%]
	A	B	C	D	Surface roughness		
					Experiment	Predicted	
1	5	3	2	100	21.5	22.28	0.035
2	5	4	4	150	11.23	10.93	0.027
3	5	5	6	200	11.76	12.3	0.044
4	7	3	4	200	40.67	41.08	0.010
5	7	4	6	100	27.98	28.34	0.013
6	7	5	2	150	18.89	19.53	0.033
7	9	3	6	150	51.75	50.29	0.029
8	9	4	2	200	37.63	36.16	0.065
9	9	5	4	100	67.403	65.02	0.037

Table 3. *Results of ANOVA for Ra*

Source	Degrees of freedom	Sum of squares	% Contribution	F-Value	P-Value
Regression	7	5761.32	95.13	2.06	0.0491
Power	1	3904.61	67.96	1.40	0.0946
Frequency	1	23.19	1.70	1.76	0.0411
Gas pressure	1	161.43	1.04	1.33	0.155
Cutting speed	1	401.56	4.11	1.25	0.0464
Power × Frequency	1	426.07	11.93	1.03	0.0495
Power × Gas pressure	1	644.85	6.66	2.12	0.383
Frequency × Gas pressure	1	199.61	1.71	0.50	0.0608
Error	1	398.73	4.87		

on *Ra* is shown in Fig. 8 a. The region is found between Levels 1 and 2 of frequency and Level 1 of cutting speed and between Levels 2 and 3 of frequency and Levels 2 and 3 of cutting speed. The minimum region for surface roughness is obtained for the combination of high pulse frequency × high cutting speed and for low pulse frequency × low cutting speed. In the pulsed mode laser cutting, the extent of spot overlap influences the surface roughness. The combination of pulse frequency and cutting speed mainly decides the extent of spot overlap. The greater the spot overlap, the smoother the cut edge surface will be. The above combinations result in a high level of spot overlapping and continuous power density per unit length, which gives complete cutting with a uniform smooth surface. The influence of the interaction effect of laser power and cutting speed on *Ra* is shown in Fig. 8b. The region that yields minimum *Ra* is Levels 1 and 2 of laser power and all the levels of cutting speed. According to the results of the study, a medium level of laser power combined with high cutting speed generates a surface with minimum surface roughness. This combination provides just sufficient time of exposure of the work material to the laser.

The influence of the interaction effect of cutting speed and gas pressure on *Ra* is shown in Fig. 8c. The levels that yield minimum surface roughness is Level 1 of gas pressure and level 2 of cutting speed. The combination of low gas pressure and medium cutting speed leads to minimum surface roughness. Medium cutting speed provides adequate exposure of the work material to the laser, and minimum gas

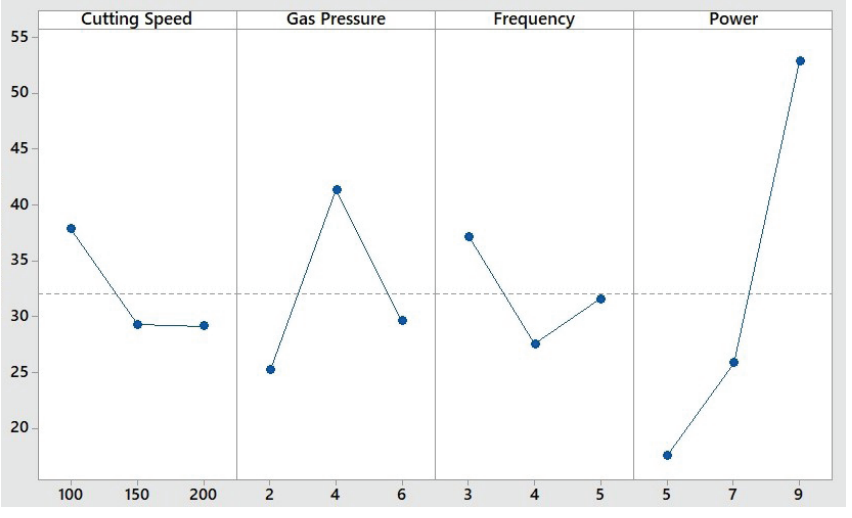

Fig. 7. *Main effect plots for means - Input process parameters vs. surface roughness (Ra)*

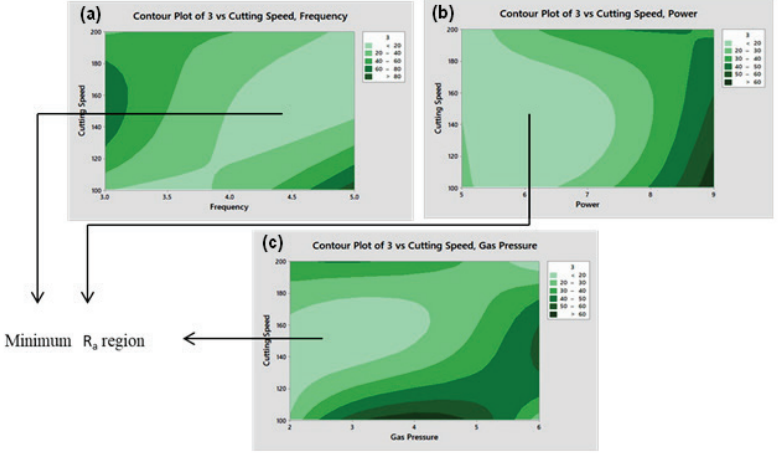

Fig. 8. *Contour Plots for a) Ra vs. cutting speed × pulse frequency, b) Ra vs. laser power × cutting speed, and c) Ra vs. cutting speed × gas pressure*

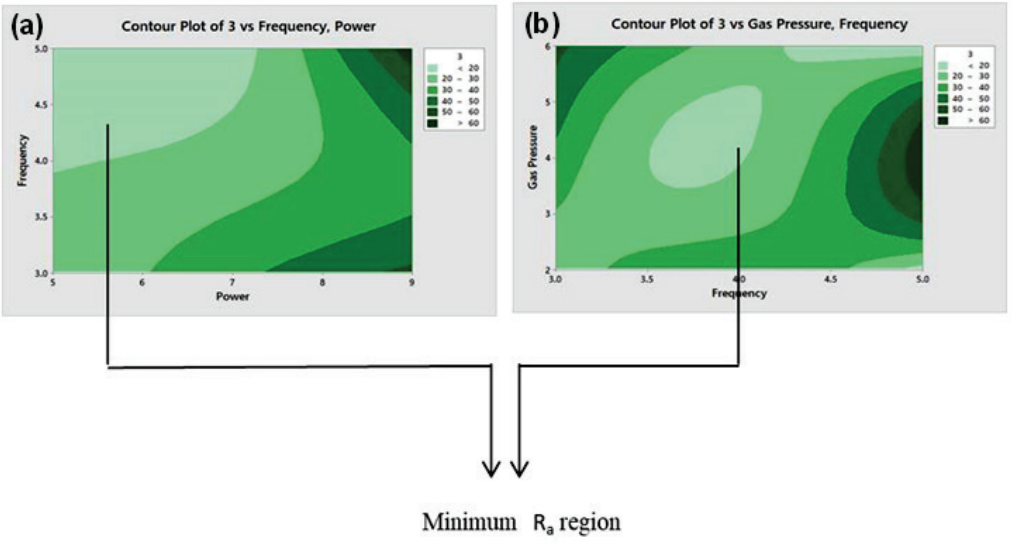

Fig. 9. *Contour plots for a) Ra vs. Pulse frequency × Laser power, and b) Ra vs. Gas pressure × Pulse frequency*

pressure prevents the solidification of the material in the channel itself. This improves the surface finish of the microchannel.

Fig. 9a show the effect of the interaction between pulse frequency and laser power on *Ra*. The region that yields minimum *Ra* is found between Levels 2 and 3 of pulse frequency and Levels 1 and 2 of laser power. Moderate laser power with high frequency allows for an adequate amount of exposure of the work material to the laser for ablation and thus provides minimum roughness on the machined surface. The influence of the interaction effect of gas pressure and pulse frequency on *Ra* is shown in Fig. 9b. The levels that yield minimum *Ra* are found between Levels 1 and 2 of gas pressure and Level 3 of pulse frequency. Moderate gas pressure combined with high frequency also leads to an adequate amount of exposure of the work material to the laser thus producing minimum surface roughness.

3 CONCLUSIONS

Experimental investigations were performed to study the influence of laser machining parameters on the surface roughness of microchannels on Al/TiB_2 composite. Laser machining is an excellent choice for machining micro-features on advanced composite materials like Al/TiB_2. The important findings of the work are summarised as follows.

The surface roughness images of the microchannels obtained using the atomic force microscope revealed that the laser micromachining of Al/TiB_2 composite resulted in surface roughness values ranging from 11.23 nm to 67.403 nm. The main effect plots for means show the optimum combination of laser machining parameters to produce a minimum surface roughness value are a cutting speed of 200 mm/min, a gas pressure of 2 bar, a frequency of 4 kHz, and a laser power of 5 kW. The effect of input process parameters on Ra in the descending order of their influence is laser power, cutting speed, frequency, and gas pressure.

Although the main effect plots for means show the trend of the influence of the individual input process parameters on surface roughness, the output process parameter is also influenced by the effect of interaction between the input process parameters. Thus, contour plots were obtained for this purpose, and the effect of the interaction of two process parameters on surface roughness when the other input parameters are kept constant at their optimum level was studied.

The effect of interaction between the input process parameters on Ra in the descending order of their influence is power × frequency, power × gas pressure, and frequency × gas pressure.

4 ACKNOWLEDGEMENTS

The authors thank the management of PSG College of Technology, Coimbatore, for their financial support in conducting experiments.

5 REFERENCES

[1] Dhupal, D., Doloi, B., Bhattacharyya, B. (2008). Pulsed Nd: YAG laser turning of micro-groove on aluminum oxide ceramic (Al203). International Journal of Machine Tools and Manufacture, vol. 48, no. 2, p. 236-248, **DOI:10.1016/j.ijmachtools.2007.08.016**.

[2] Khot Rahul, S., Venkateshwara Rao, T., Harshad, N., Girish, H., Ishigaki, T., Madhusudan, P. (2021). An Investigation on Laser Welding Parameters on the Strength of TRIP Steel. *Strojniški vestnik - Journal of Mechanical Engineering*, vol. 67 no. 1-2, p. 45-52, **DOI:10.5545/sv-jme.2020.6912**.

[3] Li, L. (1994). Three-dimensional laser micromachining. *Microelectronics Technology and Process Integration*, vol. 2335, p. 212-220, **DOI:10.1117/12.186058**.

[4] Gower, M.C. (1998). Industrial applications of pulsed lasers to materials microprocessing. *High-Power Laser Ablation*, vol. 3343, p. 171-182, **DOI:10.1117/12.321564**.

[5] Holmes, A.S. (2001). Laser fabrication and assembly processes for MEMS. *Laser Applications in Microelectronic and Optoelectronic Manufacturing VI*, vol. 4274, p. 297-306, **DOI:10.1117/12.432522**.

[6] Kibria, G., Doloi, B., Bhattacharyya, B. (2014). Investigation into the effect of overlap factors and process parameters on surface roughness and machined depth during micro-turning process with Nd: YAG laser. *Optics & Laser Technology*, vol. 60, p. 90-98, **DOI:10.1016/j.optlastec.2014.01.009**.

[7] Yue, T.M., Lau, W.S. (1996). Pulsed Nd: YAG laser cutting of Al/Li/SiC metal matrix composites. *Material and Manufacturing Process*, vol. 11, no. 1, p. 17-29, **DOI:10.1080/10426919608947458**.

[8] Qiao, H., Zhihe, C., Jianfeng, C., Zhao, J. (2021). Experimental study on water jet guided laser micro-machining of mono-crystalline silicon. *Optics & Laser Technology*, vol. 140, art. ID 107057, **DOI:10.1016/j.optlastec.2021.107057**.

[9] Cao Z.H., Qiao, H.C., Zhao, J.B. (2020). Experimental study on laser water-jet machining of metal material. *Opto-Electronic Engineering*, vol. 47, no. 2, p. 190423-1, DOI:10.12086/oee.2020.190423. (in Chinese)

[10] Yu, Y.F., Qiao, H.C, Cao, Z.H., Zhao, J.B., Zhang, Y.N., Wu, J.J. (2020). Effect of water-guided laser machining technology on micro-morphology of 316L stainless steel. *Opto-Electronic Engineering*, vol. 47, no. 11, p. 190654-1, **DOI:10.12086/oee.2020.190654**. (in Chinese)

[11] Posa, V., Vardhan, M., Sundaram, (2021). Experimental study of micromachining on borosilicate glass using CO_2 laser. Journal of Manufacturing Science and Engineering, vol. 143, no. 5, art. ID.051007, **DOI:10.1115/1.4048639**.

[12] Demarbaix, A., Ducobu, F., Juste, E., Petit, F., Duterte, C., Rivière-Lorphèvre, E. (2021). Experimental investigation on green ceramic machining with nanosecond laser source. *Journal of Manufacturing Processes*, vol. 61, p. 245-253, **DOI:10.1016/j.jmapro.2020.11.031**.

[13] Pramanik, D., Kuar, A.S., Sarkar, S., Mitra, S. (2020). Evaluation of sawing approach of hole quality characteristics in low power fiber laser trepan drilling of monel k-500 superalloy sheet. *Optik*, vol. 224, art. ID 165642, **DOI:10.1016/j.ijleo.2020.165642**.

[14] Muthuramalingam, T., Akash, R., Krishnan, S., Phan, N.H., Pi, V.N., Elsheikh, A.H. (2021). Surface quality measures analysis and optimization on machining titanium alloy using CO_2 based laser beam drilling process. *Journal of Manufacturing Processes*, vol. 62, p. 1-6, **DOI:10.1016/j.jmapro.2020.12.008**.

[15] Shrivastava, P.K., Pandey, A.K. (2018). Optimization of machining parameter during the laser cutting of Inconel-718 sheet using regression analysis based particle swarm optimization method. *Materials Today: Proceedings*, vol. 5, no. 11, p. 24167-24176, **DOI:10.1016/j.matpr.2018.10.211**.

[16] Deng, B., Peng, F., Zhou, L., Yan, R., Wang, H., Yang, M. (2021). Study on the surface layer formation of aluminum matrix composites and associated machinability in precision milling based on laser melting modification. *Journal of Manufacturing Processes*, vol. 62, p. 670-684, **DOI:10.1016/j.jmapro.2020.12.071**.

[17] Boujelbene, M. (2018). Influence of the CO_2 laser cutting process parameters on the quadratic mean roughness Rq of the low carbon steel. *Procedia Manufacturing*, vol. 20, p. 259-264, **DOI:10.1016/j.promfg.2018.02.038**.

[18] Boujelbene, M., El Aoud, B., Bayraktar, E., Elbadawi, I., Chaudhry, I., Khaliq, A., Elleuch, Z. (2021). Effect of cutting conditions on surface roughness of machined parts in CO_2 laser cutting of pure titanium. *Materials Today: Proceedings*, vol. 44, p. 2080-2086, **DOI:10.1016/j.matpr.2020.12.179**.

[19] Cekic, A., Begic-Hajdarevic, D., Kulenovic, M., Omerspahic, A. (2014). CO_2 laser cutting of alloy steels using N_2 assist gas. *Procedia Engineering*, vol. 69, p. 310-315, **DOI:10.1016/j.proeng.2014.02.237**.

[20] Kim, J., Zani, L., Abdul-Kadir, A., Jones, L., Roy, A., Zhao, L., Silberschmidt, V.V. (2022). Hybrid-hybrid machining of SiC-reinforced aluminium metal matrix composite. *Manufacturing Letters*, vol. 32, p. 63-66, **DOI:10.1016/j.mfglet.2022.04.002**.

[21] Bahrami, M., Yovanovich, M.M., Culham, J.R. (2006). Pressure drop of fully developed, laminar flow in rough microtubes, *Journal of Fluids Engineering*, vol. 128, no. 3, p. 632-637, **DOI:10.1115/1.2175171**.

[22] Chen, J.P., Gu, L., He, G.J. (2020). A review on conventional and nonconventional machining of SiC particle-reinforced aluminium matrix composites. *Advances in Manufacturing*, vol. 8, p. 279-315, **DOI:10.1007/s40436-020-00313-2**.

[23] Nampoothiri, J., Harini, R.S., Nayak, S.K., Raj, B., Ravi, K.R. (2016). Post in-situ reaction ultrasonic treatment for generation of Al-4.4 Cu/TiB_2 nanocomposite: A route to enhance the strength of metal matrix nanocomposites. *Journal of Alloys and Compounds*, vol. 683, p. 370-378, **DOI:10.1016/j.jallcom.2016.05.067**.

[24] Nampoothiri, J., Raj, B., Ravi, K.R. (2015). Role of ultrasonic treatment on microstructural evolution in A356/TiB_2 in-situ composite. *Transactions of the Indian Institute of Metals*, vol. 68, p. 1101-1106, **DOI:10.1007/s12666-015-0653-2**.

[25] Nampoothiri, J., Balasundar, I., Raghu, T., Ravi, K. R. (2020). Structural and mechanical behavior of Al-4.4 Cu/2TiB_2 in-situ nanocomposites fabricated by post-in-situ reaction ultrasonic processing. *Metallurgical and Materials Transactions B*, vol. 51, p. 149-160, **DOI:10.1007/s11663-019-01713-x**.

[26] Mandal, A., Chakraborty, M., Murty, B.S. (2008). Ageing behaviour of A356 alloy reinforced with in-situ formed TiB2

particles. Materials Science and Engineering: A, vol. 489, no. 1-2, p. 220-226, **DOI:10.1016/j.msea.2008.01.042**.

[27] Kumar, S.D., Mandal, A., Chakraborty, M., (2015). On the age hardening behavior of thixoformed A356-5TiB_2 in-situ composite. *Materials Science and Engineering: A*, vol. 636, p. 254-262, **DOI:10.1016/j.msea.2015.03.076**.

[28] Chen, J. Yu, W., Zou, Z., Li, Z., Chen, D., An, Q., Geng, J., Chen, M., Wang, H. (2021). Effects of in-situ TiB2 particles on machinability and surface integrity in milling of TiB2/2024 and TiB2/7075 Al composites. *Chinese Journal of Aeronautics*, vol. 34, no. 6, p. 110-124, **DOI:10.1016/j.cja.2020.06.017**.

[29] Ross, P.J. (1988) *Taguchi Techniques for Quality Engineering*. McGraw Hill, New York.

Strojniški vestnik - Journal of Mechanical Engineering 68(2022)12, 746-756
DOI:10.5545/sv-jme.2022.273
Original Scientific Paper
Received for review: 2022-07-07
Received revised form: 2022-10-03
Accepted for publication: 2022-10-17

Investigation of Machining Parameters in Thin-Walled Plate Milling Using a Fixture with Cylindrical Support Heads

Muthu Mekala Natarajan[1] – Balamurugan Chinnasamy[1] – Bovas Herbert Bejaxhin Alphonse[2]
[1] Anna University, College of Engineering Guindy, India
[2] SIMATS, Saveetha School of Engineering, India

Construction, processing, biomedical instruments, electronics, automobiles, and aerospace widely use thin-wall parts. Mostly, these thin-walled parts are machined using either a peripheral milling machine or an end milling machine with the help of fixtures. In this study, three different material thin-walled parts (i.e., Inconel 718, AISI 316L, and Al 6061) are machined in end milling using a newly designed fixture with cylindrical heads, and the surface roughness and deformation with different machining parameters are compared. The optimum values of the machining parameters feed, speed, and depth of cut have been found to improve the surface roughness of thin-walled plates by arresting the deformation using the proposed fixture. Analysis of variance (ANOVA) results show that the speed is the most influential parameter in the case of displacement for AISI 716L and Al 6061, feed is the most influential parameter in the case of surface roughness for Inconel 718 and AISI 716L, and speed is the most influential parameter in the case of displacement and surface roughness for Al 6061. The use of fixtures provides a significant reduction in the deformation and surface roughness during the machining in end milling machine.
Keywords: end-milling, fixture, surface roughness, deformation

Highlights
- *A new milling fixture with sliding jaws was designed and developed to reduce the surface roughness in workpieces.*
- *The experimental model is verified with the three levels of input parameters.*
- *The experimental result values of displacement and surface roughness correlated well with the simulated displacement values.*
- *The cylindrical support heads in the milling fixture reduce the surface roughness to a greater extent.*

0 INTRODUCTION

Thin-walled parts are widely used in the automobile industry, aerospace, precision processing, and medical care to meet specific needs, such as improved performance, aesthetics, and weight. Generally, thin-walled parts are considered to be lightweight and the thickness-to-profile ratio is less than 1:20; they also elastically deform during machining due to low stiffness. The complex geometric shapes of thin-walled parts with significant deformation are no longer machined in milling machine because the surface roughness of thin-walled parts directly impact wear resistance, fatigue strength, corrosion resistance, and friction. The surface roughness of the milled profile is the function of feed and the geometry of the tool profile under ideal circumstances. In actual cases, the deflection, work-tool system vibration, chatter, and built-up edge formation all affect the surface roughness generated in the end milling process. Thus, it is necessary to relate the surface roughness with primary machining parameters, such as speed, feed, and axial depth of cut. The fixtures and jigs are used in the milling operation, which significantly reduce deformation and hence achieve a good surface finish.

Hao and Liu **[1]** investigated the surface milling of curved thin-walled parts to predict the surface roughness and physical factors. They demonstrated that the surface roughness prediction model had an error of less than 13 %. Cheng et al. **[2]** explored surface roughness in the feed direction, transverse surface roughness, and deformation while milling Al alloy 5083; they investigated the impact of cutting parameters on both surface roughness and machining deformation. Zahaf and Benghersallah **[3]** experimentally evaluated the vibration and surface roughness in the end-milling of annealed and hardened bearing steel; they also compared statistical analysis, mathematical modelling, and optimization. They showed the results that the cutting speed and feed per tooth are the influential elements in the milling surface roughness evaluation in the steel workpiece. Sharma and Dwivedi **[4]** examined the aspects that influence surface roughness in milling; they showed the results that the three primary process parameters that affect the end-milling process of aluminium alloy are feed rate, depth of cut, and spindle speed. Kumar et al. **[5]** have experimentally determined the effect of machining settings on the surface roughness of aluminium metal matrix composites; the most significant milling parameters, according to their research, are 0.1 mm/rev feed rate, 3000 rpm spindle speed, and 0.2 mm cut depth, with 86.6 %, 9.75 %, and 6.16 % contributions, respectively.

*Corr. Author's Address: Anna University, College of Engineering Guindy, India, muthumekalagunalan@annauniv.edu

Lan et al. [6] proposed an intelligent mirror milling machine to mitigate deformation and vibration in the end-milling of large thin-plate workpieces; they have devised a viable way for determining a support head's movement path under a specified cutting path. Bao et al. [7] investigated the forming mechanism of surface topography and the effect of support locations on aircraft skin parts in mirror-milling; they demonstrated that mechanical surface topographies with diverse features may be generated using the same processing parameters by related location between the support head and the milling head. Fei et al. [8] suggested a new method of deformation suppression that involves supporting a fixture element on the back surface of the workpiece at the projection area of the tool-workpiece contact zone; they demonstrated that the method used reduces machining error, improves surface quality, and thus reduces the deformation of low-rigidity workpieces during machining. Bao et al. [9] validated the measurements of milling force for the mirror milling of aircraft skin with the proposed milling force model. They have also developed a finite element m″SPEEethod (FEM) model to calculate the deformation in the mirror milling of an aluminium plate; they also analysed the position of support heads' locations used in the mirror milling process. Sallese et al. [10] presented the key design considerations and also the characteristics of the black-box control logic employed in the new active fixture; they concluded that the reduction obtained allows for deeper cut depths with lower vibration levels, potentially enhancing production.

A multi-point location/support algorithm was developed by Junbai and Kai [11] to solve positions of a flexible tooling system's location and support spheres in order to construct the workpiece's envelope surface while avoiding machine tool interference. The tooling system, which is said to be flexible, meets the needs of large-scale thin-wall workpiece machining in aircraft while minimizing manufacturing error and cycle time. Amaral et al. [12] created an algorithm using ANSYS parametric design language code; they showed that the algorithm optimizes the supports of the fixture, clamp placements, and clamping forces. Also, they showed the results that the reduced deformation improves the machining accuracy. Finite element analysis (FEA) in the computer-aided fixture design environment minimizes the need for extensive "trial and error" experiments on the shop floor. Shi et al. [13] analysed the response of a thin-walled component over the variable thickness in the milling process using the first shear deformation theory and the Lagrange equation. They observed that increasing the slope of the thickness variation, and length and decreasing the width improves the workpiece's dynamic deformation. Chang and Lu [14] presented a feasibility study predicting the surface roughness inside milling operations using different polynomial networks. They concluded that the developed polynomial network models possess promising potential for predicting surface roughness inside milling operations. Yuan et al. [15] presented an accurate surface roughness model based on cutting process kinematics and tool geometry, taking into account the effects of tool run-out and minimum thickness. They demonstrated that the surface roughness model's proposed results could accurately predict the trends and magnitude of surface roughness in micro end-milling.

Xiao et al. [16] performed a turning test on stainless steel using the central composite surface design and the Taguchi design; they suggested that the feed rate impact on surface roughness is highly predominant. They showed the results that the cutting depth ranks second, and cutting speed has the least impact. Yuan et al. [17] studied the auxiliary device capable of providing double-sided support to the tenuously rigid places between the cutter and the workpiece to reduce chatter vibrations in the thin-wall milling of half-opened side walls. They concluded that the quality of the machined surface in the presence of the support device is superior to that of the machined surface in the absence of the support device. Zhao et al. [18] constructed a posture accessibility and a stability diagram based on geometric analysis and machining dynamic analysis by identifying interference and chatter-free cutter postures. Also, they propose a novel surface roughness prediction model by exploring the correlation between surface roughness and maximum cutter deformation force. Maiyar et al. [19] investigated the parameter optimization of Inconel 718 superalloy end milling operations using multi-response criteria based on the Taguchi orthogonal array and grey relational analysis. Jing et al. [20] investigated the effects of micro-end-milling cutting parameters on machined surface roughness to determine the best operating conditions. Muthu Mekala et al. [21] designed and developed a new fixture to minimize the surface roughness in the end milling of Al6061 workpiece. They concluded that the proposed fixture with the support heads greatly reduces the deformation in the work piece, which significantly impacted the surface quality.

Shaik and Srinivas [22] assessed the influence of machining process variables comprising cost, cutting speed, and axial depth of cut on output variables like surface roughness and tool vibration amplitude in an

Al-6061 workpiece; they developed an interactive platform to evaluate the ideal process parameter combination using a multi-objective approach and neural network models. Wanner et al. [23] stated that a well-designed tool-to-workpiece offset geometry could result in a reliable and noise-free operation while milling thin-walled Inconel 718. They proved that adjusting the tool's offset location helped lessen chatter vibrations in the system. Wu and Lei [24] studied the possibility of using signal characteristics in milling vibration measurements and cutting parameters to predict the surface roughness of S45C stee; their experiments revealed that the vibration behaviour affects the surface roughness in addition to cutting parameters. Yue et al. [25] summarised current research on how to achieve stable chatter prediction, chatter identification, and chatter control/suppression during the milling process. They concluded with some reflections regarding possible directions for future research in this field. Alauddin et al. [26] investigated the incorporation of a surface-roughness model for end-milling 190 BHN steel. They observed that the feed effect is predominant in the first- and second-order models.

In the above literature, it is evident that many researchers have test various methods to improve the surface roughness of thin-walled parts by optimizing the machining parameters such as feed, speed, and depth of cut (doc) when machining in end milling. Therefore, the main goal of this research work is to reduce the workpiece deformation with the use of the proposed fixture and also optimizing the machining parameters, including feed, speed, and depth of cut, to improve the surface roughness of thin-walled plates made of three different materials (Inconel 718, AISI 316L, and Al 6061) in a milling machine. Also, the DEFORM 3D model is simulated prior to the experiment, and the significance of variables on the multiple performance characteristics is further investigated using ANOVA results.

1 METHODS

Aircraft wings, automobile bodies, and turbine blades are all machined with computer navigated control (CNC) milling machines. While milling thin-walled components, the milling process causes more deformation, which leads to poor surface roughness. Hence jigs and fixtures are employed to reduce deformation. They minimize the surface roughness in the thin-wall plates during the time of machining. These fixtures will hold the workpiece in place during the machining process, limiting the amount of deformation. The machining settings are critical to achieving surface roughness optimization. The machining parameters are spindle speed, feed rate, depth of cut, coolant flow, drill tool diameter, cutting speed, and the number of passes. Among the input parameters, the speed of the spindle, depth of cut, and the feed rate affect the surface finish to a greater extent. Table 1 gives the detailed required input cutting parameters for machining.

Table 1. *Cutting parameters and their ranges*

Parameters	Values		
Speed [rpm]	800	950	1050
Feed rate [mm/rev]	0.05	0.10	0.15
Depth of cut [mm]	0.1	0.2	0.3

In this study, the three different thin-walled plate materials selected are Inconel 718, Stainless steel AISI 316L, and Aluminium alloy Al6061. The requirement of good corrosion-resistant for various applications is the basis for using these materials, but the drawback is more deformation while machining because of low rigidity. This drawback is resolved by the fixture for the milling machine and optimizing the selected machining parameters. The dimensions of all three thin-walled plate materials used for the study are Inconel 718 100 mm × 50 mm × 5 mm, AISI 316L 100 mm × 50 mm × 5 mm, and Al6061 100 mm × 100 mm × 5 mm for the length, width, and thickness, respectively. The chemical compositions of the workpieces play a vital role in selecting the desired input parameters. Fig. 1 shows the nomenclature of the cutting tool. The material of the cutting tool used in this end-milling is high-speed steel (HSS). The width of the cutting tool is 8 mm, and the length is 65 mm.

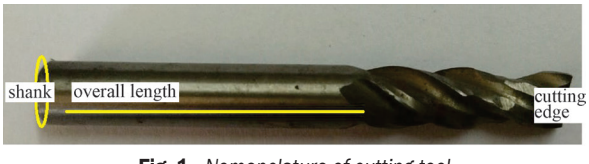

Fig. 1. *Nomenclature of cutting tool*

2.1 Design of Fixture and Simulation of Workpiece Deformation

The main parts of milling fixtures are locators, clamps, and supports or support heads. The milling fixture is designed in such a way as to hold the thin-walled plate and avoids chatter during the milling process. The thin-walled workpieces widely use cylindrical

support heads. The high carbon steel is the material used for the attached support heads of the fixtures. Fig. 2 shows the designed fixture with nomenclature and dimensions. This fixture is fixed in the end-milling bed, and the workpiece is subjected to the milling operation. The theoretical values of workpiece deformation are initially predicted with DEFORM 3D simulation software. The simulation uses the same fixture design, end-milling machine, milling cutter, and workpiece similar to the shop floor experiment. The cylindrical support heads in the fixtures reduce the maximum deformation observed during the machining. The input parameters of machining speed, feed rate, and the depth of cut assess the prediction of deformation of the workpiece are the machining speed, feed rate, and the depth of cut, as indicated in Table 1. The parameters are considered to avoid the maximum deformation by reducing the chatter during the milling process.

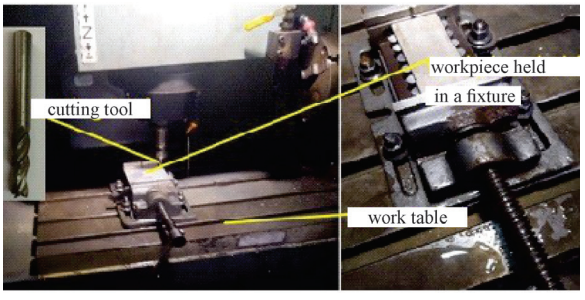

Fig. 2. *Experimental setup*

2.2 Experiment

The vertical milling machine of model Chetak 75M machining centre is employed to perform the end milling operations on the three workpieces. Fig. 3 shows how the proposed newly designed fixture is fixed on the CNC milling machine table using a bench vice. Initially, the thin-walled plate workpiece material of Inconel 718 is fixed on the support heads of the fixture by using various tools and supports. Primarily, the three input parameters considered here for the experiment are feed, depth of cut, and speed. The three different combination values of feed and depth of cut with the different spindle speed values are applied to run the experiments in the end-milling machine. The other workpieces (Stainless steel AISI 316L and the aluminium alloy Al6061) follow a similar experimental procedure. For each experiment, the measurement of the output parameters (surface roughness, displacement, acceleration, frequency, and velocity) is carried out. The SURFTEST SJ-210 portable surface roughness tester measures the average surface roughness for each experiment in the three workpieces under investigation. All other output variables, such as displacement, velocity, acceleration, and frequency, are measured using the HTBB-8215 digital vibration meter. Fig. 4 shows the measuring devices. The fixture usage to reduce the surface roughness in workpieces is evaluated based on the measurements.

Fig. 3. *Measuring devices: vibration meter and surface tester SJ-210*

2.2.1 Design of Experiments

Taguchi's method carries out the design test, which involves analysing data obtained from surface roughness measurements and instantaneous displacement values on the workpiece. The Taguchi method uses a new orthogonal array design to investigate the whole parameter with fewer experiments. With the newly developed fixture, the Taguchi methodology carries the plan of experiments for three elements in three phases for the three workpieces under investigation. Taguchi's L9 orthogonal array defines the nine trial conditions required for the experiment.

2.2.2 ANOVA (Analysis of Variance)

ANOVA is used to investigate the importance of the output response values regarding surface roughness and displacement of the input parameter. Table 2 shows the procedure's parameters and levels. The

present study investigates how different machining parameters affect the machining deformation and surface quality of the product. The present work utilizes MINITAB Software to do experimental data optimization and graphical analysis. The optimal design serves as the basis for the experimental runs, which include nine experiments for each material with the proposed fixture incorporated. The machining parameters used in milling thin-walled plates affect the deformation, quality, and productivity of machined parts.

Table 2. *Input parameters for three different levels*

Input parameters	Unit	Type	Level 1 (L1)	Level 2 (L2)	Level 3 (L3)
Speed	rpm	fixed	800	950	1050
Feed	mm/tooth	fixed	0.05	0.10	0.15
Depth of cut	mm	fixed	0.1	0.2	0.3

3 RESULTS AND DISCUSSION

The Taguchi analysis approach with the values of three levels and three input parameters as shown in Table 1 is employed in the milling operation on three thin-walled plates. Table 2 shows the ranges of input parameters in three different levels (L1, L2, and L3) of experimentation with units and types. A total of nine experiments were carried out on each of three different workpieces using the suggested designed fixture, using the combination of the three machining parameters in MINITAB Software. Table 3 shows the values of simulated displacement found from DEFORM 3D software and experimental values of displacement and surface roughness of the combination of levels by various experimental runs with corresponding input parameters. The following subsections discuss displacement and surface roughness with different outputs from simulation, experimentation, and ANOVA.

Table 3. *Simulation ad experimental values-displacement and surface roughness*

Experiment run	Combination of levels with corresponding input parameters			Material	Experimental displacement [mm]	Displacement simulation [mm]	Surface roughness [μm]
	Speed	Feed	DOC				
1	L1	L1	L1	INCONEL 718	0.019	9.93	0.928
2	L1	L2	L3		0.016	8.44	2.078
3	L1	L3	L3		0.020	9.94	2.768
4	L2	L1	L2		0.014	6.24	2.090
5	L2	L2	L3		0.031	18.5	1.315
6	L2	L3	L1		0.014	4.26	2.485
7	L3	L1	L3		0.025	11.6	2.386
8	L3	L2	L2		0.017	7.19	1.760
9	L3	L3	L2		0.014	4.00	1.552
10	L1	L1	L1	AISI 316L	0.030	20.4	0.565
11	L1	L2	L3		0.026	13.5	1.458
12	L1	L3	L3		0.020	8.54	2.386
13	L2	L1	L2		0.016	6.24	0.958
14	L2	L2	L3		0.020	9.82	0.845
15	L2	L3	L1		0.015	5.99	1.697
16	L3	L1	L3		0.018	9.65	0.428
17	L3	L2	L2		0.022	13.2	1.075
18	L3	L3	L2		0.022	13.7	1.365
19	L1	L1	L1	AL6061	0.030	18.8	1.532
20	L1	L2	L3		0.019	8.6	1.989
21	L1	L3	L3		0.022	12.7	3.090
22	L2	L1	L2		0.016	5.94	2.551
23	L2	L2	L3		0.019	9.62	3.789
24	L2	L3	L1		0.018	9.38	3.620
25	L3	L1	L3		0.016	5.93	3.235
26	L3	L2	L2		0.017	9.80	3.860
27	L3	L3	L2		0.014	4.92	2.719

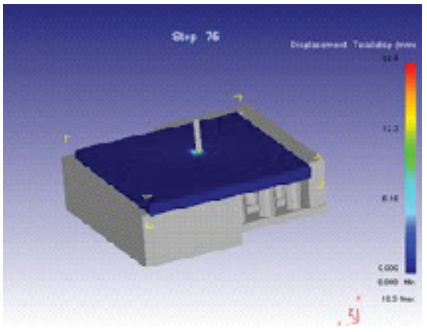

Fig. 4. *Simulation results for Inconel 718 workpiece*

3.1 Comparison of Displacement and Surface Roughness

Fig. 5 shows the comparison of experimental displacement values and surface roughness of three thin-walled plates machined in end-milling machine using the proposed fixture with cylindrical support heads. Nine experiments were carried out on each thin-walled plate with different input parameter combinations. Fig. 5a shows that the displacement trend curve has different behaviour for Inconel when the other two materials show similar trends for the corresponding experimental runs. From Fig. 5b, the minimum surface roughness value of 0.928 µm is measured for the combination of same level's (L1, L1, L1) parameter values. Similarly, for AISI 716L, the minimum surface roughness value measured is 0.565 µm and for AL6061; it is 1.532 µm. For the first three experimental runs, the surface roughness shows a similar trend for all three metals, and then different behaviour is observed for the rest of the experimental runs.

Fig. 6 shows the correlation of experimental displacement, simulated displacement, and surface roughness. It is seen that the displacement trend is similar in both the experimentation and simulation. Also, the surface roughness reduces with the corresponding reduction in displacement values. As seen from the figure, for the experimental samples 6, 11 and 20, the deformations are the peak, as compared to other samples and the corresponding reduction in surface roughness. Hence, the use of fixtures is valid for reducing the deformation in terms of displacement values and the corresponding improvement in surface roughness.

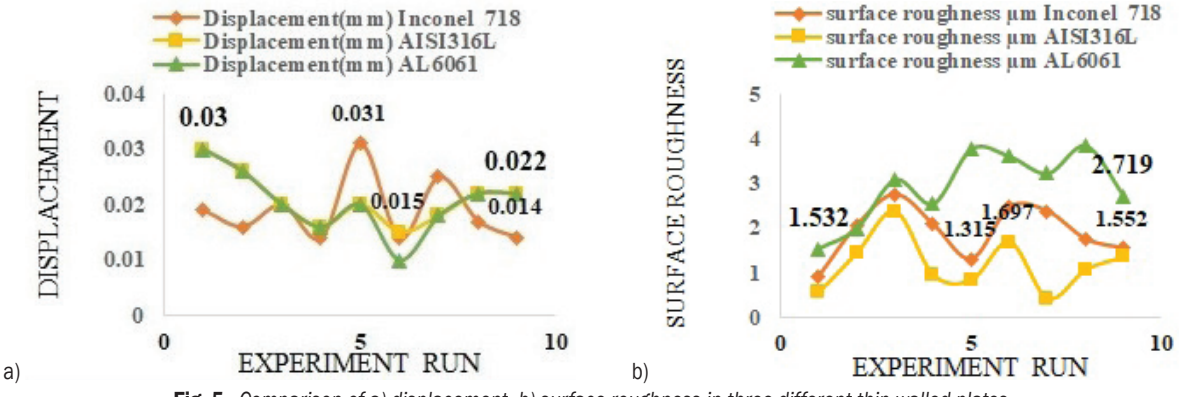

Fig. 5. *Comparison of a) displacement, b) surface roughness in three different thin-walled plates*

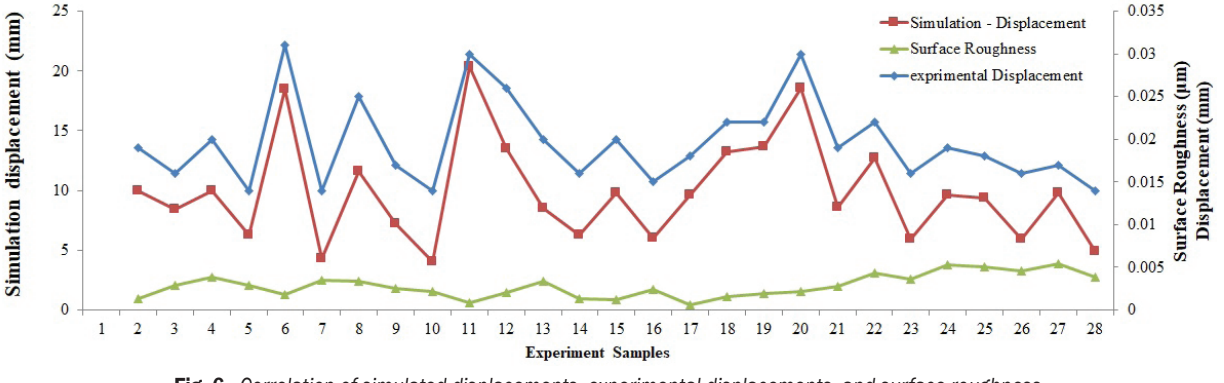

Fig. 6. *Correlation of simulated displacements, experimental displacements, and surface roughness*

3.2 Identification of Influential Parameters by ANOVA

ANOVA helps predict the most influential parameter in the machining with the proposed fixture. The schematic of ANOVA for the displacement of three different materials is given in Table 4. It also shows the most influential input parameters for displacement-measured output responses of the milling process with the use of proposed fixtures for three workpieces. It is inferred from this table that the depth of cut is the most influential input parameter with a contribution of 71.48 % in controlling the displacement for Inconel 718; speed is the most influential input parameter in controlling the displacement by 58.01 % and 58.42 % for AISI 316L and AL6061, respectively. The schematic of ANOVA for the surface roughness of three different materials is given in Table 5. It also shows the most influential input parameters for surface roughness measured output responses of the milling process with the use of proposed fixtures for three workpieces. It is inferred from this table that the feed is the most influential input parameter with contributions of 71.03 % and 70.02 % in controlling the surface roughness for Inconel 718 and AISI 316L, respectively. Speed is the most influential input parameter in controlling the surface roughness by

Table 4. *Scheme of ANOVA for displacement of three different materials*

Material	Source	DF	Adj SS	Adj MS	F-value	P-value	% of contribution	Influential parameter
Inconel 718	Speed	2	0.000003	0.000001	0.10	0.911	1.11	insignificant
	Feed	2	0.000044	0.000022	1.47	0.404	16.30	significant
	Depth of cut	2	0.000193	0.000096	6.53	0.133	71.48	significant and most influential
	Error	2	0.000030	0.000015	-	-	11.11	admissible
	Total	8	0.000269					
AISI 316L	Speed	2	0.000105	0.000052	2.57	0.280	58.01	significant and most influential
	Feed	2	0.000041	0.000020	0.51	0.663	22.65	significant
	Depth of cut	2	0.000014	0.000007	0.34	0.744	7.73	less significant
	Error	2	0.000021	0.000010	-	-	11.60	admissible
	Total	8						
AL6061	Speed	2	0.000104	0.000052	5.57	0.152	58.42	significant and most influential
	Feed	2	0.000013	0.000006	0.68	0.596	0.07	insignificant
	Depth of cut	2	0.000043	0.000021	2.29	0.304	24.16	significant
	Error	2	0.000019	0.000009	-	-	10.67	admissible
	Total	8	0.000178					

Table 5. *Scheme of ANOVA for surface roughness for three different materials*

Material	Source	DF	Adj SS	Adj MS	F-Value	P-Value	% of Contribution	Influential parameter
Inconel 718	Speed	2	0.00623	0.00312	0.00	0.997	0.22	insignificant
	Feed	2	2.00296	1.00148	0.26	0.791	71.03	significant and most influential
	Depth of cut	2	0.52832	0.1411	0.14	0.877	18.74	less significant
	Error	2	0.28220	-	-	-	10.01	admissible
	Total	8	2.81971	-	-	-	-	-
AISI 316L	Speed	2	0.45050	0.000020	0.89	0.530	15.30	less significant
	Feed	2	2.06114	0.000010	4.58	0.179	70.02	significant and most influential
	Depth of cut	2	0.03208	0.000007	0.08	0.928	1.09	insignificant
	Error	2	0.40004	0.000052	-	-	13.5	admissible
	Total	8	2.94676	-	-	-	-	-
AL6061	Speed	2	2.3885	0.000052	5.57	0.152	45.71	significant and most influential
	Feed	2	1.0980	0.000006	0.68	0.596	21.01	significant
	Depth of cut	2	1.3820	0.000009	2.29	0.304	26.45	significant
	Error	2	0.3570	0.127449	-	-	6.83	admissible
	Total	8	-	-	-	-	-	-

45.71 % for AL6061. The contribution factor is the speed for both the displacement and surface roughness from ANOVA in Tables 4 and 5.

Fig. 7 shows the ANOVA graphs for the main plot of the means for displacement and surface roughness for Inconel 718, AISI 316L and Al6061, respectively. From Fig. 7a, the main effect plot for means, for Inconel 718, the optimum parameter conditions are L2L2L3 (speed 950 rpm, feed rate 0.10 mm, and depth of cut 0.3 mm) for displacement and L2L3L3 (speed 950 rpm, feed rate 0.15 mm, and depth of cut 0.3 mm) for surface roughness, as identified from the plots.

From Fig. 7b for AISI 316L, the optimum parameter conditions are L1L2L1 (speed 800 rpm, feed rate 0.10 mm, and depth of cut 0.10 mm) for displacement and L1L3L2 (speed 800 rpm, feed rate 0.15 mm, and depth of cut 0.2 mm) for surface roughness. From Fig. 7c, the optimum parameter conditions are L1L1L1 (speed 800 rpm, feed rate 0.05 mm, and depth of cut 0.1 mm) for displacement and L2LB2C3 (speed 950 rpm, feed rate 0.10 mm, and depth of cut 0.3 mm) for surface roughness.

A grey relational analysis of three metals is given in Table 6, which also gives the optimum machining conditions L2L2C3 for Inconel 718, L1L1L1 condition for AISI 316L and AISI 316L. Based on the ANOVA, the predominant input parameters are speed and feed in the case of milling of AISI 316L, and speed and feed in the case of milling of Al 6061. Hence the optimum speed for the Inconel milling using the fixture is 950 rpm. The surface roughness value measured for Experiment Run 5 with the optimum conditions gives less value around 1.315 µm.

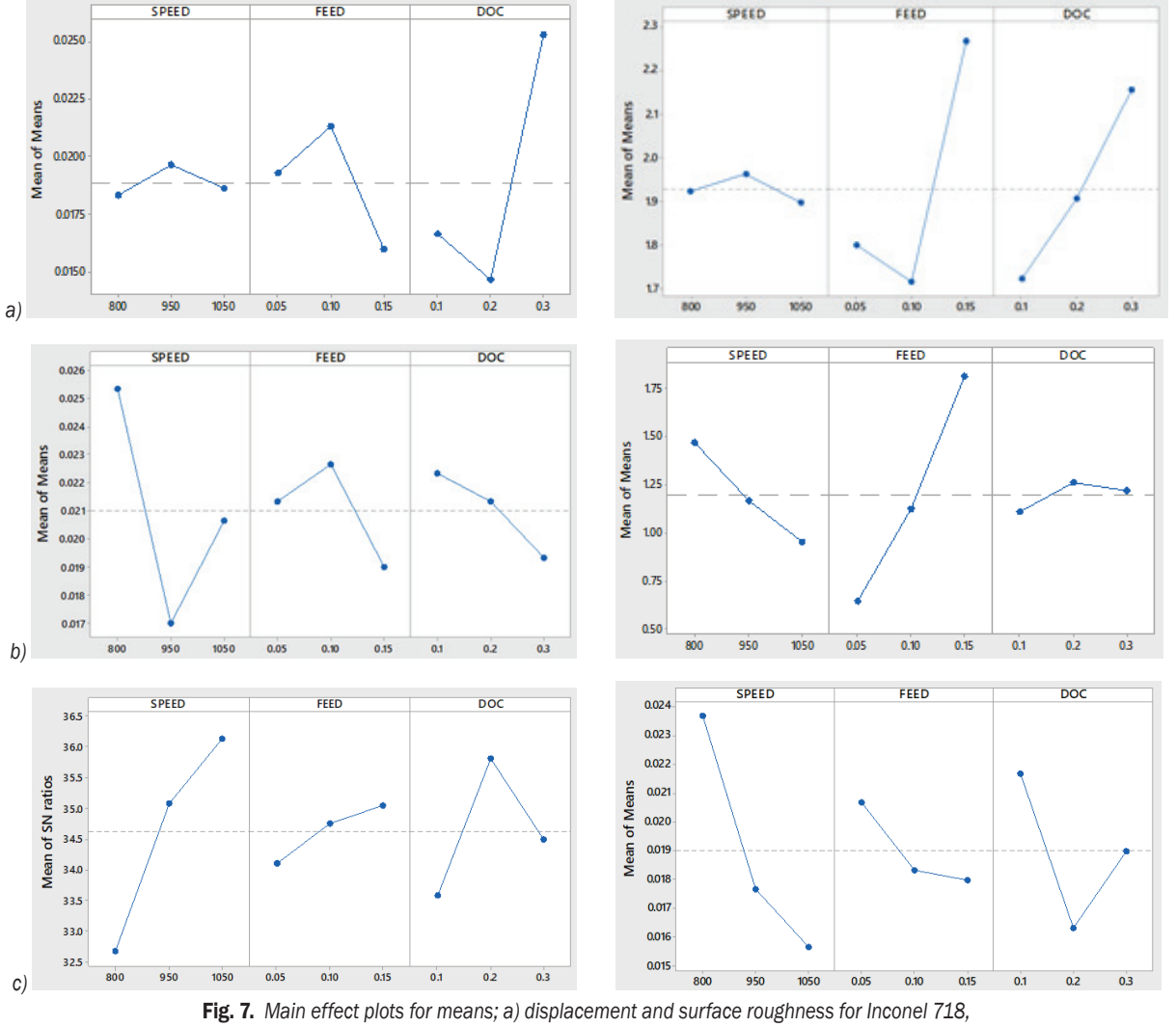

Fig. 7. *Main effect plots for means; a) displacement and surface roughness for Inconel 718, b) displacement and surface roughness for AISI 316L, and c) displacement and surface roughness for Al6061*

Table 6. *Grey relational analysis (GRA)*

Material	Experiment run	Grey relational coefficient for experimental displacement	Grey relational coefficient for displacement simulation [mm]	Grey relational coefficient for surface roughness [μm]	Grey relational grade	Rank
Inconel 718	1	0.414634	0.550076	1	0.235772	2
	2	0.361702	0.620188	0.444444	0.134358	8
	3	0.435897	0.549659	0.333333	0.128205	9
	4	0.333333	0.763962	0.441883	0.129203	6
	5	1	0.333333	0.703902	0.283984	1
	6	0.333333	0.965379	0.371417	0.117458	4
	7	0.586207	0.488215	0.38688	0.162181	7
	8	0.377778	0.694444	0.525114	0.150482	5
	9	0.333333	1	0.595855	0.154865	3
AISI 316L	1	1	0.333333	0.87724	0.368429	1
	2	0.652174	0.489636	0.487307	0.27152	6
	3	0.428571	0.738596	0.333333	0.250083	8
	4	0.348837	0.966465	0.648774	0.327346	3
	5	0.428571	0.652923	0.701289	0.297131	4
	6	0.333333	1	0.435498	0.294805	5
	7	0.384615	0.663139	1	0.341292	2
	8	0.483871	0.499827	0.602091	0.264298	7
	9	0.483871	0.483071	0.51096	0.246317	9
AL6061	1	1	0.333333	1	0.388889	1
	2	0.421053	0.65019	0.718075	0.29822	3
	3	0.5	0.467852	0.427627	0.23258	6
	4	0.363636	0.870229	0.533211	0.294513	4
	5	0.421053	0.592721	0.340251	0.225671	8
	6	0.4	0.60531	0.357934	0.227207	7
	7	0.363636	0.871338	0.405999	0.273496	5
	8	0.380952	0.583618	0.333333	0.216317	9
	9	0.333333	1	0.495108	0.30474	2

Table. 7. *Consolidation of influential input parameters on output results*

Workpiece	Output			
	Displacement		Surface roughness	
	Most influential input parameter	Range of the input factor	Most influential input parameter	Range of the input factor
Inconel 718	Depth of cut	L2L2L3 (speed 950 rpm, feed rate 0.10 mm, and depth of cut 0.3 mm)	feed	L2L3L3 (speed 950 rpm, feed rate 0.15 mm, and depth of cut 0.3 mm)
AISI 316L	Speed	L1L2L1 (speed 800 rpm, feed rate 0.10 mm, and depth of cut 0.10 mm)	feed	L1L3L2 (speed 800 rpm, feed rate 0.15 mm, and depth of cut 0.2 mm)
Al6061	Speed	L1L1L1 (speed 800 rpm, feed rate 0.05 mm, and depth of cut 0.1 mm) for displacement	speed	L2L2l3 (speed 950 rpm, feed rate 0.10 mm, and depth of cut 0.3 mm)

Table 7 gives the consolidation of the influential input parameters on the output results. It has been construed from Table 7 that the speed is the most influential parameter in the case of displacement for AISI 716L and Al 6061. Feed is the most influential parameter in the case of surface roughness for Inconel 718 and AISI 316L. Speed is the most influential parameter in the case of displacement and surface roughness for Al 6061.

5 CONCLUSIONS

The proposed fixture with a cylindrical support head is used in an end-milling machine to produce three thin-walled plates made with three different materials (Inconel 718, AISI 316L, and Al 6061) to reduce the deformation and hence minimize the surface roughness. The cylindrical support heads in the proposed fixture reduce the chatter and vibration

during the milling of thin-walled plates. The author proposes the new fixture design to improve the surface quality by minimizing the deformation caused due to low rigidity. The workpiece-fixture system also suppresses the vibration of thin-walled parts.

The optimum machining parameters (feed, speed, and depth of cut) have been found to improve the surface roughness of thin-walled plates by arresting the deflection using the proposed fixture. ANOVA is performed to investigate the more influential parameters on multiple performance characteristics.

The following conclusions are via simulation and experimentation.

- For Al 6061, speed is the most influential parameter in controlling the displacement and surface roughness, contributing around 58 % and 45 %, respectively.
- The optimum machining conditions for Inconel 718: speed 950 rpm, and depth of cut 0.3 mm. The feed rate range is 0.10 mm to 0.15 mm for the displacement and surface roughness model. It is evident that the grey relational analysis results match with ANOVA in terms of speed and feed rate. The depth of cut is the most influential parameter.
- The optimum machining condition for AISI 316L: speed 800 rpm, feed rate 0.10 mm, depth of cut 0.1 mm for displacement and speed 800 rpm, feed rate 0.15 mm, and depth of cut 0.2 mm for surface roughness.
- Hence, care has been taken to reduce the displacement and surface roughness with the use of the proposed fixture.
- The speed is the most influential parameter in the case of displacement for AISI 716L and Al 6061, feed is the most influential parameter in the case of surface roughness for Inconel 718 and AISI 716L, and speed is the most influential parameter in the case of displacement as well as surface roughness for Al 6061.
- Therefore, the speed and feed are the two most influential parameters (not the depth of cut) to reduce the deformation and the surface roughness using the proposed fixture with cylindrical support heads.

8 REFERENCES

[1] Hao, Y., Liu, Y. (2017). Analysis of milling surface roughness prediction for thin-walled parts with curved surface. *International Journal of Advanced Manufacturing Technology*, vol. 93, p. 2289-2297, **DOI:10.1007/s00170-017-0615-4**.

[2] Cheng, D.J., Xu, F., Xu, S.H., Zhang, C.Y., Zhang, S.W., Kim, S.J. (2020). Minimization of surface roughness and machining deformation in milling of al alloy thin-walled parts. *International Journal of Precision Engineering and Manufacturing*, vol. 21, p. 1597-1613, **DOI:10.1007/s12541-020-00366-0**.

[3] Zahaf, M.Z., Benghersallah, M. (2021). Surface roughness and vibration analysis in end milling of annealed and hardened bearing steel. *Measurement: Sensors*, vol. 13, art. ID 100035, **DOI:10.1016/j.measen.2020.100035**.

[4] Sharma, A., Dwivedi, V.K. (2019). Effect of milling parameters on surface roughness: An experimental investigation. *Materials Today: Proceedings*, vol. 25, p. 868-871, **DOI:10.1016/j.matpr.2019.11.256**.

[5] Kumar, M.B., Parameshwaran, R., Deepandurai, K., Senthil, S.M. (2020). Influence of milling parameters on surface roughness of Al-SiC-B4C composites. *Transactions of the Indian Institute of Metals*, vol. 73, p. 1171-1183, **DOI:10.1007/s12666-020-01960-6**.

[6] Lan, J., Lin, B., Huang, T., Xiao, J.L., Zhang, X.F., Fei, J.X. (2017). Path planning for support heads in mirror-milling machining system. *International Journal of Advanced Manufacturing Technology*, vol. 91, p. 617-628, **DOI:10.1007/s00170-016-9725-7**.

[7] Bao, Y., Kang, R., Dong, Z., Zhu, X., Wang, C., Guo, D. (2018). Model for surface topography prediction in mirror-milling of aircraft skin parts. *International Journal of Advanced Manufacturing Technology*, vol. 95, p. 2259-2268, **DOI:10.1007/s00170-017-1368-9**.

[8] Fei, J., Lin, B., Xiao, J., Ding, M., Yan, S., Zhang, X., Zhang, J. (2018). Investigation of moving fixture on deformation suppression during milling process of thin-walled structures. *Journal of Manufacturing Processes*, vol. 32, p. 403-411, **DOI:10.1016/j.jmapro.2018.03.011**.

[9] Bao, Y., Dong, Z.G., Kang, R.K., Li, Z., Yuan, Y.C. (2016). Milling force and machining deformation in mirror milling of aircraft skin. *Advanced Materials Research*, vol. 1136, p. 149-155. **DOI:10.4028/www.scientific.net/amr.1136.149**.

[10] Sallese, L., Grossi, N., Tsahalis, J., Scippa, A., Campatelli, G. (2016). Intelligent fixtures for active chatter control in milling. *Procedia CIRP*, vol. 55, p. 176-181, **DOI:10.1016/j.procir.2016.08.019**.

[11] Junbai, L., Kai, Z. (2011). Multi-point location theory, method, and application for flexible tooling system in aircraft manufacturing. *International Journal of Advanced Manufacturing Technology*, vol. 54, p. 729-736, **DOI:10.1007/s00170-010-2974-y**.

[12] Amaral, N., Rencis, J., Rong, Y. (2005). Development of a finite element analysis tool for fixture design integrity verification and optimisation. *International Journal of Advanced Manufacturing Technology*, vol. 25, p. 409-419, **DOI:10.1007/s00170-003-1796-6**.

[13] Shi, J., Gao, J., Song, Q., Liu, Z., Wan, Y. (2017). Dynamic deformation of thin-walled plate with variable thickness under moving milling force. *Procedia CIRP*, vol. 58, p. 311-316, **DOI:10.1016/j.procir.2017.03.329**.

[14] Chang, C.K., Lu, H.S. (2006). Study on the prediction model of surface roughness for side milling operations. *The*

International Journal of Advanced Manufacturing Technology, vol. 29, p. 867-878, **DOI:10.1007/s00170-005-2604-2**.

[15] Yuan, H., Wan, M., Yang, Y., Zhang, W. H. (2021). Mitigation of chatter in thin-wall milling by using double-side support device. *International Journal of Advanced Manufacturing Technology*, vol. 115, p. 213-232, **DOI:10.1007/s00170-021-06929-3**.

[16] Xiao, M., Shen, X., Ma, Y., Yang, F., Gao, N., Wei, W., Wu, D. (2018). Prediction of surface roughness and optimization of cutting parameters of stainless steel turning based on RSM. *Mathematical Problems in Engineering*, vol. 2018, art. ID 9051084, **DOI:10.1155/2018/9051084**.

[17] Yuan, H., Wan, M., Yang, Y., Zhang, W.H. (2021). Mitigation of chatter in thin-wall milling by using double-side support device. *International Journal of Advanced Manufacturing Technology*, vol. 115, p. 213-232, **DOI:10.1007/s00170-021-06929-3**.

[18] Zhao, Z., Wang, S., Wang, Z., Liu, N., Wang, S., Ma, C., Yang, B. (2019). Interference- and chatter-free cutter posture optimization towards minimal surface roughness in five-axis machining. *International Journal of Mechanical Sciences*, vol. 171, art. ID 105395, **DOI:10.1016/j.ijmecsci.2019.105395**.

[19] Maiyar, L.M., Ramanujan, R., Venkatesan, K., Jerald, J. (2013). Optimization of machining parameters for end milling of Inconel 718 super alloy using Taguchi based grey relational analysis. *Procedia Engineering*, vol. 64, p. 1276-1282, **DOI:10.1016/j.proeng.2013.09.208**.

[20] Jing, X., Lv, R., Chen, Y., Tian, Y., Li, H. (2020). Modelling and experimental analysis of the effects of run out, minimum chip thickness and elastic recovery on the cutting force in micro-end-milling. *International Journal of Mechanical Sciences*, vol. 176, art. ID 105540, **DOI:10.1016/j.ijmecsci.2020.105540**.

[21] Natarajan, M.M., Chinnasamy, B., Alphonse, B.H.B. (2022). Deform 3D simulation and experimental investigation of fixtures with support heads. *Mechanika*, vol. 28, no. 2. p. 130-138, DOI:10.**5755/j02.mech.29468**.

[22] Shaik, J.H., Srinivas, J. (2017). Optimal selection of operating parameters in end milling of Al-6061 work materials using multi-objective approach. *Mechanics of Advanced Materials and Modern Processes*, vol. 3, no. 5, **DOI:10.1186/s40759-017-0020-6**.

[23] Wanner, B., Eynian, M., Beno, T., Pejryd, L. (2012). Process stability strategies in milling of thin-walled Inconel 718. *AIP Conference Proceedings*, vol. 1431, p. 465-472, **DOI:10.1063/1.4707597**.

[24] Wu, T.Y., Lei, K.W. (2019). Prediction of surface roughness in milling process using vibration signal analysis and artificial neural network. *International Journal of Advanced Manufacturing Technology*, vol. 102, p. 305-314, DOI:10.1007/s00170-018-3176-2.

[25] Yue, C., Gao, H., Liu, X., Liang, S.Y., Wang, L. (2019). A review of chatter vibration research in milling. *Chinese Journal of Aeronautics*, vol. 32, no. 2, p. 215-242, **DOI:10.1016/j.cja.2018.11.007**.

[26] Alauddin, A., Baradie, M.A.EI, Hashimi, M.S.J. (1995). Computer aided analysis of a surface roughness model for end milling. *Journal of Material Production Technology*, vol. 55, no. 2, p. 123-127, **DOI:10.1016/0924-0136(95)01795-X**.

Strojniški vestnik - Journal of Mechanical Engineering 68(2022)12, 757-770
DOI:10.5545/sv-jme.2022.368
Original Scientific Paper
Received for review: 2022-09-15
Received revised form: 2022-11-17
Accepted for publication: 2022-12-16

Design, Manufacturing, and Thermodynamic Analysis of a Gamma-type Stirling Engine Powered by Solar Energy

Tolga Topgül*
Gazi University, Department of Automotive Engineering, Turkey

In this study first a double-cylinder V-type air compressor has been converted to a gamma-type Stirling engine. Some components of the compressor have been used in the converted engine. For this reason, the air compressor has determined some technical features of the Stirling engine. Other parts of the Stirling engine have been manufactured. Then, the optimum operating parameters to provide maximum thermal efficiency have been investigated using the nodal thermodynamic analysis considering that the engine is powered by solar energy. In the analysis, helium as the working fluid is used due to its suitable thermodynamic features and safety usage. The optimum working fluid mass and engine speed have been determined as 0.15 g and 100 rad/s for all hot-end temperatures (750 K, 800 K, and 850 K). Also, the optimum displacer height has been determined as 190 mm since there is no significant improvement in the thermal efficiency after this dimension. The maximum thermal efficiency has been obtained as 46.5 % at 100 rad/s and 850 K. At this point, the indicated power is determined as 657.8 W. If the engine speed increases from 100 rad/s to 300 rad/s, the indicated power becomes 1141.5 W. The experimental results indicate that the maximum output power with helium is 42.5 W at 4 bar charge pressure, 260 rpm engine speed, and 350 °C hot-end temperature. The engine output power could be further increased with some modifications such as higher hot-end temperature, reduction of heat losses and gas leakage.

Keywords: γ-type Stirling engine, operating parameters, engine performance, thermal efficiency, nodal analysis

Highlights

- *A double-cylinder V-type air compressor has been converted to a γ-type Stirling engine for use in solar energy applications.*
- *The structure of the air compressor has formed some parameters of the converted engine like phase angle, stroke, and cylinder diameter.*
- *The working fluid mass, engine speed, and displacer height have been optimized as operating parameters using the nodal thermodynamic analysis to obtain maximum thermal efficiency.*
- *According to the simulation results, the maximum thermal efficiency is 46.5 % and the maximum indicated power is 1141.5 W.*
- *The simulation results show that the thermal efficiency can be increased by optimizing the operating parameters.*
- *The experimental results indicate that the maximum output power with helium is 42.5 W at 4 bar charge pressure, 260 rpm engine speed, and 350 °C hot-end temperature.*

0 INTRODUCTION

Stirling engines are external combustion engines. This feature eliminates the possible dependency of the engine on a specific energy resource and allows it to work with diverse energy sources, especially solar and other renewable energy sources. Also, Stirling engines could be built in different configurations that have a significant effect on the engine performance. With these aspects, Stirling engines have attracted the attention of researchers. In the Stirling engine studies, besides conventional energy sources, researchers around the world **[1]** to **[5]** consider environmentally friendly energy sources, such as biomass, solar energy, and waste heat. Also, there are many studies **[6]** to **[9]** on the configurations, driving mechanisms, and structural properties of the Stirling engines.

Air, helium, and hydrogen are usually used as the working fluid in the Stirling engines. Among the working fluids, helium and hydrogen come forward with their high heat transfer ability, which is important for regenerative effectiveness, efficiency, and power. In fact, hydrogen can provide higher engine power than helium and other fluids; however, it has the risk of inflammation. For this reason, helium can be considered more advantageous **[10]** to **[14]**.

The operating parameters and physical structure of the Stirling engine have a significant effect on its efficiency and performance. The effects of the operating parameters, drive mechanisms, and configurations of the Stirling engines on their performances can be seen in several studies in the literature. Cheng and Yang **[15]** performed a theoretical analysis on the performance of the kinematic types (α, β, and γ) of the Stirling engine. It was emphasized that the γ-type engine could operate at low-temperature differences compared to other kinematic Stirling engines, but it needed very effective mechanisms to provide sufficient output work.

Abuelyamen and Ben-Mansour **[7]** compared numerically three basic types of kinematic Stirling engines in terms of thermal efficiency and output

*Corr. Author's Address: Gazi University, Faculty of Technology, Department of Automotive Engineeering, Ankara, Turkey, topgul@gazi.edu.tr

power. Their results showed that the highest thermal efficiency and output power were obtained with the γ-type engine as 9.8 % and 9.223 W, respectively. Also, the α-type engine had the lowest performance. Nevertheless, its performance was improved from 1.8 % and 0.908 W to 10.5 % and 9.856 W owing to the modification to have an annular connecting pipe instead of the circular pipe.

Laazaar and Boutammachte **[2]** investigated the suitable energy source for each Stirling engine type. For this purpose, they used the same physical and geometrical parameters in several kinematic types of Stirling engines by using a crank drive mechanism. They emphasized that each type of Stirling engine was more suitable for a particular energy to obtain high performance. The results of the study showed that the α-type engine was more applicable to waste heat recovery in the industrial sector owing to the high gas temperature, and the β and γ-type engines were more suitable for low and medium temperature differences like biomass and solar energy.

Topgül et al. **[16]** experimentally investigated the effect of the connection type (cold-end and hot-end) between the expansion and displacer cylinders on the output power and torque of a γ-type Stirling engine. It was observed that the engine performance improves with the hot-end connection compared with the cold-end connection at 30 °C cold and 200 °C hot source temperatures. The results showed that the maximum output power and engine torque for the hot-end connection were higher by 84.7 % and 68.4 % than those of the cold-end connection, respectively.

Kongtragool and Wongwises **[17]** emphasized the importance of dead volume and regenerator effectiveness. The results of the numerical simulation showed that decreasing regenerator effectiveness and increasing dead volume decrease the engine efficiency.

Cheng and Yu **[13]** researched the effect of the physical and geometric parameters on the thermal efficiency and performance of the β-type rhombic drive Stirling engine. For this purpose, the heat source temperature, offset distance between the crank and the center of the gear, regenerative gap, and distance between two gears were discussed in their parametric study. The results of the study showed that engine output power and efficiency could be improved by adjusting these parameters.

Ahmed et al. **[18]** performed the optimal design of a free piston β-type Stirling engine using a numerical model. According to the optimization results, about 7.95 kW engine power and 30 % thermal efficiency were obtained.

In a numerical study, Raghavendra et al. **[19]** investigated the effects of the operating and geometric parameters on the performance of a β-type Stirling engine. They expressed that as the displacer height was increased, both engine power and efficiency increased due to an increase in the compression ratio. The effects of the regenerator channel gap and offset distance from the crank to the center on the power and efficiency were similar. The results of the study indicated that the maximum engine power was 27.4 W at 1700 rpm and 800 °C.

Ahmed et al. **[20]** investigated the effects of the operating and geometric parameters on the performance of a β-type Stirling engine using a numerical model. The phase angle, temperature ratio, regenerator porosity, mean pressure, and frequency were optimized. The optimum value of the phase angle was found to be between 80° to 100° with regard to the engine efficiency and power. It was emphasized that the engine power decreased with the increasing temperature ratio and it decreased dramatically after the approximately 0.32 temperature ratio. They stated that the value of the frequency below 30 Hz was suitable for effective and efficient engine operation.

Aksoy et al. **[21]** experimentally investigated the performance of a β-type Stirling engine powered by solar energy. In the study, 400 W and 1000 W halogen lamps placed on the upper side of the displacer cylinder were used as the solar simulators. They obtained the hot-end temperatures as 623 K and 873 K for 400 W and 1000 W halogen lamps, respectively. They found that the maximum torque, power, and thermal efficiency with a 1000 W halogen lamp were 3.4 Nm, 127.17 W, and 12.85 %, respectively.

In a review study, Malik et al. **[11]** evaluated the applications and design parameters of the parabolic solar dish Stirling systems. They stated that a temperature level of 500 °C could be achieved with a parabolic trough collector, and 600 °C could be obtained using a parabolic solar dish collector. Additionally, they expressed that although the solar power tower had a higher temperature level (1000 °C), the parabolic solar dish systems would gain importance because of some disadvantages of the solar power tower. These disadvantages were mentioned by Cavallaro et al. **[22]** as higher greenhouse gas emissions (GHG/kWh), land use, and water usage. In another study, Sharma **[23]** emphasized that it could be achieved up to 600 °C using a parabolic trough or parabolic dish collectors in solar application systems. It was also expressed that the central tower was the most suitable solar power system for upper temperatures (more than 1000 °C).

In the present study, an air compressor that was produced for a different purpose was converted to an external combustion engine powered by eco-friendly energy sources. In the preliminary tests using LPG fueled heater, it was seen that the converted γ-type Stirling engine started to operate at low temperatures of approximately 100 °C using atmospheric air. This is promising for solar energy applications. The development of the engine and solar energy system has been proceeding. This study presents the manufacturing procedure and results of the thermodynamic analysis. Additionally, the pre-test results with air and helium are presented in this study and the experimental results are also compared to that of the nodal thermodynamic analysis.

1 MATERIAL AND METHODS

In this study, design, manufacturing, and nodal-thermodynamic analyses of a γ-type Stirling engine that can be used in solar energy applications were conducted. In terms of easiness of manufacturing, a V-type air compressor was converted to a γ-type Stirling engine by using the block, cylinders, connecting rods, and the crank mechanism of the compressor. In the theoretical analysis, the operating parameters were investigated for the designed and manufactured Stirling engine. In the analysis, the phase angle was used as 90° due to the structure of the V-type air compressor. This value is also suitable for Stirling engine applications in the literature [20]. In the numerical calculations, 750 K, 800 K, and 850 K hot-end temperatures were used considering the temperature range of the parabolic collector systems [11] and [23].

The system given as a schematic view in Fig. 1 could be considered for supplying solar power to the converted Stirling engine.

This application can be seen in some studies in the literature [11], [24] to [26]. It can be provided up to 600 °C (873 K) hot source temperature using the parabolic solar dish system as in Fig. 1 considering the literature [11] and [23]. This system using solar energy, an unlimited energy source can be defined as an eco-friendly power plant because of reducing the carbon footprint. Also, this system could be used to produce electricity [27] and [28].

1.1 Description of the Converted Stirling Engine

A γ-type Stirling engine was designed for solar energy applications. The photographs of the γ-type Stirling engine converted from a V-type air compressor are seen in Figs. 2 and 3.

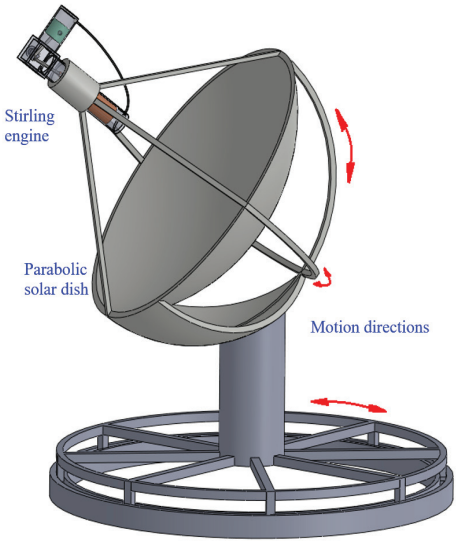

Fig. 1. *The schematic view of the converted Stirling engine powered by solar energy*

Fig. 2. *The assembly photograph of the Stirling engine*

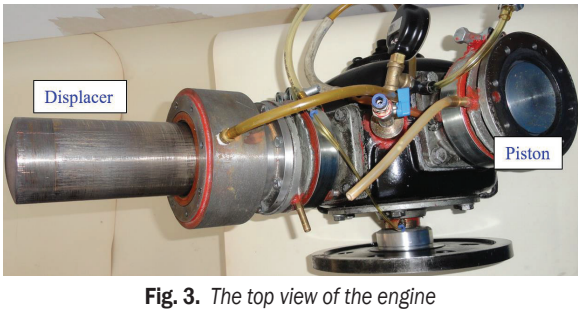

Fig. 3. *The top view of the engine*

The air compressor's block, cylinders, connecting rods, and crank mechanism were used in the converted

Stirling engine seen in Figs. 2 and 3. Since the compressor had double cylinders, one of the cylinders formed the expansion cylinder which is also called the power cylinder, and the other formed the displacer cylinder. However, a new piston and cylinder head were required for the expansion cylinder. A new piston having the same diameter was manufactured from aluminum alloy. The material of the cylinder head was ASTM steel.

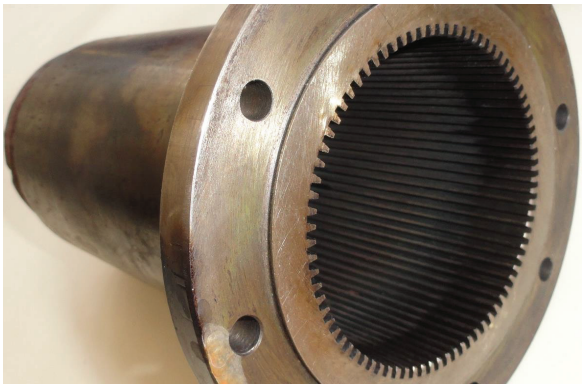

Fig. 4. *The inner surface of the displacer cylinder*

To form the displacer cylinder, additional parts were manufactured. For this purpose, a displacer cylinder, a displacer, and a displacer rod were manufactured. The displacer and its cylinder were manufactured from ASTM steel and the cylinder's inner surface was enlarged with rectangular slots (see Fig. 4). The displacer cylinder was placed on the compressor cylinder using bolts. The connecting rods of the piston and displacer were connected to the same crankpin journal. The strokes of the piston and displacer and the angle between the cylinders were not changed because the air compressor's block and crank mechanism were used. For this reason, the phase angle between the cylinders was obtained as 90°. The expansion and displacer cylinders were combined via a hot-end connection. The advantages of the hot-end connection in the Stirling engines were previously presented by Topgül et al. [16] and Kentfield [29].

1.2 Principal of the Operation of the Converted Stirling Engine

P-V (pressure-volume) and T-s (temperature-entropy) diagrams and the positions of the converted γ-type Stirling engine during the cycle are given in Fig. 5. As shown in the figure, the engine turns anticlockwise. During the 1-2 process in which the crankshaft moves from –45° to 45° crankshaft angle (CA), the piston in the expansion cylinder goes from the top dead center (TDC) to the bottom dead center (BDC), the working fluid expands isothermally, and the piston produces work. The displacer is almost constant around the BDC.

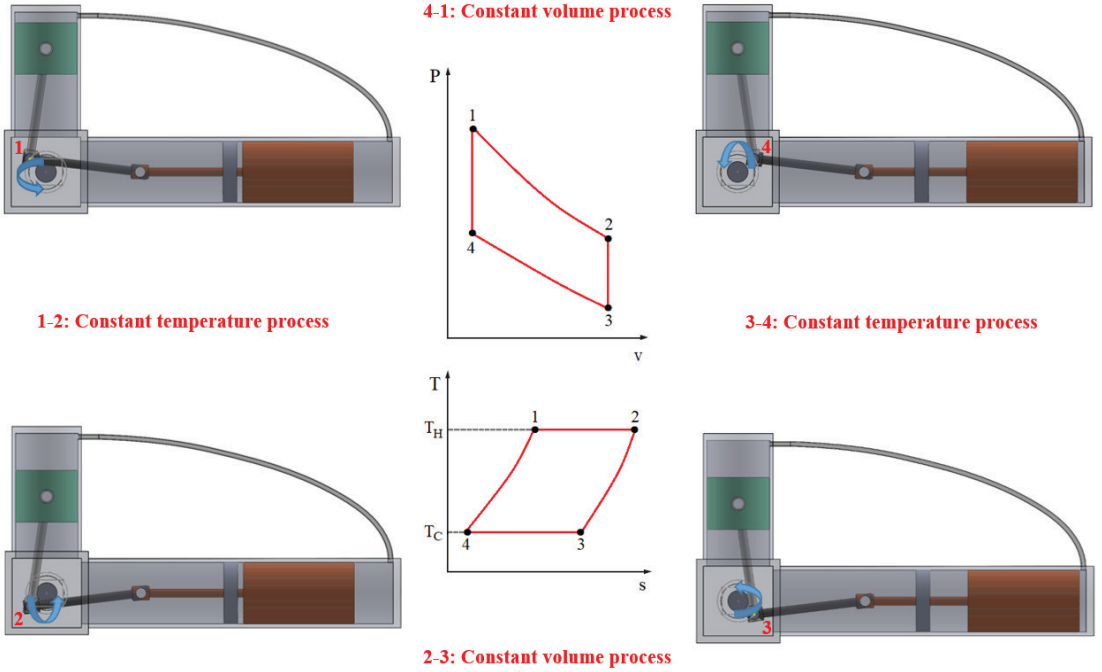

Fig. 5. *P-V and T-s diagrams and the positions of the converted γ-type Stirling engine during the cycle*

During the 2-3 process in which the crankshaft moves from 45° to 135° CA, the piston is almost constant around the BDC. The displacer goes from the BDC to the TDC, the working fluid passes through the heating–cooling channel between the cylinder wall and displacer from the hot volume to the cold volume. The hot volume decreases while the cold volume increases, because of this, the total volume does not change. At this constant volume process, the working fluid is cooled.

During the 3-4 process in which the crankshaft moves from 135° to 225° CA, the piston goes from the BDC to the TDC and the working fluid is compressed isothermally. During this process, the position of the displacer is almost near the TDC.

Finally, during the 4-1 process in which the crankshaft moves from 225° to 315° CA, the position of the piston is almost near the TDC. The displacer goes from the TDC to the BDC, the working fluid passes through the heating–cooling channel between the cylinder wall and displacer from the cold volume to the hot volume. The total volume does not change since the cold volume decreases while the hot volume increases. The working fluid is heated during this constant volume process. At the end of this process, the cycle is completed.

The variations in the volumes during the cycle are given in Fig. 6. As demonstrated in the figure, the phase angle between the expansion and displacer cylinders is 90°. Also, the total volume is the sum of the cold, hot, and expansion volumes.

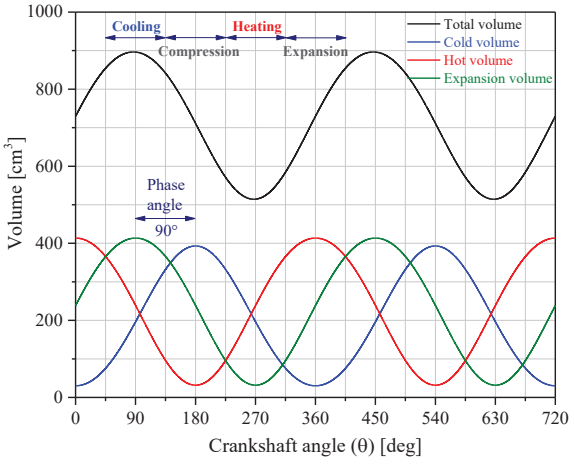

Fig. 6. *The variations in the volumes with respect to the crankshaft angle*

1.3 Mathematical Model

In the analysis, helium was chosen as the working fluid due to its suitable thermodynamic features and safety usage. In the literature, Cinar et al. [30] suggested in their experimental study to use as possible as high hot source temperatures and helium or hydrogen as the working fluid to improve engine performance. In a theoretical study, Chahartaghi and Sheykhi [31] expressed that the maximum engine power for helium was 5151 W at 1500 rpm and that of hydrogen was 12679 W at 3000 rpm. They stated that this was due to the viscosity of hydrogen being lower than that of helium. Also, it was emphasized that the higher specific heat value of hydrogen than that of helium affects the difference between the working fluid temperature and the wall temperatures. Ben-Mansour et al. [32] used air, helium, and hydrogen as working fluids. Hydrogen, which is among the working fluids used, possesses the highest thermal conductivity, while air has the lowest. They stated that this feature affects heat transfer and absorption amount of heat. Shufat et al. [28] and Cheng et al. [33] reported that engine power is much higher when using helium as a working fluid compared to air. Ahmet et al. [18] proposed helium as the working fluid for Stirling engines since hydrogen has a low molar mass, reactive nature, and inflammatory properties.

In this study, the nodal analysis method was used for thermodynamic analysis. The simulation study was conducted on the γ-type Stirling engine considering similar studies in the literature [34] to [40]. The specifications of the engine and the simulation inputs are shown in Table 1.

The assumptions in the analysis were considered as follows:

1. The working fluid is an ideal gas.
2. There is no leakage, so the total mass of fluid in the total volume does not vary.
3. There are no pressure drops. The pressure of the working fluid in all of the nodal volumes is equal.
4. There is no heat transfer from the engine to the ambient.
5. There is no mechanical loss.
6. The rotational speed of the crankshaft does not vary for each thermodynamic solution.
7. The wall temperatures of the nodal volumes are constant and foreknown, as shown in Fig 7.
8. During the regeneration, the variation of the wall temperature between cold-end and hot-end temperatures is linear and does not change with time.

Table 1. *The simulation inputs and the specifications of the converted γ-type Stirling engine*

Working fluid	*He*	Helium
Gas constant of helium [J/(kgK)]	$\Re$	2077
The specific heat at constant pressure [J/(kgK)])	c_p	5192.6
The specific heat at constant volume [J/(kgK)]	c_v	3115.6
Compression ratio		1.74
Diplacer diameter [mm]	D_d	88.5
Piston diameter [mm]	D_p	90
Diplacer rod diameter [mm]	D_{dr}	20
Convective heat transfer coefficient in the cooler, regenerator, and heater [W/(m²K)]	h	1200
Convective heat transfer coefficient in the cylinders [W/(m²K)]	h_c	70
Displacer height [mm]	h_d	190
Distance between piston pin center and piston top [mm]	h_p	38
Engine speed [rad/s]	ω_e	100
Crank radius [mm]	R_c	30
Displacer rod length [mm]	R_{dr}	167.3
Connecting rod length [mm]	R_{cr}	180
Hot-end temperature [K]	T_H	750 800 850
Cold-end temperature [K]	T_C	350
Distance between the crankpin center and displacer cylinder bottom [mm]	Z_c	312.3
Distance between the crankpin center and expansion cylinder top [mm]	Z_e	253
Distance between the crankpin center and displacer cylinder top [mm]	Z_h	572.3

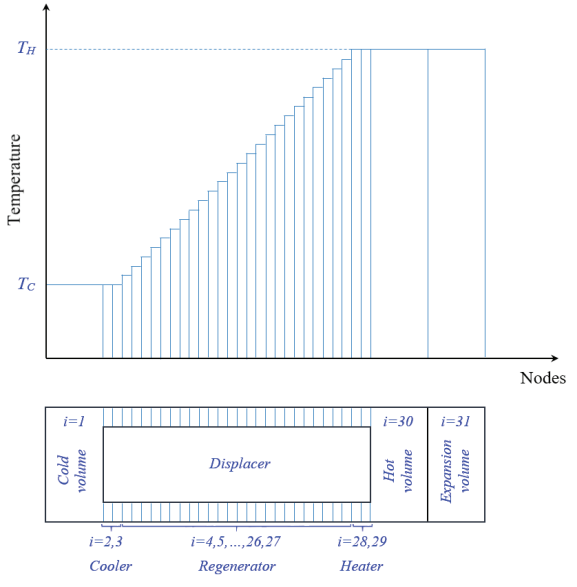

Fig. 7. *The nodal volumes and wall temperature distribution*

The working fluid in the Stirling engine continuously moves between the expansion and displacer cylinders during the cycle. In other words, the working fluid passes through the cold volume, cooler, regenerator, heater, hot volume, and expansion volume. In the calculations, the total volume was divided into 31 nodal volumes. Fig. 7 depicts all nodal volumes used in the simulation and the boundary temperatures of the nodal volumes. The first nodal volume is the cold volume of the displacer cylinder and is indicated by $i = 1$. The cooler, regenerator, and heater volumes in the heating–cooling channel between the cylinder wall and displacer are indicated by $i = 2, 3$, $i = 4, 5, \ldots, 27$, and $i = 28, 29$, respectively. The hot volume of the displacer cylinder is indicated by $i = 30$. The last of the nodal volumes, $i = 31$, is the expansion volume.

A schematic figure of the converted engine is indicated in Fig. 8. As indicated in Fig. 8, β_d specifies the angle between the axis of the displacer cylinder and the axis of the connecting rod of the displacer. β_d can be defined with respect to the crankshaft angle (θ).

$$\beta_d = arcsin\left(\frac{R_c}{R_{cr}} sin\theta\right), \tag{1}$$

where β_p specifies the angle between the axis of the expansion cylinder and the axis of the connecting rod of the piston (Fig. 8). β_p can be defined with respect to θ.

$$\beta_p = arcsin\left(\frac{R_c}{R_{cr}} cos\theta\right). \tag{2}$$

The cold, hot, and expansion volumes can be obtained using Eqs. (3) to (5), respectively.

$$V_1 = \left(-R_c\, cos\theta + R_{cr}\, cos\,\beta_d + R_{dr} - Z_c\right)\cdot\left(A_p - A_{dr}\right), \tag{3}$$

$$V_{30} = \left(Z_h - \left(-R_c\, cos\theta + R_{cr}\, cos\,\beta_d + R_{dr} + h_d\right)\right)\cdot A_p, \tag{4}$$

$$V_{31} = \left(Z_e - \left(-R_c\, sin\theta + R_{cr}\, cos\,\beta_p + h_p\right)\right)\cdot A_p. \tag{5}$$

The pressure can be determined using the Schmidt formula (Eq. (6)).

$$p = \frac{m\Re}{\sum_{i=1}^{31}\frac{V_i}{T_i}}. \tag{6}$$

The working fluid temperature in a nodal volume can be calculated via Eq. (7).

$$T = T^F + \Delta T. \tag{7}$$

In Eq. (7), the T^F indicates the working fluid temperature within the time step before the current one. ΔT, the temperature variation in the nodal volume

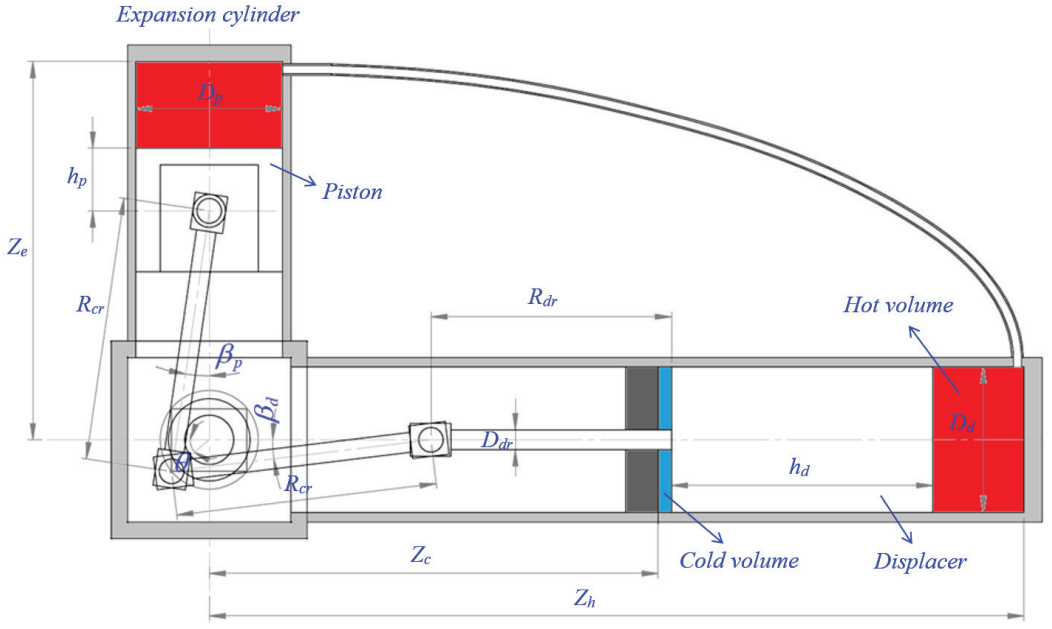

Fig. 8. *The schematic figure of the converted γ-type Stirling engine*

within the time step, can be defined via the first law of thermodynamics (Eq. (8)).

$$\Delta Q - \Delta W = H_o - H_i + (\Delta U), \tag{8}$$

where ΔQ is the heat exchange between the working fluid and the nodal volume, ΔW is the work generated in the nodal volume, ΔU is the variation of the internal energy in the nodal volume, H_o is the enthalpy of the outgoing working fluid from the nodal volume, and H_i is the enthalpy of the entering working fluid into the nodal volume.

1.4 Results of the Pre-Test and Comparison with Nodal Thermodynamic Analysis Results

The converted Stirling engine is tested in an experimental setup as seen in Fig. 9. In the experiments, the hot-end temperature was set at 350 ±5 °C by using an LPG-fueled heater. The cold-end temperature was adjusted to 35 ±2 °C by circulating the cooling water into the water jacket. All temperatures were measured NiCr-Ni thermocouples and a 12-channel Elimko 6000 brand device. The working fluid pressure was measured with a burdon tube manometer. To impose variable loading conditions on the engine used a prony-type dynamometer. The ESIT BB20 brand load cell was also used to determine brake torque. Finally, the measurement of the engine speed was performed via ENDA ETS1410 digital tachometer.

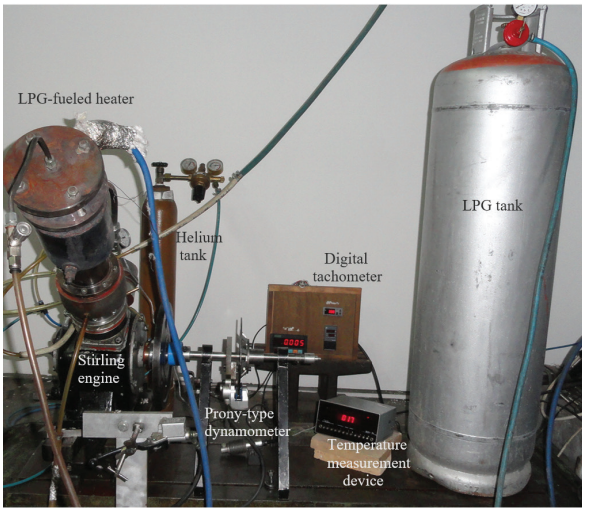

Fig. 9. *The photograph of the experimental setup*

Table 2. *The accuracies of the measurement equipment and the uncertainty of the calculated value*

Measured values	Accuracy
Temperature	±1 °C
Gauge pressure	±0.1 bar
Torque	±0.003 Nm
Speed	±1 rpm
Calculated value	Uncertainty
Engine output power	0.4 % to 2.85 %

It can be seen in Table 2, the accuracies of the measurement equipment and the uncertainty of the

calculated parameter. Similar to the experimental studies in the literature [16], [41] to [44], the route mean square method was used for uncertainty analysis. Additionally, the error bars based on the accuracies of the measurement equipment and the maximum uncertainty are used in Fig. 10 similar to the literature [16] and [45]. Some of the error bars may not be noticed due to their small values or scale.

Fig. 10 shows the comparison of the engine output power obtained with air and helium at different charge pressures. The charge pressure is given as the absolute pressure in this figure. Compared to the air, helium had a higher improvement in the engine power for all charge pressures. While the maximum engine power with air was obtained as 9.8 W at 123 rpm engine speed and 3 bar charge pressure, helium provided significantly higher power at higher engine speed and charge pressure (42.5 W at 260 rpm and 4 bar). This result agrees with the literature [28], [30], [32], and [33]. However, the output power decreased when the charge pressure was increased more for both working fluids.

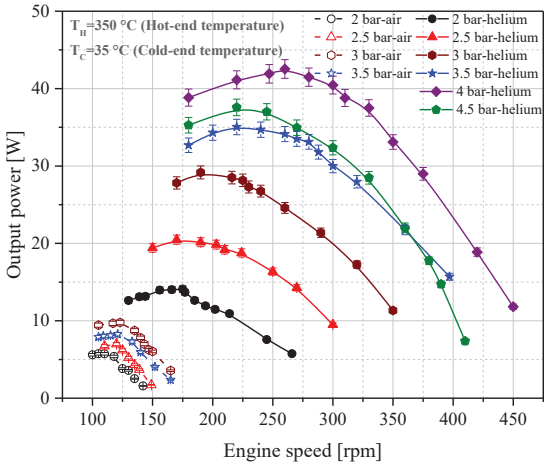

Fig. 10. *The variation of the engine output power at different charge pressures with air and helium*

Fig. 11a depicts a comparison of the experimental and theoretical analysis results for helium at the charge pressures of 2.5 bar and 4 bar. While the experimental results expressed the engine output power, the results of the nodal thermodynamic analysis stated the indicated engine power in ideal operating conditions such as using ideal gas, no leakage, no pressure drops, etc. The assumptions in the analysis are given in Section 1.3.

The maximum output power values were found as 20.5 W and 42.5 W at 2.5 bar and 4 bar charge pressure, respectively. At the points corresponding to these values, the values of the indicated power were determined as 77.1 W and 188.9 W, respectively. The differences in these values result from comparison with the indicated power and effective power (engine output power). The friction may also have some influence on this difference. Since the friction depends on the engine speed, higher difference appears at high speeds. In the theoretical analysis, the factor limiting the power is the engine speed which shortens the time required for adequate heat transfer. For this reason, the maximum indicated power could be obtained at a higher engine speed. However, this engine speed was not reached in the pre-tests. For all these reasons, as seen in Fig. 11a, the difference between theoretical and experimental results increases with the increase in the engine speed. Fig. 11b shows the extended scale of the engine speed. Theoretically, as illustrated in this figure, the maximum indicated power is obtained as 573 W at 2.5 bar charge pressure and 2387 rpm engine speed, while it is 571.5 W at 4 bar and 1432 rpm.

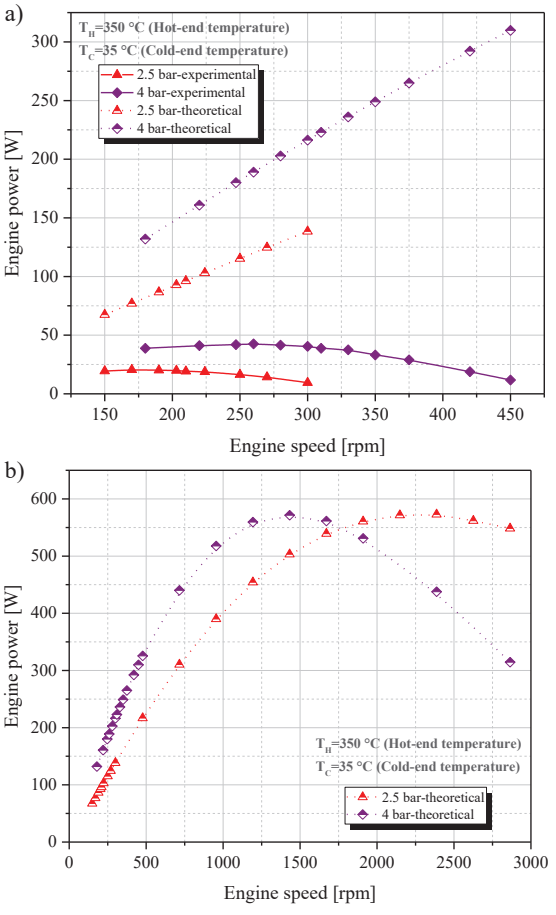

Fig. 11. *a) The comparison with experimental and theoretical results; and b) the variation of the theoretical results versus engine speed*

The results of the theoretical analysis show the highest achievable engine power. In other words, it shows the upper limit of engine performance under the considered operating conditions. In practice, this limit can be reached as the engine and operating conditions become perfect. Some improvements can be performed by reducing heat losses, friction losses, and pressure losses, or increasing regeneration effectiveness and providing sealing. To obtain more power, the Stirling engine should be operated at a higher engine speed with the best regenerator effectiveness.

2 RESULTS AND DISCUSSION

The phase angle, cylinder diameter, stroke, displacer height, engine speed, hot source temperature, cold source temperature, etc. are some operating and structural parameters in a Stirling engine. These parameters, which have a significant impact on engine performance, need to be evaluated according to the configuration of the Stirling engine. The γ-type Stirling engine was converted from a V-type air compressor and optimized to operate with the highest efficiency in solar energy applications. For this reason, this study aimed to maximize the thermal efficiency by optimizing the hot-end temperature, the mass of the working fluid, engine speed, and displacer height. In the analysis, the hot-end temperature range was determined considering parabolic collector systems.

2.1 The Effect of Working Fluid Mass

The effect of the working fluid mass and hot-end temperature on the engine efficiency and power is given in Fig. 12. These simulation results are compatible with the literature [18], [34], [35], [46], and [47].

As indicated in the figure, the highest engine power and thermal efficiency are obtained at 850 K hot-end temperature. Compared with their maximum values at 750 K, the thermal efficiency and the engine power at 850 K were improved by 14 % and 44 %, respectively. Considering the effect of the working fluid mass, it can be seen that the thermal efficiency increases up to its maximum value at 0.15 g for all hot-end temperatures as the mass increases. The low mass value means that the amount of the working fluid in the circulation is low. For the heating-cooling process, it is needed that enough working fluid circulates between cold and hot volumes. For this reason, the thermal efficiency at the lower mass of the working fluid was relatively low compared to that of 0.15 g. Also, charge pressure which figures the cyclic average pressure is lower due to the low mass of working fluid. As illustrated in Fig. 13, charge pressure which expresses the produced amount of the indicated work increases depending on the mass of the working fluid. For maximum thermal efficiency, the optimum working fluid mass was determined as 0.15 g. With the increase in the mass of the working fluid above this value, the thermal efficiency decreased due to inadequate heat transfer to the working fluid. It means that the capacities of the heating-cooling processes are inadequate for working fluid mass. In this study, an external heater-cooler and a regenerator were not used. It was assumed that the heat transfer occurs from the surfaces of the cylinders. For this purpose, the inner surface of the displacer cylinder was enlarged with rectangular slots. It can be used as an external heat exchanger to increase heat transfer.

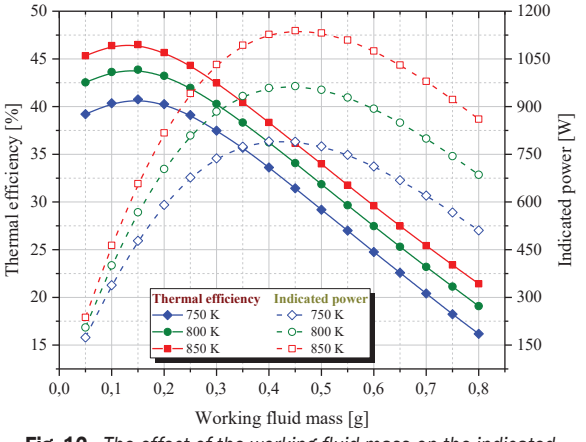

Fig. 12. *The effect of the working fluid mass on the indicated power and thermal efficiency*

The engine power showed a similar inclination with the thermal efficiency, but its maximum value was obtained at about 0.45 g mass of working fluid. The power depends on the work per cycle. For this reason, the power increased as the work increased. The area shown in the pressure-volume (P-V) diagram indicates the work of the cycle (see Fig. 13). As shown in the figure, the indicated work at 0.45 g is higher than that of the 0.15 g mass of working fluid at all hot-end temperatures. However, as seen in the figure, the indicated work is close to the isothermal work at 0.15 g because of the higher thermal efficiency.

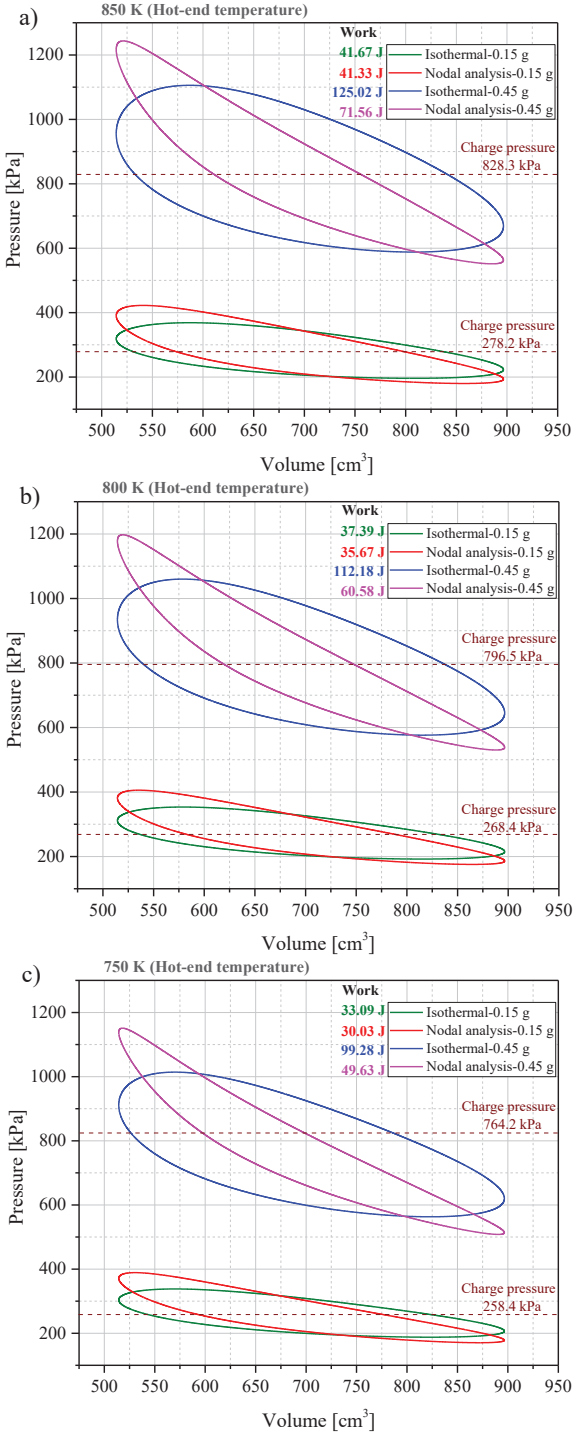

Fig. 13. *The effect of the working fluid mass on the P-V diagram at hot-end temperatures; a) 850 K, b) 800 K, and c) 750 K*

2.2 The Effect of Engine Speed

The effect of the engine speed on the indicated power and thermal efficiency is seen in Fig. 14. At low engine speeds, the thermal efficiency was relatively low. The reason for this may be inadequate working fluid mass in the circulation. Also, the indicated engine power was considerably low up to 300 rad/s engine speed due to the lower number of cycles. However, the efficiency and power increased up to their maximum values depending on increasing the engine speed. The thermal efficiency and indicated power began to decrease over 100 rad/s and 300 rad/s, respectively. The working fluid has less time at higher engine speeds to heat transfer. This causes insufficient temperature difference between heated and cooled working fluid and reduces indicated work and efficiency. In the literature, Ahmed et al. [18], Karabulut et al. [34], Xiao et al. [48], and Alfarawi et al. [49] obtained similar results.

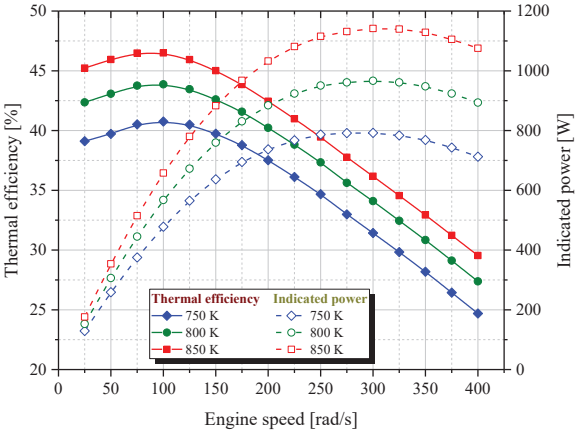

Fig. 14. *The effect of the engine speed on the indicated power and thermal efficiency*

The effect of the engine speed on the P-V diagram is given in Fig. 15. As indicated in the figure, the indicated work at 300 rad/s is less than that of the 100 rad/s. The duration of the cycle decreases due to the increase in the engine speed. Because of this, the heat transfer in the heating-cooling processes during the cycle period cannot occur sufficiently due to inadequate time.

When Figs. 14 and 15 are evaluated together, it can be realized that the indicated engine power increases when the engine speed increases from 100 rad/s to 300 rad/s although the work decreases. The power is identified as the work done per unit time (see Eq. (9)). For this reason, although the work done in each cycle decreases, it may increase depending on the number of cycles per second.

$$Power\,[\mathrm{W}] = \frac{Work\,[\mathrm{J}] \cdot Speed\,[\mathrm{rad/s}]}{2\pi}. \qquad (9)$$

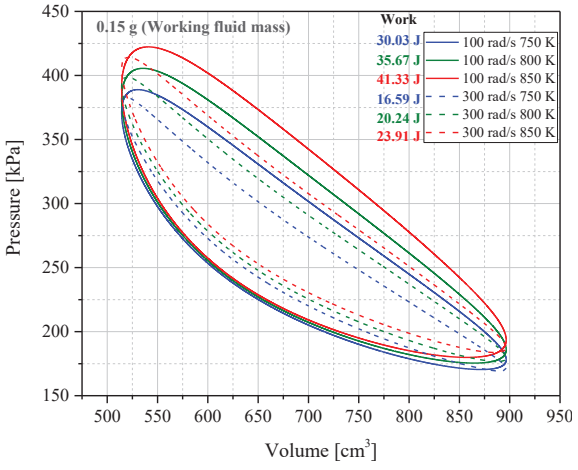

Fig. 15. *The effect of the engine speed and hot-end temperature on the P-V diagram*

2.3 The Effect of Displacer Height

Figs. 16 and 17 depict the effect of displacer height on the engine performance at different hot-end temperatures.

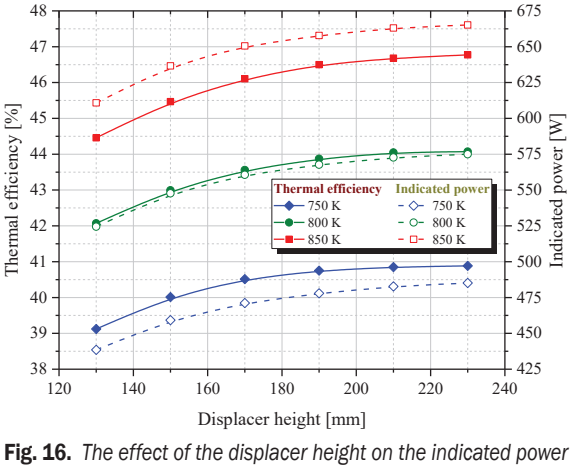

Fig. 16. *The effect of the displacer height on the indicated power and thermal efficiency*

As illustrated in Fig. 16, the increment in both the thermal efficiency and indicated power varies depending on the increase in the displacer height. An external regenerator was not used in this converted engine. Therefore, the regeneration process is provided by the working fluid passing through the heating–cooling channel between the cylinder wall and the displacer. Because of this, a higher displacer height provides a greater heat transfer area and improves power and efficiency. However, as demonstrated in the figure, the effect of this parameter becomes low as the height increases. In the literature, similar results were also obtained by Raghavendra et al. [19], Bataineh [37], and Eid [50].

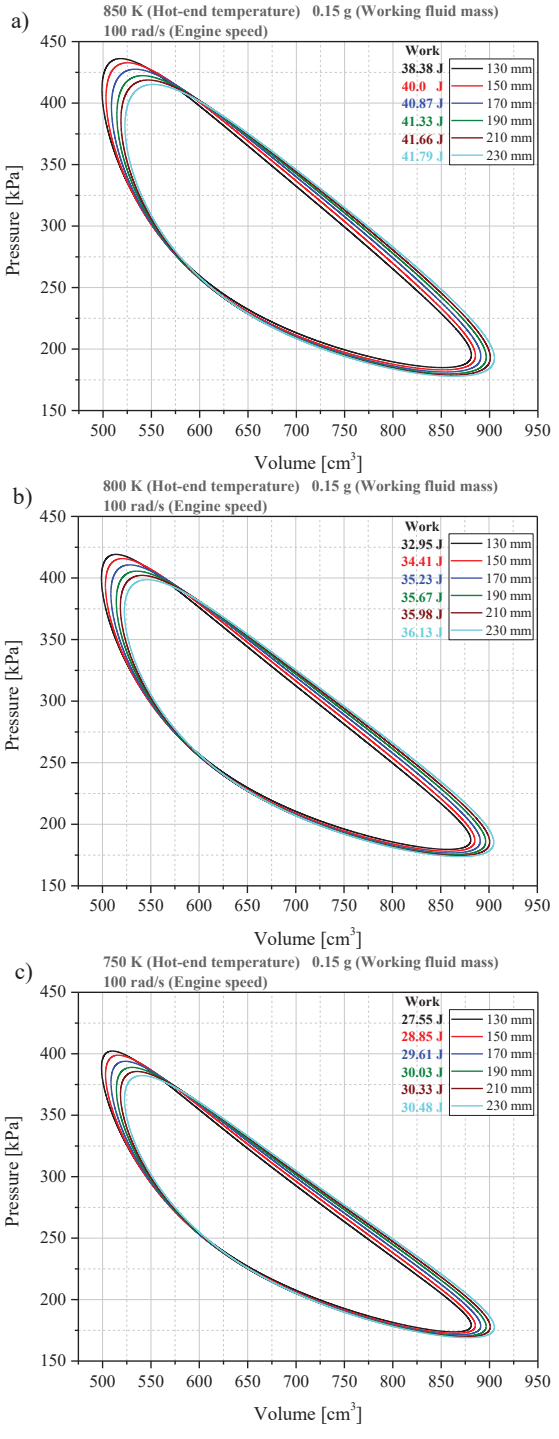

Fig. 17. *The effect of the displacer height on the P-V diagram at hot-end temperatures: a) 850 K, b) 800 K, and c) 750 K*

The variation of the indicated works depending on the displacer height for each hot-end temperature

is demonstrated in Fig. 17. It can be seen that the minimum and maximum values of the total volume increase based on displacer height. The swept volume remains constant since the crankshaft radius does not change. Only, the working fluid circulates between larger volumes because of the increasing displacer cylinder volume. The indicated work increases because of a greater heat transfer area. However, if the displacer height is increased more, the amount of improvement in the indicated work decreases. According to the literature **[17]**, **[18]**, **[37]**, and **[50]**, an increase in the dead volume has a negative effect on engine performance. Therefore, the volume of the regenerator should be large enough for good thermal capacity and engine output power.

If the results obtained for different displacer heights are compared with each other, it can be seen that when the displacer height increases from 130 mm to 190 mm, at 750 K, 800 K, and 850 K, the indicated work increases by 9 %, 8.25 %, and 7.7 %, respectively. However, when the size is increased from 190 mm to 230 mm, the increments are about 1.5 %, 1.3 %, and 1.1 %, respectively. Depending on the increase in the displacer height, the approaching of the indicated work to the isothermal work may also cause these results. The optimum displacer height was determined as 190 mm due to the decrease in the positive effect of the increase in the displacer height and the losses that would occur in the practical operation.

3 CONCLUSIONS

In this study, a double-cylinder V-type air compressor was converted to a γ-type Stirling engine. The block, cylinders, connecting rods, and crank mechanism of the air compressor constituted the main structure of the converted engine. However, a new piston, displacer, displacer cylinder, and other equipment were needed to form the converted engine. After this conversion, this study aimed to determine the optimum operating parameters of the Stirling engine for use in solar energy applications. For this purpose, the nodal thermodynamic analysis of the γ-type Stirling engine was conducted. Helium was considered as the working fluid due to its suitable thermodynamic properties and safety usage.

The optimum value of the working fluid mass and engine speed were determined as 0.15 g and 100 rad/s for all hot-end temperatures (750 K, 800 K, and 850 K). Also, the optimum displacer height was preferred as 190 mm since there was no significant improvement in the thermal efficiency for the longer dimensions. By using these optimum values, the maximum thermal efficiency was obtained as 46.5 % (at 0.15 g working fluid mass, 100 rad/s engine speed, 190 mm displacer height, and 850 K hot-end temperature). At this operating condition, the indicated power was obtained as 657.8 W. The maximum indicated power was found as 1141.5 W at 300 rad/s (other parameters remained the same), but the thermal efficiency decreased to 36.2 % under this operating condition. It can be concluded that the thermal efficiency can be increased by optimizing the operating parameters of the Stirling engine.

4 REFERENCES

[1] Ferreira, A.C., Silva, J., Teixeira, S., Teixeira, J.C., Nebra, S.A. (2020). Assessment of the Stirling engine performance comparing two renewable energy sources: Solar energy and biomass. *Renewable Energy*, vol. 154, p. 581-597, **DOI:10.1016/j.renene.2020.03.020**.

[2] Laazaar, K., Boutammachte, N. (2020). New approach of decision support method for Stirling engine type choice towards a better exploitation of renewable energies. *Energy Conversion and Management*, vol. 223, 113326, **DOI:10.1016/j.enconman.2020.113326**.

[3] Urciuolo, M., Chirone, R., Marra, F.S., Solimene, R. (2019). Power generation by Stirling engine during fluidized bed combustion of wood pellets. *Combustion Science and Technology*, vol. 191, no. 2, p. 263-274, **DOI:10.1080/00102202.2018.1453122**.

[4] Singh, U.R., Kumar, A. (2018). Review on solar Stirling engine: Development and performance. *Thermal Science and Engineering Progress*, vol. 8, p. 244-256, **DOI:10.1016/j.tsep.2018.08.016**.

[5] Stritih, U., Zupan, G., Butala, V. (2007). A parametrical analysis of a biomass Stirling cogeneration unit for use in housing. *Strojniški vestnik - Journal of Mechanical Engineering*, vol. 53, no. 9, p. 556-568.

[6] Karabulut, H., Okur, M., Cinar, C. (2022). Mechanical configuration and thermodynamic analysis of an alpha-type Stirling engine with crank-shifted driving mechanism. *Iranian Journal of Science and Technology, Transactions of Mechanical Engineering*, vol. 46, p. 431-448, **DOI:10.1007/s40997-021-00436-2**.

[7] Abuelyamen, A., Ben-Mansour, R. (2018). Energy efficiency comparison of Stirling engine types (α, β, and γ) using detailed CFD modeling. *International Journal of Thermal Sciences*, vol. 132, p. 411-423, **DOI:10.1016/j.ijthermalsci.2018.06.026**.

[8] Aksoy, F., Solmaz, H., Karabulut, H., Cinar, C., Ozgoren, Y.O., Polat, S. (2016). A thermodynamic approach to compare the performance of rhombic-drive and crank-drive mechanisms for a beta-type Stirling engine. *Applied Thermal Engineering*, vol. 93, p. 359-367, **DOI:10.1016/j.applthermaleng.2015.09.105**.

[9] Shendage, D.J., Kedare, S.B., Bapat, S.L. (2011). An analysis of beta type Stirling engine with rhombic drive mechanism. *Renewable Energy*, vol. 36, no. 1, p. 289-297, **DOI:10.1016/j.renene.2010.06.041**.

[10] Liu, M., Zhang, B., Zheng, K., Du, X., Wang, H. (2022). Numerical study on regenerative effectiveness of parallel-plate regenerator for Stirling engine. *International Journal of Green Energy*, vol. 19, no. 12, p. 1345-1356, **DOI:10.1080/15435075.2021.1997750**.

[11] Malik, M.Z., Shaikh, P.H., Zhang, S., Lashari, A.A., Leghari, Z.H., Baloch, M.H., Memon, Z.A., Caiming, C. (2022). A review on design parameters and specifications of parabolic solar dish Stirling systems and their applications. *Energy Reports*, vol. 8, p. 4128-4155, **DOI:10.1016/j.egyr.2022.03.031**.

[12] Qiu, H., Wang, K., Yu, P., Ni, M., Xiao, G. (2021). A third-order numerical model and transient characterization of a b-type Stirling engine. *Energy*, vol. 222, 119973, **DOI:10.1016/j.energy.2021.119973**.

[13] Cheng, C.H., Yu, Y.J. (2010). Numerical model for predicting thermodynamic cycle and thermal efficiency of a beta-type Stirling engine with rhombic-drive mechanism. *Renewable Energy*, vol. 35, no. 11, p. 2590-2601, **DOI:10.1016/j.renene.2010.04.002**.

[14] Karabulut, H., Çınar, C., Öztürk, E., Yücesu, H.S. (2010). Torque and power characteristics of a helium charged Stirling engine with a lever controlled displacer driving mechanism. *Renewable Energy*, vol. 35, no. 1, p. 138-143, **DOI:10.1016/j.renene.2009.04.023**.

[15] Cheng, C.H., Yang, H.S. (2012). Optimization of geometrical parameters for Stirling engines based on theoretical analysis. *Applied Energy*, vol. 92, p. 395-405, **DOI:10.1016/j.apenergy.2011.11.046**.

[16] Topgül, T., Okur, M., Şahin, F., Çınar, C. (2022). Experimental investigation of the effects of hot-end and cold-end connection on the performance of a gamma type Stirling engine. *Engineering Science and Technology, an International Journal*, vol. 36, 101152, **DOI:10.1016/j.jestch.2022.101152**.

[17] Kongtragool, B., Wongwises, S. (2006). Thermodynamic analysis of a Stirling engine including dead volumes of hot space, cold space and regenerator. *Renewable Energy*, vol. 31, no. 3, p. 345-359, **DOI:10.1016/j.renene.2005.03.012**.

[18] Ahmed, F., Zhu, S., Yu, G., Luo, E. (2022). A potent numerical model coupled with multi-objective NSGA-II algorithm for the optimal design of Stirling engine. *Energy*, vol. 247, 123468, **DOI:10.1016/j.energy.2022.123468**.

[19] Raghavendra, H., Raju, P.S., Reddy, K.H. (2022). Effect of geometric and operational parameters on the performance of a beta-type Stirling engine: A numerical study. *Iranian Journal of Science and Technology, Transactions of Mechanical Engineering*, vol. 46, p. 1-13, **DOI:10.1007/s40997-020-00406-0**.

[20] Ahmed, F., Hulin, H., Khan, A.M. (2019). Numerical modeling and optimization of beta-type Stirling engine. *Applied Thermal Engineering*, vol. 149, p. 385-400, **DOI:10.1016/j.applthermaleng.2018.12.003**.

[21] Aksoy, F., Karabulut, H., Çınar, C., Solmaz, H., Özgören, Y.Ö., Uyumaz, A. (2015). Thermal performance of a Stirling engine powered by a solar simulator. *Applied Thermal Engineering*, vol. 86, p. 161-167, **DOI:10.1016/j.applthermaleng.2015.04.047**.

[22] Cavallaro, F., Zavadskas, E.K., Streimikiene, D., Mardani, A. (2019). Assessment of concentrated solar power (CSP) technologies based on a modified intuitionistic fuzzy topsis and trigonometric entropy weights. *Technological Forecasting and Social Change*, vol. 140, p. 258-270, **DOI:10.1016/j.techfore.2018.12.009**.

[23] Sharma, A. (2011). A comprehensive study of solar power in India and world. *Renewable and Sustainable Energy Reviews*, vol. 15, no. 4, p. 1767-1776, **DOI:10.1016/j.rser.2010.12.017**.

[24] Kumar, A., Sharma, M., Thakur, P., Thakur, V.K., Rahatekar, S.S., Kumar, R. (2020). A review on exergy analysis of solar parabolic collectors. *Solar Energy*, vol. 197, p. 411-432, **DOI:10.1016/j.solener.2020.01.025**.

[25] Zhu, J., Wang, K., Li, G., Wu, H., Jiang, Z., Lin, F., Li, Y. (2016). Experimental study of the energy and exergy performance for a pressurized volumetric solar receiver. *Applied Thermal Engineering*, vol. 104, p. 212-221, **DOI:10.1016/j.applthermaleng.2016.05.075**.

[26] Zayed, M.E., Zhao, J., Li, W., Elsheikh, A.H., Zhao, Z., Khalil, A., Li, H. (2020). Performance prediction and techno-economic analysis of solar dish/stirling system for electricity generation. *Applied Thermal Engineering*, vol. 164, 114427, **DOI:10.1016/j.applthermaleng.2019.114427**.

[27] Hijazi, H., Mokhiamar, O., Elsamni, O. (2016). Mechanical design of a low cost parabolic solar dish concentrator. *Alexandria Engineering Journal*, vol. 55, no. 1, p. 1-11, **DOI:10.1016/j.aej.2016.01.028**.

[28] Shufat, S.A., Kurt, E., Cinar, C., Aksoy, F., Hançerlioğulları, A., Solmaz, H. (2019). Exploration of a Stirling engine and generator combination for air and helium media. *Applied Thermal Engineering*, vol. 150, p. 738-749, **DOI:10.1016/j.applthermaleng.2019.01.053**.

[29] Kentfield, J.A.C. (1992). The thermodynamics of Stirling engines revisited: The relative merits of hot zone or cold zone work extraction. *SAE Technical Paper*, 929026, **DOI:10.4271/929026**.

[30] Cinar, C., Yucesu, S., Topgul, T., Okur, M. (2005). Beta-type Stirling engine operating at atmospheric pressure. *Applied Energy*, vol. 81, no. 4, p. 351-357, **DOI:10.1016/j.apenergy.2004.08.004**.

[31] Chahartaghi M., Sheykhi M. (2019). Energy, environmental and economic evaluations of a CCHP system driven by Stirling engine with helium and hydrogen as working gases. *Energy*, vol. 174, p. 1251-1266, **DOI:10.1016/j.energy.2019.03.012**.

[32] Ben-Mansour, R., Abuelyamen, A., Mokheimer, E.M.A. (2017). CFD analysis of radiation impact on Stirling engine performance. *Energy Conversion and Management*, vol. 152, p. 354-365, **DOI:10.1016/j.enconman.2017.09.056**.

[33] Cheng, C.H., Yang, H.S., Keong, L. (2013). Theoretical and experimental study of a 300-W beta-type Stirling engine. *Energy*, vol. 59, p. 590-599, **DOI:10.1016/j.energy.2013.06.060**.

[34] Karabulut, H., Düzgün, M., Topgül, T. (2023). Nodal thermodynamic analysis of a three-cylinder gamma-type Stirling engine and a conventional gamma-type Stirling engine and performance comparison. *Journal of the Faculty of Engineering and Architecture of Gazi University*, vol. 38, no. 1, p. 45-56, **DOI:10.17341/gazimmfd.944333**.

[35] Ipci, D. (2021). Thermodynamic analysis of a gamma-type Stirling engine driven by Scotch Yoke mechanism. *International*

Journal of Green Energy, vol. 18, no. 2, p. 144-155, **DOI:10.1080/15435075.2020.1831512**.

[36] Cinar, C., Ozdemir, A.O., Karabulut, H., Duzgun, M. (2021). Nodal thermodynamic and dynamic analysis of a free displacer Stirling engine. *Journal of Thermal Science and Technology*, vol. 41, no. 1, p. 141-155, **DOI:10.47480/isibted.979390**.

[37] Bataineh, K.M. (2018). Numerical thermodynamic model of alpha-type Stirling engine. *Case Studies in Thermal Engineering*, vol. 12, p. 104-116, **DOI:10.1016/j.csite.2018.03.010**.

[38] İpci, D., Karabulut, H. (2018). Thermodynamic and dynamic analysis of an alpha type Stirling engine and numerical treatment. *Energy Conversion and Management*, vol. 169, p. 34-44, **DOI:10.1016/j.enconman.2018.05.044**.

[39] Karabulut, H., Çınar, C., Aksoy, F., Solmaz, H., Özgören, Y.Ö., Arslan, M. (2016). Design and performance tests of a beta type rhombic driven stirling engine. *Journal of the Faculty of Engineering and Architecture of Gazi University*, vol. 31, no. 4, p. 879-888, **DOI:10.17341/gazimmfd.278443**.

[40] Karabulut, H., Solmaz, H., Okur, M., Şahin, F. (2013). Dynamic and thermodynamic analysis of gamma type free-piston Stirling engine. *Journal of the Faculty of Engineering and Architecture of Gazi University*, vol. 28, no. 2, p. 265-273.

[41] Nour, M., Kosaka, H., Bady, M., Sato, S., Abdel-Rahman, A.K. (2017). Combustion and emission characteristics of DI diesel engine fuelled by ethanol injected into the exhaust manifold. *Fuel Processing Technology*, vol. 164, p. 33-50, **DOI:10.1016/j.fuproc.2017.04.018**.

[42] Karagöz, Y., Balcı, Ö., Köten, H. (2019). Investigation of hydrogen usage on combustion characteristics and emissions of a spark ignition engine. *International Journal of Hydrogen Energy*, vol. 44, no. 27, p. 14243-14256, **DOI:10.1016/j.ijhydene.2019.01.147**.

[43] Akcay, M., Yilmaz, I.T., Feyzioglu, A. (2021). The influence of hydrogen addition on the combustion characteristics of a common-rail CI engine fueled with waste cooking oil biodiesel/diesel blends. *Fuel Processing Technology*, vol. 223, 106999, **DOI:10.1016/j.fuproc.2021.106999**.

[44] Huang, Y., He, X., Zhang, H., Wei, J., Sng, D.W.M. (2021). Spark ignition and stability limits of spray kerosene flames under subatmospheric pressure conditions. *Aerospace Science and Technology*, vol. 114, 106734, **DOI:10.1016/j.ast.2021.106734**.

[45] Rocha, D.D., Radicchi, F.C., Lopes, G.S., Brunocilla, M.F., Gomes, P.C.F., Santos, N.D.S.A., Malaquias, A.C.T., Filho, F.A.R., Baêta, J.G.C. (2021). Study of the water injection control parameters on combustion performance of a spark-ignition engine. *Energy*, vol. 217, 119346, **DOI:10.1016/j.energy.2020.119346**.

[46] Karabulut, H., Çınar, C., Topgül, T., Uysal, L.K. (2022, Ahead of Print). Combined dynamic and thermodynamic investigation of a crank-shifted alpha-type Stirling engine. *Arabian Journal for Science and Engineering*, **DOI:10.1007/s13369-022-06980-6**.

[47] Karabulut, H., Okur, M., Ozdemir, A.O. (2019). Performance prediction of a Martini type of Stirling engine. *Energy Conversion and Management*, vol. 179, p. 1-12, **DOI:10.1016/j.enconman.2018.10.059**.

[48] Xiao, G., Qiu, H., Wang, K., Wang, J. (2021). Working mechanism and characteristics of gas parcels in the Stirling cycle. *Energy*, vol. 229, 120708, **DOI:10.1016/j.energy.2021.120708**.

[49] Alfarawi, S., Al-Dadah, R., Mahmoud, S. (2016). Enhanced thermodynamic modelling of a gamma-type Stirling engine. *Applied Thermal Engineering*, vol. 106, p. 1380-1390, **DOI:10.1016/j.applthermaleng.2016.06.145**.

[50] Eid, E. (2009). Performance of a beta-configuration heat engine having a regenerative displacer. *Renewable Energy*, vol. 34, no. 11, p. 2404-2413, **DOI:10.1016/j.renene.2009.03.016**.

Strojniški vestnik - Journal of Mechanical Engineering 68(2022)12, 771-780
DOI:10.5545/sv-jme.2022.284
Original Scientific Paper
Received for review: 2022-07-14
Received revised form: 2022-10-27
Accepted for publication: 2022-12-16

Adaptive Super-twisting Sliding Mode Control of Hydraulic Servo Actuator with Nonlinear Features and Modeling Uncertainties

Zhenshuai Wan[1,2*] – Yu Fu[1,2] – Longwang Yue[1] – Chong Liu[1]

[1] Henan University of Technology, School of Mechanical and Electrical Engineering, China
[2] Henan University of Technology, Key Laboratory of Grain Information Processing and Control of Ministry of Education, China

This study proposes a novel adaptive super-twisting sliding mode controller (ASTSMC) for hydraulic servo actuator with nonlinear features and modeling uncertainties. In the proposed method, an extended state observer (ESO) is utilized to estimate the value of lumped uncertainties. The core feature of this paper is the combination of ASTSMC with ESO to compensate disturbance in hydraulic servo actuator. Moreover, the proposed ASTSMC does not need to obtain the bound of uncertainties in advance and ensures that the sliding variable and its derivative reach to zero in a finite time. In addition, the stability of the closed-loop is proved by Lyapunov theory. Simulation and experiment results demonstrate that the proposed ASTSMC can effectively mitigate the lumped uncertainties and obviously improve the tracking performance.
Keywords: hydraulic servo actuator, nonlinear features, modeling uncertainties, super-twisting sliding mode control

Highlights

- *The dynamic mathematical model of hydraulic servo actuator is established considering nonlinear features and modeling uncertainties.*
- *The ESO is used to estimate the unmeasured system state and lumped uncertainties.*
- *The ASTSMC is adopted to compensate the disturbance and further improve the tracking precision.*
- *The simulation and experiment results validate the effectiveness of the ASTSMC based on ESO.*

0 INTRODUCTION

Hydraulic servo actuator is widely employed in modern industrial, such as heavy vehicle [1] and [2], load simulator [3], hot-pressing equipment [4], hydraulic manipulator [5], due to the virtues of small size-to-power ratio, high control precision, fast response performance and strong bearing capacity [6] to [8]. However, the nonlinear features and modeling uncertainties of hydraulic servo actuator complicates the dynamic model and hinders position tracking performance. The nonlinear features are mainly caused by pressure-flow characteristic of servo valve and nonlinear friction of hydraulic actuator [9] to [12]. While the modeling uncertainties are mostly caused by time-varying hydraulic parameters, unmodeled friction and external disturbance [13] to [15]. Hence, the traditional linear control schemes have become more and more difficult to satisfy the high precision position tracking control requirement of modern hydraulic servo actuator. Importantly, it is essential to study high performance control strategy for hydraulic servo actuator.

In recent years, numerous control schemes have been proposed, such as adaptive control [16], robust control [17], backstepping control [18], sliding mode control (SMC) [19], and intelligent control [20] to improve the control performance of hydraulic servo system. As an effective control method, SMC can cope with uncertainties and achieve asymptotic tracking performance [21] to [23]. However, the inevitable chattering of SMC caused by discontinuous control input is not acceptable for practical systems. To solve this problem, the continuous switching function, such as continuous saturation function and hyperbolic function, is used to replace the discontinuous symbol function in conventional SMC. Although the tracking error of improved control scheme is bounded, it loses the asymptotic tracking performance. The high order sliding mode controller can ensure the continuity of SMC and obtain the asymptotic tracking performance. However, it needs the derivative information of the sliding mode variable, which is often unattainable in practice, so it is difficult to be realized in engineering practice. In hydraulic servo system, only parts of states can be measured, and load or disturbance cannot be measured directly. Hence, an ESO is used to estimate the immeasurable system state variables and lumped uncertainties in this paper [24]. The proposed ASTSMC can effectively avoid the above drawbacks, but the controller gain related to the upper bound of modeling uncertainty needs to be

*Corr. Author's Address: School of Mechanical and Electrical Engineering, Henan University of Technology, Zhengzhou, 450001, China, wanzhenshuai@haut.edu.cn

set artificially, which is conservative to some extent. The feedforward adaptive control law based on model is introduced into the ASTSMC to improve the control precision of actuator. Moreover, the proposed method does not need to know the exact bound of modeling uncertainty, rather designs an adaptive law to constantly adjust the controller gain associated with the bound. In particular, ASTSMC can make the tracking error converge asymptotically to a small adjustable range near zero in finite time.

The rest of this paper is organized as follows. Section 1 gives system description and dynamical model. The ASTSMC design process and theoretical result are presented in section 2. Simulation results and discussion are depicted in section 3. Section 4 carries experimental setup and comparative results. Finally, the conclusions are summarized in section 5.

1 SYSTEM DESCRIPTION AND DYNAMICAL MODEL

The schematic diagram of the hydraulic servo actuator is given in Fig. 1, which mainly includes pump, motor, servo valve and hydraulic actuator.

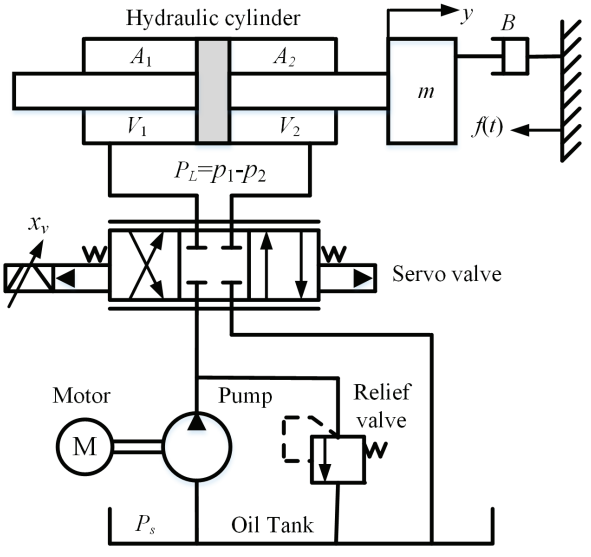

Fig. 1. *Schematic diagram of the hydraulic servo actuator*

The system mainly consists of three subsystems which are the servo system, the hydraulic part and the mechanical section. The hydraulic part supplies energy for overall equipment. The servo system provides the hydraulic pressure to the mechanical section by controlling the piston's movement. As an executive part, the performance of actuator directly influences the precision of hydraulic driven system. However, many hydraulic servo actuator models have not adequately account for the impact of nonlinear features and modeling uncertainties. To improve the position control performance of the hydraulic servo actuator, the dynamic model considering various disturbance and uncertainties is used to replace the traditional linear model.

According to the Newton's second law, the dynamic equation of load can be described as

$$m\ddot{y} = P_L A - B\dot{y} - f(t), \tag{1}$$

where m is the equivalent load mass, y is the load displacement, P_L is the load pressure, A is of effective piston area of hydraulic cylinder, B is viscous friction coefficient, $f(t)$ is the nonlinear features and modeling uncertainties.

Ignoring external leakage of hydraulic cylinder, the dynamic equation of load pressure can be written as

$$\frac{V_t}{4\beta_e}\dot{P}_L = Q_L - A\dot{y} - C_t P_L + q(t), \tag{2}$$

where V_t is total volume of hydraulic actuator, β_e is the effective bulk modulus of the hydraulic fluid, Q_L is load flow, C_t is the internal leakage coefficient of hydraulic cylinder, $q(t)$ is the disturbance.

The load flow of servo valve can be constructed as

$$Q_L = k_t u\sqrt{P_s - \text{sign}(u)P_L}, \tag{3}$$

where k_t is the flow gain coefficient, u is the input control voltage of the servo valve, P_s is the supply pressure of the pump, sign(u) is defined as

$$\text{sign}(u) = \begin{cases} 1, & \text{if } u \geq 0 \\ -1, & \text{if } u < 0 \end{cases}. \tag{4}$$

For the ease of calculation, let the system states be defined as

$$x = [x_1, x_2, x_3]^T = [y, \dot{y}, \ddot{y}]^T. \tag{5}$$

Combing Eqs. (1) to (5), the state space model of the hydraulic servo actuator is given by

$$\begin{cases} \dot{x}_1 = x_2 \\ \dot{x}_2 = x_3 \\ \dot{x}_3 = f_1(u, P_L)u - f_2(x_2) - f_3(x_3) + d(t) \end{cases}, \tag{6}$$

where

$$\begin{cases} f_1(t)=\dfrac{4\beta_e A k_t}{mV_t}\sqrt{P_s-\text{sign}(u)P_L} \\ f_2(t)=\dfrac{4\beta_e}{mV_t}\left(A^2+BC_t\right)x_2 \\ f_3(t)=\dfrac{4\beta_e}{mV_t}\left(C_t m+\dfrac{BV_t}{4\beta_e}\right)x_3 \\ d(t)=\dfrac{4\beta_e A}{mV_t}q(t)-\dfrac{4\beta_e C_t}{mV_t}f(t)-\dfrac{\dot{f}(t)}{m} \end{cases}.$$

The greatest difficulties in this model is the high nonlinearity with respect the control signal and unmodeled disturbance for hydraulic servo actuator. To cope with this problem, the ASTSMC is utilized to drive the load track the desired trajectory as closely as possible.

2 CONTROLLER DESIGN

2.1 Extended State Observer

Set the lumped uncertainties of $d(t)$ as an extended state x_4, then Eq. (6) can be rewritten as

$$\begin{cases} \dot{x}_1=x_2 \\ \dot{x}_2=x_3 \\ \dot{x}_3=f_1(u,P_L)u-f_2(x_2)-f_3(x_3)+x_4 \\ \dot{x}_4=\dot{d}(t) \end{cases}. \quad (7)$$

Note that $q(t)$ and $f(t)$ are bounded, thus $d(t)$ is bounded by a known positive constant δ.

Design an ESO of the Eq. (7) as

$$\begin{cases} \dot{\hat{x}}_1=\hat{x}_2-\beta_1\left(\hat{x}_1-x_1\right) \\ \dot{\hat{x}}_2=\hat{x}_3-\beta_2\left(\hat{x}_1-x_1\right) \\ \dot{\hat{x}}_3=\hat{f}_1\left(u,P_L\right)u-\hat{f}_2\left(x_2\right)-\hat{f}_3\left(x_3\right)+\hat{x}_4-\beta_3\left(\hat{x}_1-x_1\right) \\ \dot{\hat{x}}_4=-\beta_4\left(\hat{x}_1-x_1\right) \end{cases}, \quad (8)$$

where $\hat{x}_i$ is the estimation states of the ESO, $\hat{f}_i$ is the estimations of f_i, β_i is the observe gains to be determined.

Define $\varepsilon_i=x_i-\hat{x}_i$, the dynamic of error is

$$\begin{aligned} \dot{\varepsilon} &= A\varepsilon-L(\hat{x}_1-x_1)+B_w d+F \\ &= \left(A-LC\right)\varepsilon+B_w d+F, \end{aligned} \quad (9)$$

where $\tilde{f}_i$ is the estimation error of f_i, and

$$A=\begin{bmatrix} 0&1&0&0\\0&0&1&0\\0&0&0&1\\0&0&0&0 \end{bmatrix},\ L=\begin{bmatrix}\beta_1\\\beta_2\\\beta_3\\\beta_4\end{bmatrix},\ C=\begin{bmatrix}1\\0\\0\\0\end{bmatrix}^T,\ B_w=\begin{bmatrix}0\\0\\0\\1\end{bmatrix},$$

$$F=\begin{bmatrix}0\\0\\\tilde{f}_1u-\tilde{f}_2-\tilde{f}_3\\0\end{bmatrix}.$$

To ensure the pole of matrix $(A-LC)$ on the left half plane, the characteristic polynomial can be written as

$$\lambda_0(s)=\left[sI-(A-LC)\right]=(s+w_0)^4, \quad (10)$$

where w_0 is the bandwidth of the observe.

The parameters of ESO are selected as

$$\beta_1=4w_0,\ \beta_2=-6w_0^2,\ \beta_3=4w_0^3,\ \beta_4=-4w_0^4. \quad (11)$$

Assumption 1: The unmodeled disturbances are bounded and satisfy

$$d(t)\le M_1,\left|\dot{d}(t)\right|\le M_2,\left|F(t)\right|\le M_3, \quad (12)$$

where M_1, M_2, M_3 are unknown positive constants.

Theorem 1: The estimated error of the ESO can be expressed as

$$\lim_{t\to\infty}\varepsilon(t)=0. \quad (13)$$

Proof: Define A_1=$A-LC$, then

$$\begin{aligned} \varepsilon(t) &= \exp(A_1t)\varepsilon(0)+\int_0^t\exp((A_1(t-\tau))Fd\tau \\ &+\int_0^t\exp((A_1(t-\tau))B_w d(t)d\tau. \end{aligned} \quad (14)$$

Using the property of matrix norms, Eq. (14) can be represented as

$$\begin{aligned} \left\|\varepsilon(t)\right\| &\le \left\|\exp(A_1t)\right\|\left\|\varepsilon(0)\right\| \\ &+\int_0^t\left\|\exp((A_1(t-\tau))\right\|\left\|B_w\right\|\left\|d(t)\right\|d\tau \\ &+\int_0^t\left\|\exp((A_1(t-\tau))\right\|\left\|F\right\|d\tau. \end{aligned} \quad (15)$$

Based on Eq. (10), the eigenvalues of A_1 are λ_1=λ_2=λ_3=$-w_0$, then there exists $\kappa>1$ such that for all $t\ge0$

$$\begin{cases} \left\|\exp(A_1t)\right\|\le\kappa\exp(-w_0) \\ \left\|\exp((A_1(t-\tau))\right\|\le\kappa\exp(-w_0(t-\tau)) \end{cases}. \quad (16)$$

Then the Eq. (15) can be represented as

$$\|\varepsilon(t)\| \le \kappa \|\exp(-w_0 t)\| \|\varepsilon(0)\| + \frac{\kappa M_1}{w_0}\left(1-\exp(-w_0 t)\right) + \frac{\kappa M_3}{w_0}\left(1-\exp(-w_0 t)\right). \quad (17)$$

Therefore, if the w_0 goes to infinity, the $\varepsilon(t)$ would be convergent to zero.

2.2 Adaptive Super-twisting Sliding Mode Controller

The tracking errors are defined as

$$\begin{cases} z_1 = x_1 - x_{1d} \\ z_2 = x_2 - \dot{x}_{1d} \\ z_3 = x_3 - \ddot{x}_{1d} \end{cases}, \quad (18)$$

where z_1, z_2, z_3 are tracking error of position, velocity and acceleration, respectively.

The sliding mode surface is defined as

$$s = k_1 z_1 + k_2 z_2 + z_3, \quad (19)$$

where k_1 and k_2 are positive constants.

The derivative of s can be written as

$$\dot{s} = k_1 z_2 + k_2 z_3 + \dot{z}_3 = k_1 z_2 + k_2 z_3 + f_1(u, P_L)u - f_2(x_2) - f_3(x_3) - \dddot{x}_{1d}. \quad (20)$$

The control input of super-twisting sliding mode controller is designed as

$$u = \frac{1}{f_1(u, P_L)} \left\{ \underbrace{f_2(x_2) + f_3(x_3) + \dddot{x}_{1d}}_{u_1} - k_1 z_1 - k_2 z_3 - \alpha |s|^{1/2} \operatorname{sign}(s) \underbrace{- \int_0^\tau \frac{\theta}{2} \operatorname{sign}(s)}_{u_2} \right\}, \quad (21)$$

where u_1 and u_2 are feedforward control law and robust control law, α and θ are time varying controller gains.

The adaptive laws are defined as

$$\begin{cases} \dot{\alpha} = \gamma_1 \sqrt{\omega / 2} \operatorname{sign}\left(|s| - \nu\right) \\ \theta = 2\varepsilon\alpha \end{cases}, \quad (22)$$

where γ_1, ω, θ, ν are positive constants.

According to Eqs. (21) and (22), the dynamics of s are represented as

$$\begin{cases} \dot{s} = -\alpha |s|^{1/2} \operatorname{sign}(s) + \eta + d(t) \\ \dot{\eta} = -\frac{\theta}{2} \operatorname{sign}(s) \end{cases}. \quad (23)$$

Define state vector $\xi = [\xi_1, \xi_2]^T = [|s|^{1/2} \operatorname{sign}(s), \eta]^T$, then the unmodeled uncertainties are expressed as

$$d(t) = \rho(x,t)|s|^{1/2} \operatorname{sign}(s) = \rho(x,t)\xi_1, \quad (24)$$

where $\rho(x,t)$ is a positive function.

Then, the new state equation is defined as

$$\dot{\xi} = A\xi, \quad (25)$$

where $A = \frac{1}{2|\xi_1|}\begin{bmatrix} \rho(x,t) - \alpha & 1 \\ -\theta & 0 \end{bmatrix}$.

A Lyapunov function is represented as

$$V = V_0 + \frac{1}{2\psi_1}(\alpha - \alpha_0)^2 + \frac{1}{2\psi_2}(\theta - \theta_0)^2, \quad (26)$$

where α_0 and β_0 are positive constants. V_0 is defined as follows

$$V_0 = \xi^T P \xi, \quad (27)$$

where $P = \begin{bmatrix} \lambda + 4\varepsilon^2 & 2\varepsilon \\ -2\varepsilon & 1 \end{bmatrix}$, λ is a positive constant.

The derivative of V_0 is written as

$$\dot{V}_0 = \dot{\xi}^T P \xi + \xi^T P \dot{\xi} = \xi^T (A^T P + PA)\xi = -\frac{1}{2|\xi_1|}\xi^T \Lambda \xi, \quad (28)$$

where

$$\Lambda = \begin{bmatrix} \Lambda_{11} & \Lambda_{12} \\ \Lambda_{21} & \Lambda_{22} \end{bmatrix}, \Lambda_{11} = -2(\lambda + 4\varepsilon^2)(\rho - \alpha) - 4\varepsilon\theta,$$
$$\Lambda_{12} = 2\varepsilon(\rho - \alpha) + \theta - \lambda - 4\varepsilon^2,$$
$$\Lambda_{21} = 2\varepsilon(\rho - \alpha) + \theta - \lambda - 4\varepsilon^2, \Lambda_{22} = 4\varepsilon.$$

When α satisfies

$$\alpha > \frac{\delta(\lambda + 4\varepsilon^2) - \varepsilon}{\lambda(1 - \psi_1)} + \frac{(2\varepsilon\delta - \lambda - 4\varepsilon^2)^2}{12\varepsilon\lambda(1 - \psi_1)}. \quad (29)$$

We have

$$\dot{V}_0 \le -\frac{\varepsilon}{|\xi_1|}\xi^T \xi = -\frac{\varepsilon}{|\xi_1|}\|\xi\|. \quad (30)$$

According to the following inequalities

$$\begin{cases} \lambda_{\min}(P)\|¾\|^2 \le ¾^T P ¾ \le \lambda_{\max}(P)\|¾\|^2 \\ |\xi_1| = |s|^{1/2} \le \|¾\|^2 \le \dfrac{V_0^{1/2}}{\lambda_{\min}^{1/2}(P)} \end{cases}, \quad (31)$$

where $\lambda_{\max}(P)$ and $\lambda_{\min}(P)$ are maximum and minimum eigenvalue of matrix P, respectively.

Thus, Eq. (31) can be rewritten as

$$\dot{V}_0 \le -\zeta V_0^{1/2}, \quad (32)$$

where $\zeta = \varepsilon\lambda_{\min}^{1/2}(\boldsymbol{P})/\lambda_{\max}(\boldsymbol{P})$.

Then, the time derivative can be given as

$$\begin{aligned}\dot{V} &= \dot{V}_0 + \frac{1}{\psi_1}(\alpha-\alpha_0)\dot{\alpha} + \frac{1}{\psi_2}(\theta-\theta_0)\dot{\theta} \\ &\le -\sigma V_0^{1/2}\frac{1}{\psi_1}(\alpha-\alpha_0)\dot{\alpha} + \frac{1}{\psi_2}(\theta-\theta_0)\dot{\theta} \\ &+ \frac{\gamma_1}{\sqrt{2\psi_1}}|\alpha-\alpha_0| + \frac{\gamma_2}{\sqrt{2\psi_2}}|\theta-\theta_0|,\end{aligned} \tag{33}$$

where $\sigma = \min\{\zeta, \gamma_1, \gamma_2\}$.

$$\begin{aligned}\dot{V} &\le -\sigma V_0^{1/2} + \frac{1}{\psi_1}(\alpha-\alpha_0)\dot{\alpha} + \frac{1}{\psi_2}(\theta-\theta_0)\dot{\theta} \\ &+ \frac{\gamma_1}{\sqrt{2\psi_1}}|\alpha-\alpha_0| + \frac{\gamma_2}{\sqrt{2\psi_2}}|\theta-\theta_0|.\end{aligned} \tag{34}$$

Based on Eq. (22), there exists positive constants α_0 and β_0, which satisfy $\alpha-\alpha_0<0$ and $\beta-\beta_0<0$. Then Eq. (33) can be represented as

$$\begin{cases}\dot{\alpha} = \gamma_1\sqrt{\psi_1/2}, \dot{\theta} = \gamma_2\sqrt{\psi_2/2} & |s| > v \\ \dot{\alpha} = -\gamma_1\sqrt{\psi_1/2}, \dot{\theta} = -\gamma_2\sqrt{\psi_2/2} & |s| < v\end{cases}, \tag{35}$$

Assuming $v=0$, we know that $s\to 0$ in finite time, and

$$t_f \le \frac{2V^{1/2}(t_0)}{\sigma}. \tag{36}$$

3 SIMULATION RESULTS

To show the trajectory tracking performance of the presented ASTSMC, PID and SMC schemes are first utilized for simulation comparison. It should be noted that all controller parameters are set through a preliminary tuning process. The parameters of hydraulic servo actuator are listed in table 1.

1) PID: The gains of PID controller are tunned as $K_p=120$, $K_i=10$, $K_d=0.1$ to balance the steady-state error and transient response performance.
2) SMC: Based on SMC scheme, the control law is designed as

$$u = \frac{1}{f_1(u, P_L)}\left\{\begin{matrix} f_2(x_2) + f_3(x_3) + \ddot{x}_{1d} \\ -k_1 z_1 - k_2 z_3 - k_3 \text{sign}(s)\end{matrix}\right\}, \tag{37}$$

where $k_1=4\times10^3$, $k_2=2\times10^3$, $k_3=2\times10^2$.

3) ASTSMC: The parameters of proposed ASTSMC are given as $k_1=2\times10^3$, $k_2=6\times10^2$, $k_3=2\times10^2$ $\gamma_1=2$, $\omega=6$, $\theta=5$, $\nu=2$. Note that the sign function in Eq. (21) is replaced with saturation function for meeting the requirement of the control input continuous.

Table 1. *The parameters of hydraulic servo actuator*

Parameter	Value
m	300 kg
V_t	9×10^{-5} m^3
ρ	900 kg/m^3
B	1200 N·s/m
C_t	4×10^{-3}
β_e	6.9×10^8 Pa
K_t	7.2×10^{-7} m/V
A	3.14×10^{-4} m^2

To validate the advantages of the proposed ASTSMC, a sinusoidal signal $x_d=60\sin(20\pi t)$ mm is used as reference trajectory. The position tracking performance and tracking error are given in Figs. 2 and 3, from which we can see that the proposed ASTSMC is better than the SMC and PID. This is because the proposed ASTSMC can estimate the unknown dynamics by ESO and compensate that by adaptive control law. Compared with the PID controller, the tracking errors of SMC and ASTSMC are substantially reduced by 18.3 % and 48.8 %, respectively. Fig. 4 shows the control input of the three controllers. It is noted that owing to the adaptive mechanism in ASTSMC, its control input is smaller than PID and SMC. The observation performance of ESO to external interfererence is shown in Fig. 5. It is clearly indicated that the ESO can estimate the state variavbe and lumped uncertainties accurately.

In order to further authenticate the rationality of ASTMC, multi-frequency sinusoidal signal $x_d=50\sin(10\pi t)+40\sin(25\pi t)+20\sin(50\pi t)$ [mm] is selected as reference signal. Also, the simulation results are shown in Figs. 6 and 7. It is noted that three controllers can track the reference trajectory accurately. However, the proposed ASTSMC obtains the smallest tracking error than SMC and PID, which verifies the superiority of the proposed controller. The maximum tracking errors of PID, SMC and ASTSM are 20.471 mm, 14.237 mm, 8.690 mm, respectively.

In order to quantitatively compare the tracking performance of different controllers, maximum absolute value of tracking error M_e, average tracking error μ_e, and standard deviation of tracking error σ_e are adopted as performance indices. Table 2 summarizes the performance indices of different controllers for sinusoidal and multi-frequency sinusoidal motion reference signal. It can be found that the proposed ASTSMC produces the smallest values among three

controllers. In addition, the performance indices of SMC are better than PID. The simulation results clearly demonstrate that the proposed ASTSM can provide a better control performance for the hydraulic servo actuator with unknown dynamics than the others under different reference trajectories.

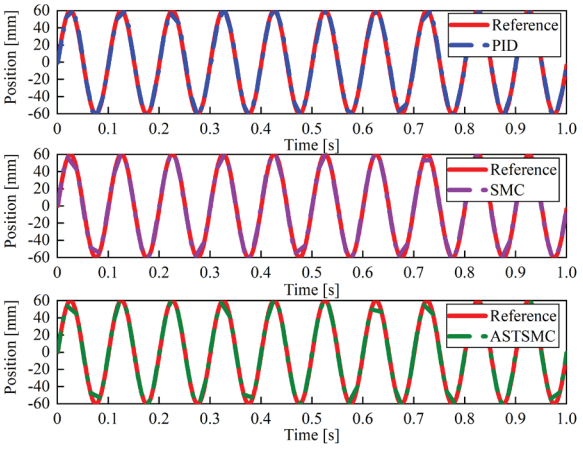

Fig. 2. *Position tracking of sinusoidal motion*

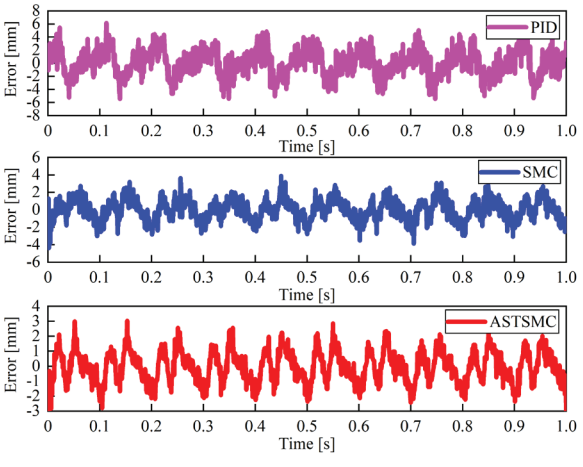

Fig. 3. *Tracking error of sinusoidal motion*

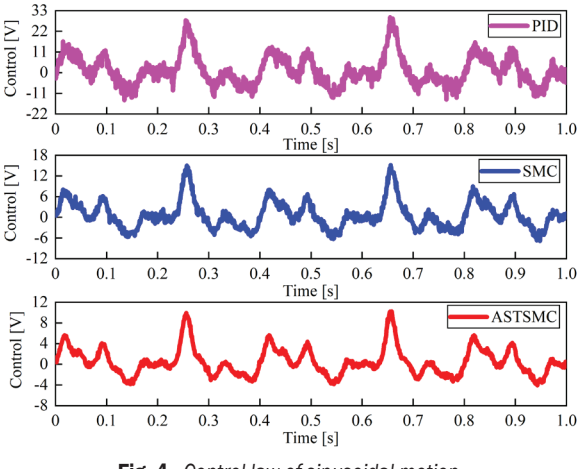

Fig. 4. *Control law of sinusoidal motion*

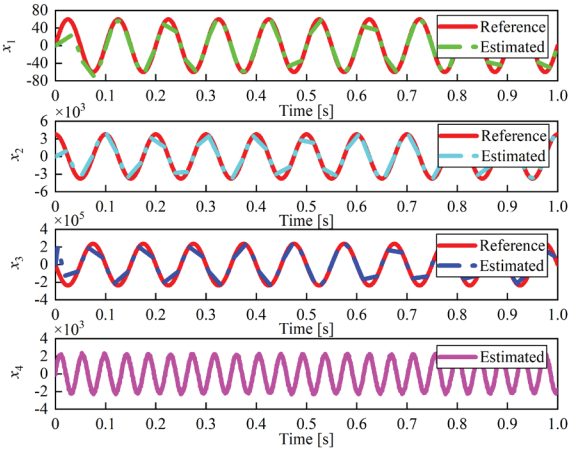

Fig. 5. *The observation performance of ESO*

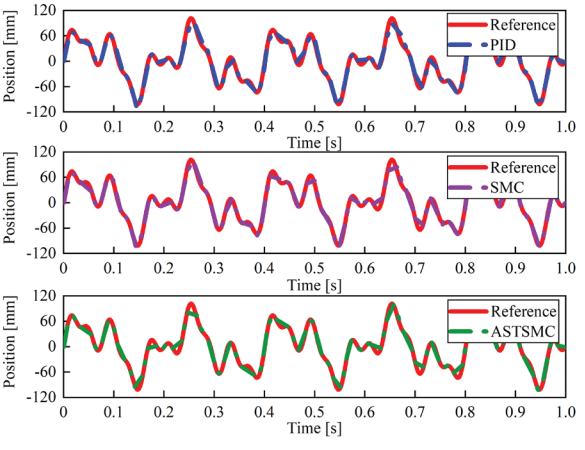

Fig. 6. *Position tracking of multi-frequency sinusoidal motion*

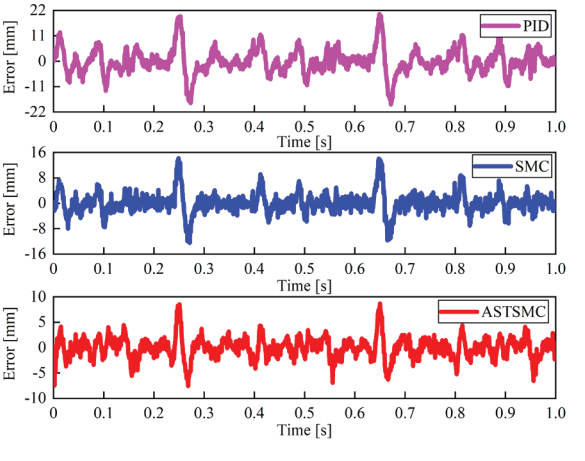

Fig. 7. *Tracking error of multi-frequency sinusoidal motion*

Table 2. *Comparison results of performance indices*

Signal	Controller	M_e	μ_e	σ_e
Sinusoidal	PID	6.147	1.682	1.225
	SMC	5.023	1.459	1.111
	ASTSMC	3.145	0.881	0.595
Multi-frequency sinusoidal	PID	20.471	3.909	3.825
	SMC	14.237	2.267	2.463
	ASTSMC	8.690	1.556	1.435

4 EXPERIMENTAL RESULTS

In this section, a hydraulic servo actuator experimental setup is used to demonstrate the effectiveness of the proposed control scheme. The diagram of experimental setup is shown in Fig 8. The host computer offers human-computer interaction interface for compiling programs and adjusting controller parameters. The Target computer reads the feedback signal real time and feeds it back to the host computer by TCP/IP protocol. The digital control signal is converted to analogue signal by D/A card and processed by signal conditioner, and then sent to the servo valve to drive the hydraulic servo actuator. The position and pressure information are collected by position sensor and pressure sensor, respectively. The A/D card obtains the sensors information and sends them to target computer to form closed-loop control system by signal conditioner.

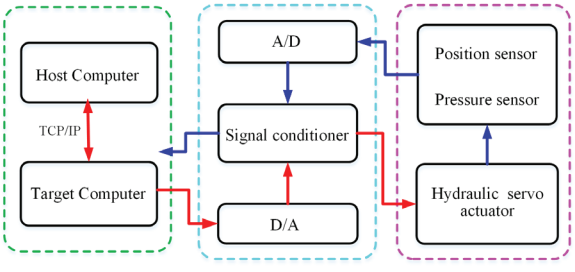

Fig. 8. *The diagram of experimental setup*

The load is first commanded to track a low-speed motion x_d=40sin(10πt) [mm]. The obtained position tracking and tracking error are displayed in Figs. 9 and 10. It can be seen that the proposed controller ASTSMC delivers smaller tracking error than PID and SMC, because they use ESO to estimate the lumped uncertainties. In addition, the tracking error of all controllers occurs chattering when the trajectory is reversed due to the unmodeled dynamic characteristic and measurement noise. However, the chattering value of the proposed ASTSMC is smaller to other controllers, which means that the control scheme based ESO and adaptive law is very helpful to alleviate the effects from lumped uncertainties in hydraulic system.

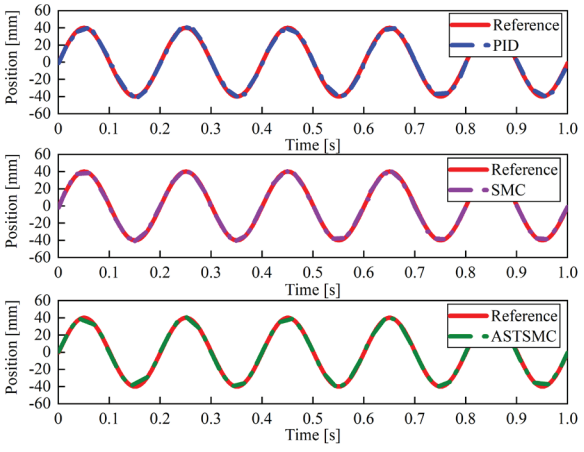

Fig. 9. *Position tracking of* $x_d = 40\sin(10\pi t)$ *[mm]*

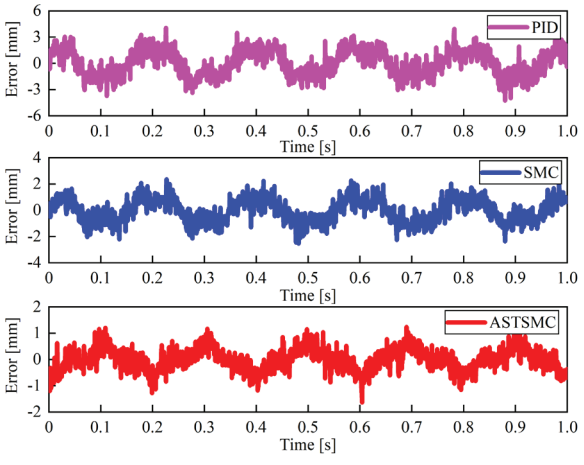

Fig. 10. *Tracking error of* $x_d = 40\sin(10\pi t)$ *[mm]*

To further verify the superiority of the ASTMC, a high-speed motion x_d = 40sin(15πt) is performed as reference signal. The experimental comparison results of three controllers are exhibited in Figs. 11 and 12. As presented, the proposed ASTSMC attains better tracking precision in comparison to the other controllers. This is because that the control gains in ASTSMC can dynamically be adjusted as unknown uncertainties changes.

In this case, a large amplitude motion signal x_d = 80sin(15πt) mm is chose as the reference trajectory with the amplitude of 80 mm and the frequency 7.5 Hz. The corresponding position tracking performance and tracking error are presented in Figs. 13 and 14. It is noted that the three controllers are all able to suppress the nonlinear features and modeling

uncertainties for such a large amplitude tracking test. However, the proposed ASTSMC shows excellent tracking performance than the other two compared controllers. The tracking error of ASTSMC is always within in 8 mm, showing a good tracking precision.

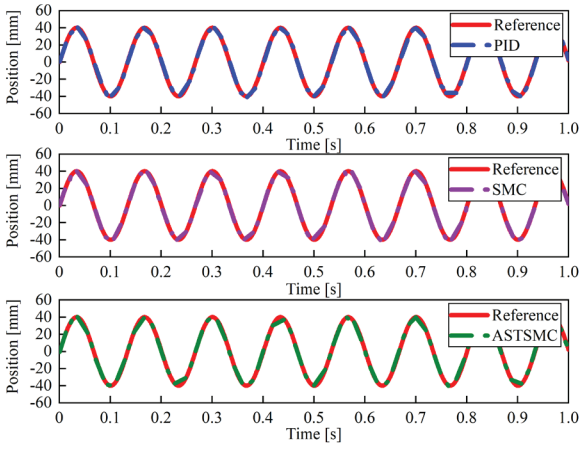

Fig. 11. *Position tracking of* $x_d = 40\sin(15\pi t)$ *[mm]*

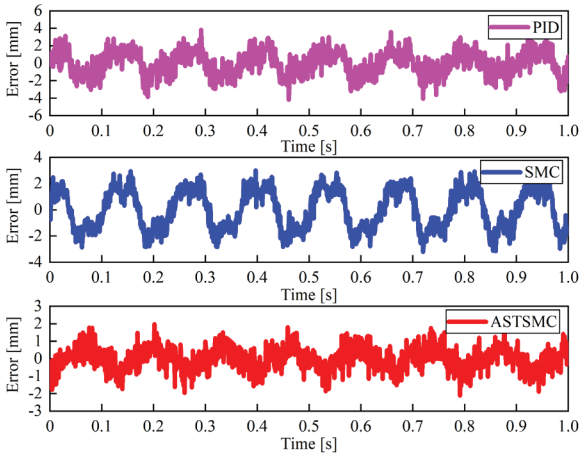

Fig. 12. *Tracking error of* $x_d = 40\sin(15\pi t)$ *[mm]*

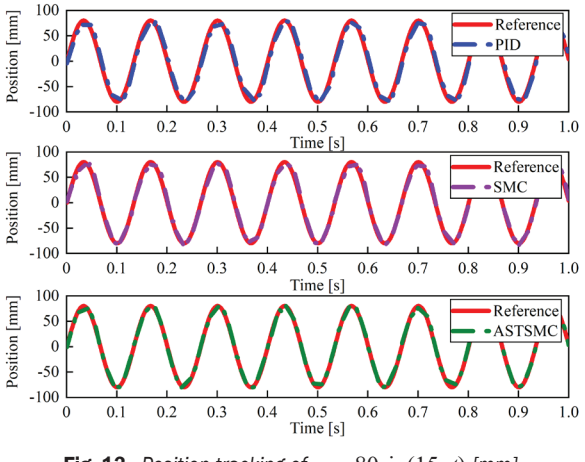

Fig. 13. *Position tracking of* $x_d = 80\sin(15\pi t)$ *[mm]*

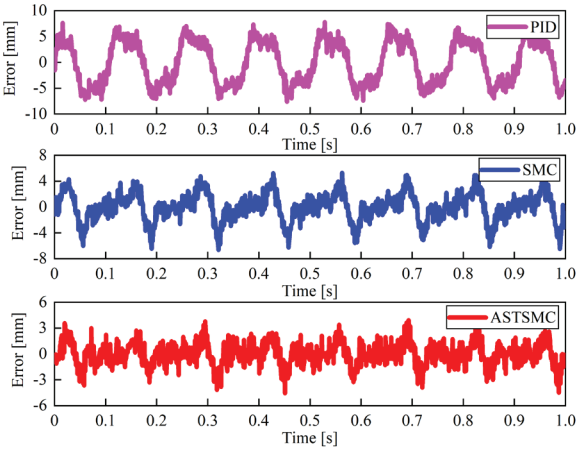

Fig. 14. *Tracking error of* $x_d = 80\sin(15\pi t)$ *[mm]*

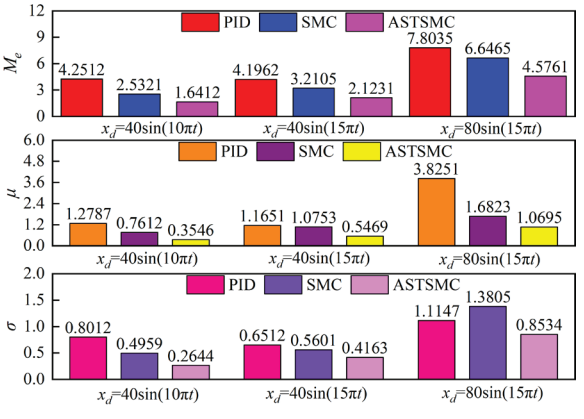

Fig. 15. *Comparison performance indices of controllers*

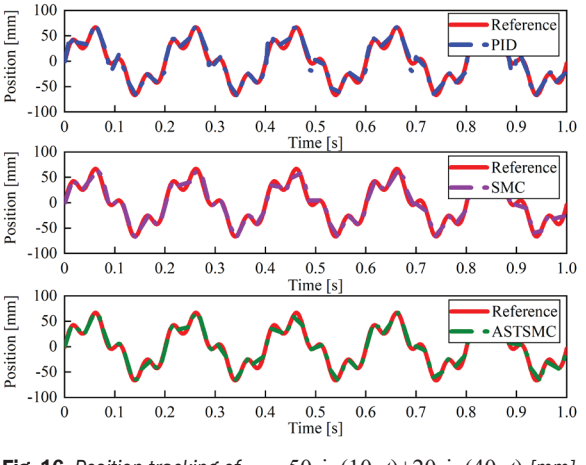

Fig. 16. *Position tracking of* $x_d = 50\sin(10\pi t)+20\sin(40\pi t)$ *[mm]*

The performance indices of three controllers for different sinusoidal motion are shown in Fig. 15. One can find that the values of performance indices with the ASTSMC are the smallest among all controllers. The maximum errors of above experimental situation are 1.6412 mm and 2.1231 mm for amplitude 40 mm, respectively. In particular, the maximum of relative average error of ASTSMC is within 1.35 %, which demonstrates the effectiveness of the proposed control scheme.

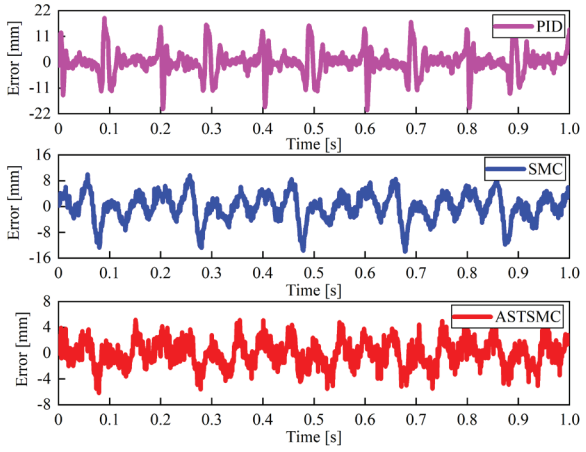

Fig. 17. Tracking error of $x_d = 50\sin(10\pi t)+20\sin(40\pi t)$ *[mm]*

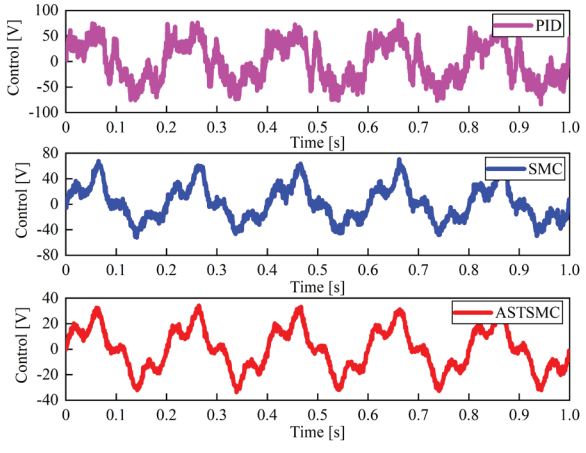

Fig. 18. *Control law of* $x_d = 50\sin(10\pi t)+20\sin(40\pi t)$ *[mm]*

Multi-frequency sinusoidal experimental results $x_d = 50\sin(10\pi t)+20\sin(40\pi t)$ are shown in Figs. 16 and 17. It can be seen that the presented controller ASTSMC can track the reference signal accurately, and the tracking error is smaller than SMC and PID. Especially, PID controller gives the worst control performance. It is evident that the tracking error of ASTSMC is within 5 mm, and that of PID, SMC is within 22 mm and 15 mmm, respectively, which proves the high-accuracy tracking performance of the designed control scheme again. The control inputs of different controllers are shown in Fig 18. As shown, although the input of all controller is bounded, the input of ASTSMC is smaller than PID and SMC.

5 CONCLUSIONS

In this paper, a ASTSMC scheme based on ESO has been proposed for hydraulic servo actuator with nonlinear features and modeling uncertainties. First, the dynamical mathematical model containing various nonlinear and uncertainties is established. The parameter adaptive law is used to update the controller gain in real time to avoid the conservativeness caused by artificial setting. The obtained control input is continuous, which avoids the chatter problem of traditional sliding mode controller. The stability analysis demonstrates that the tracking error of the system converges asymptotically to an arbitrarily small range near zero in finite time, and the convergence rate and the bounds of steady-state error can be adjusted by parameters. Extensive comparative simulation and experimental results show that the proposed ASTSMC can make the position trajectory track the reference command well and satisfy the high precision control of the servo system.

6 ACKNOWLEDGEMENTS

This work is supported by the Key Science and Technology Program of Henan Province (222102220104) and the High-Level Talent Foundation of Henan University of Technology (2020BS043).

7 REFERENCES

[1] Hu, C.A., Gao, H.B, Guo, J.H., Taghavifar, H., Qin, Y.C., Na, J., Wei, C. F. (2021). RISE-based Integrated Motion Control of autonomous ground vehicles with asymptotic prescribed performance. *IEEE Transactions on Systems Man Cybernetics-Systems*, vol. 51, no. 9, p. 5336-5348, **DOI:10.1109/tsmc.2019.2950468**.

[2] Huang, Y.B., Na, J., Wu, X., Gao, G.B. (2018). Approximation-Free Control for Vehicle Active suspensions with hydraulic actuator. *IEEE Transactions on Industrial Electronics*, vol. 65, no. 9, p. 7258-7267, **DOI:10.1109/tie.2018.2798564**.

[3] Tang, Y., Zhu, Z.C., Shen, G., Rui, G.C., Cheng, D., Li, X., Sa, Y.J., (2019). Real-time nonlinear adaptive force tracking control strategy for electrohydraulic systems with suppression of external vibration disturbance. *Journal of the Brazilian Society of Mechanical Sciences and Engineering*, vol. 41, p. 1-16, **DOI:10.1007/s40430-019-1780-1**.

[4] Zhu, L.K., Wang, Z.B., Qiang, H., Liu, Y.Q. (2019). Global sliding-mode dynamic surface control for MDF continuous hot-pressing slab thickness via LESO. *International Journal of Machine Learning and Cybernetics*, vol. 10, p. 1249-1258, **DOI:10.1007/s13042-018-0804-y**.

[5] Guo, Q., Chen, Z.L. (2021). Neural adaptive control of single-rod electrohydraulic system with lumped uncertainty. *Mechanical Systems and Signal Processing*, vol. 146, p. 1-17, **DOI:10.1016/j.ymssp.2020.106869**.

[6] Guo, Q., Chen, Z. L., Shi, Y., Liu, G. (2021). Model identification and parametric adaptive control of hydraulic manipulator with neighborhood field optimization. *IET Control Theory and Applications*, vol. 15, no. 12, p. 1599-1614, **DOI:10.1049/cth2.12145**.

[7] Yang, X.W., Deng, W.X., Yao, J.Y. (2022). Neural network based output feedback control for DC motors with asymptotic stability. *Mechanical Systems and Signal Processing*, vol. 164, p. 1-15, **DOI:10.1016/j.ymssp.2021.108288**.

[8] Guo, Q., Yin, J. M., Yu, T., Jiang, D. (2017). Saturated adaptive control of an electrohydraulic actuator with parametric uncertainty and load disturbance. *IEEE Transactions on Industrial Electronics*, vol. 64, no. 10, p. 7930-7941, **DOI:10.1109/tie.2017.2694352**.

[9] Cheng, C., Liu, S.Y., Wu, H.Z. (2020). Sliding mode observer-based fractional-order proportional-integral-derivative sliding mode control for electro-hydraulic servo systems. *Proceedings of the Institution of Mechanical Engineers Part C-Journal of Mechanical Engineering Science*, vol. 234, no. 10, p. 1887-1898, **DOI:10.1177/0954406220903337**.

[10] Yin, X.X., Zhang, W.C., Jiang, Z.S., Pan, L. (2019). Adaptive robust integral sliding mode pitch angle control of an electro-hydraulic servo pitch system for wind turbine. *Mechanical Systems and Signal Processing*, vol. 133, p. 1-15 **DOI:10.1016/j.ymssp.2018.09.026**.

[11] Zhao, J.S., Wang, Z.P., Yang, T., Xu, J.X., Ma, Z.L., Wang, C.F. (2020). Design of a novel modal space sliding mode controller for electro-hydraulic driven multi-dimensional force loading parallel mechanism. *ISA Transactions*, vol. 99, p. 374-386, **DOI:10.1016/j.isatra.2019.09.018**.

[12] Jing, C.H., Xu, H.G., Jiang, J.H. (2019). Flatness-based adaptive nonlinear control for torque tracking of electro-hydraulic friction load simulator with uncertainties. *Proceedings of the Institution of Mechanical Engineers Part I-Journal of Systems and Control Engineering*, vol. 233, no. 8, p. 1009-1016, **DOI:10.1177095965181813230**.

[13] Yao, J.Y. (2018). Model-based nonlinear control of hydraulic servo systems: Challenges, developments and perspectives. *Frontiers of Mechanical Engineering*, vol. 13, no. 2, p. 179-210, **DOI:10.1080/00207170701390132**.

[14] Won, D., Kim, W., Tomizuka, M. (2017). High-gain-observer-based integral sliding mode control for position tracking of electrohydraulic servo systems. *IEEE-ASME Transactions on Mechatronics*, vol. 22, no. 6, p. 2695-2704, **DOI:10.1109/tmech.2017.2764110**.

[15] Kaddissi, C., Kenne, J. P., Saad, M. (2007). Identification and real-time control of an electrohydraulic servo system based on nonlinear backstepping. *IEEE-ASME Transactions on Mechatronics*, vol. 12, no. 1, p. 12-22, **DOI:10.1109/tmech.2006.886190**.

[16] Xin, C., Li, Y.-X., Ahn, C.K. (2022). Adaptive neural asymptotic tracking of uncertain non-strict feedback systems with full-state constraints via command filtered technique. *IEEE Transactions on Neural Networks and Learning Systems*, p. 1-6, **DOI:10.1109/tnnls.2022.3141091**.

[17] Deng, W.X., Yao, J.Y., Ma, D.W. (2017). Robust adaptive precision motion control of hydraulic actuators with valve dead-zone compensation. *ISA Transactions*, vol. 70, p. 269-278, **DOI:10.1016/j.isatra.2017.07.022**.

[18] Guo, Q., Zhang, Y., Celler, B.G., Su, S.W. (2016). Backstepping control of electro-hydraulic system based on extended-state-observer with plant dynamics largely unknown. *IEEE Transactions on Industrial Electronics*, vol. 63, no. 11, p. 6909-6920, **DOI:10.1109/tie.2016.2 585080**.

[19] Kolsi-Gdoura, E., Feki, M., Derbel, N. (2015). Position control of a hydraulic servo system using sliding mode with an integral and realizable reference compensation. *Control Engineering and Applied Informatics*, vol. 17, no. 1, p. 111-119.

[20] Liu, Y.J., Zeng, Q., Liu, L., Tong, S.C. (2020). An adaptive neural network controller for active suspension systems with hydraulic actuator. *IEEE Transactions on Systems Man Cybernetics-Systems*, vol. 50, no. 12, p. 5351-5360, **DOI:10.1109/tsmc.2018.2875187**.

[21] Hoang, Q.D., Lee, S.G., Dugarjav, B. (2019). Super-twisting observe-based integral sliding mode control for tracking the rapid acceleration of a piston in a hybrid electro-hydraulic and pneumatic system. *Asian Journal of Control*, vol. 21, no. 1, p. 483-498, **DOI:10.1002/asjc.1971**.

[22] Shao, K., Zheng, J.C., Huang, K., Wang, H., Man, Z.H., Fu, M.Y., (2020). Finite-time control of a linear motor positioner using adaptive recursive terminal sliding mode. *IEEE Transactions on Industrial Electronics*, vol. 67, no. 8, p. 6659-6668, **DOI:10.1109/tie.2019.2937062**.

[23] Van, M., Do, X. P., Mavrovouniotis, M. (2020). Self-tuning fuzzy PID-nonsingular fast terminal sliding mode control for robust fault tolerant control of robot manipulators. *ISA Transactions*, vol. 96, p. 60-68, **DOI:10.1016/j.isatra. 2019.06.017**.

[24] Palli, G., Strano, S., Terzo, M. (2018). Sliding-mode observers for state and disturbance estimation in electro-hydraulic systems. *Control Engineering Practice*, vol. 74, p. 58-70, **DOI:10.1016/j.conengprac.2018.02.007**.

Vsebina

Strojniški vestnik - Journal of Mechanical Engineering
letnik 68, (2022), številka 12
Ljubljana, december 2022
ISSN 0039-2480

Izhaja mesečno

Razširjeni povzetki (extended abstracts)

Strojniški vestnik - Journal of Mechanical Engineering 68(2022)12, SI 93

Prejeto v recenzijo: 2022-08-29
Prejeto popravljeno: 2022-10-26
Odobreno za objavo: 2022-11-03

Večciljna optimizacija mehanizma Čebišov Lambda

Daniel Miler* – Dominik Birt – Matija Hoić
Univerza v Zagrebu, Fakulteta za strojništvo in ladjedelništvo, Hrvaška

Hodni mehanizmi so rešitev za gibanje, ko kolesa niso primerna, npr. na neravnem ali stopničastem terenu oz. v prisotnosti ovir. Pot hoje takih mehanizmov je z optimizacijo tudi prilagodljiva za večjo učinkovitost v danih delovnih razmerah. Pridobivanje analitičnih rešitev v okviru optimizacije pa je lahko zamudno zaradi kompleksnosti trajektorij hodnih oz. nožnih mehanizmov. Avtorji so zato predlagali postopek za optimizacijo trajektorij posameznih nog, ki kombinira numerične izračune v Simulinku za določitev vrednosti ciljnih funkcij, te pa se nato uporabijo kot vhodi za genetski algoritem (NSGA-II) za potrebe optimizacije. Algoritem nato vrne konstrukcijske spremenljivke za novo generacijo enot (kandidatov za mehanizem) v Simulink in optimizacija se nadaljuje, dokler niso izpolnjeni pogoji za zaustavitev.

Optimizacijski postopek je bil razvit z integracijo okolja Simulink (Matlab) za numerično analizo mehanizmov ter večciljnega genetskega algoritma. Podatki o začetni populaciji so bili ustvarjeni z genetskim algoritmom (NSGA-II) in izvoženi v Simulink za izračun vrednosti ciljnih funkcij. Po ovrednotenju vseh enot v populaciji so bile ustrezne vrednosti ciljnih funkcij vrnjene v genetski algoritem in na njihovi osnovi je bila nato generirana nova generacija enot. Postopek se nadaljuje, dokler niso izpolnjeni kriteriji za zaustavitev. Vsaka enota je primerna le, če izpolnjuje vnaprej določene robne pogoje.

Kot primer za boljšo ilustracijo postopka je bil uporabljen najpreprostejši nožni mehanizem, imenovan Čebišov Lambda. Optimiziran je bil s tremi pari ciljnih funkcij: variabilnost dolžine Δx/višina, dolžina Δx/hitrostne fluktuacije in dolžina Δx/največji pospešek noge.

Rezultati kažejo, da je predstavljeni postopek z računskim časom 2 s na enoto primeren za hitro in celovito analizo kandidatnih mehanizmov. Med obravnavo rezultatov študije primera je bil največji napredek ugotovljen pri dolžini v smeri x in variabilnosti višine. Avtorji priporočajo uvedbo variabilnosti višine trajektorije za robni pogoj pri uporabi mehanizmov tipa Čebišov Lambda.

Predlagana metoda obravnava hodni mehanizem brez zajema vplivov okolice. Naprave s premikanjem na osnovi hodnih mehanizmov vključujejo več takih mehanizmov, zato je treba upoštevati tudi vpliv obratovalnih pogojev in drže (npr. dvonožni, četveronožni, šestnožni mehanizem). Pri rezultatih te študije je treba upoštevati, da je bil zajet le minimalen obseg robnih pogojev, saj so bili v središču zanimanja vplivi ciljnih funkcij na lastnosti rešitve. Nekatere Pareto rešitve bi zato privedle do neoptimalnih hodnih mehanizmov zaradi variabilnosti dolžine v smeri x.

V članku je predstavljena enostavnejša metoda za vrednotenje lastnosti trajektorij hodnih mehanizmov. Predlagani postopek poenostavlja optimizacijo in bo lahko pospešil nadaljnje raziskave hodnih mehanizmov.
Ključne besede: mehanizem Čebišov Lambda, optimizacija, sinteza, hodni mehanizem

*Naslov avtorja za dopisovanje: Univerza v Zagrebu, Fakulteta za strojništvo in ladjedelništvo, Ivana Lučića 5, 10002 Zagreb, Hrvaška, daniel.miler@fsb.hr

Strojniški vestnik - Journal of Mechanical Engineering 68(2022)12, SI 94

Prejeto v recenzijo: 2022-08-01
Prejeto popravljeno: 2022-11-10
Odobreno za objavo: 2022-11-28

Raziskava mikroobdelave nanokompozita Al/TiB_2 z lasersko ablacijo

Pratheesh Kumar Manikandan Rajam* – Jayakrishnan Nampoothiri
Tehniški kolidž PSG, Oddelek za za proizvodno strojništvo, Indija

Obdelava z laserskim žarkom (LBM) omogoča ekonomično obdelavo raznih materialov ob doseganju želenih kakovostnih kriterijev. V članku je predstavljena izdelava mikrokanalov v nanokompozitu Al/TiB_2 z laserskim sistemom Nd:YAG. Prisotnost delcev TiB_2 v aluminijasti osnovi preprečuje napredovanje dislokacij skozi faze v osnovi, s tem pa se poveča trdnost kompozitnega materiala in za odrezavanje so potrebne večje sile. Tehnologija LBM ima prednost pri obdelavi detajlov na mikroskali, saj ponuja majhno stopnjo odnašanja materiala, visoko dimenzijsko točnost in kakovostne površine. Zato je bila tudi izbrana za obdelavo mikrokanalov v kompozitu Al/TiB_2. Neustrezna izbira parametrov procesa obdelave negativno vpliva na kakovost površine lasersko obdelanih komponent.

Cilj raziskave je identifikacija vpliva vsakega parametra procesa posebej in v kombinaciji z ostalimi parametri na površinsko hrapavost mikrokanalov, kakor tudi identifikacija optimalne kombinacije parametrov procesa za minimalno površinsko hrapavost.

Eksperimenti so bili opravljeni z različnimi vrednostmi naslednjih vhodnih parametrov procesa: moč laserja, frekvenca, tlak pomožnega plina in rezalna hitrost. Površinska hrapavost mikrokanalov je bila izmerjena z mikroskopom na atomsko silo. Eksperimentalni del študije je bil zasnovan na podlagi ortogonalnega polja Taguchi L9. Pri eksperimentih je bila uporabljena kakovostna funkcija tipa »manj je več«, saj je cilj minimalna površinska hrapavost mikrokanalov. Rezultati eksperimentov so bili statistično preiskani s programsko opremo Minitab na podlagi metodologije Taguchi. Iz podatkov je bila izpeljana regresijska enačba, ki opredeljuje odvisnost med vhodnimi parametri procesa in parametrom odziva (površinska hrapavost Ra). Napovedane vrednosti površinske hrapavosti Ra so bile določene z omenjeno regresijsko enačbo. Statistična analiza je pokazala vrednost $R^2 = 95{,}13$ % in s tem visoko točnost eksperimentalnih podatkov. Glede na odstotne prispevke vhodnih parametrov po analizi ANOVA ima največji vpliv na površinsko hrapavost moč laserja. Iz grafa glavnih učinkov za srednje vrednosti **površinske hrapavosti**, pridobljenega s statistično analizo, je razvidno, da je minimalna površinska hrapavost mikrokanala dosežena pri 3. ravni rezalni hitrosti (200 mm/min), 1. ravni tlaka plina (2 bar), 2. ravni frekvence (4 kHz) in 1. ravni moči laserja (5 kW). Grafi glavnih učinkov za srednje vrednosti nakazujejo tudi trend vpliva posameznih vhodnih parametrov procesa na površinsko hrapavost. Na površinsko hrapavost pa vplivajo tudi interakcije med vhodnimi parametri procesa. Vpliv interakcij med parametri procesa na Ra v padajočem vrstnem redu moči vpliva je tak: moč/frekvenca, moč/tlak plina, frekvenca/tlak plina. Pripravljeni so bili konturni diagrami za analizo vpliva interakcij po dveh parametrov procesa na površinsko hrapavost, medtem ko preostala vhodna parametra zavzameta konstantno optimalno raven. Diagram vpliva interakcij rezalna hitrost/frekvenca impulzov na Ra kaže, da je območje minimalne površinske hrapavosti doseženo pri kombinaciji visoke frekvence impulzov in visoke rezalne hitrosti ter pri nizki frekvenci impulzov in nizki rezalni hitrosti. Prekrivanje kraterjev je odvisno od kombinacije frekvence impulzov in rezalne hitrosti. Večje kot je prekrivanje kraterjev, bolj gladka je površina reza. Zgornje kombinacije zagotavljajo visoko stopnjo prekrivanja kraterjev in zvezno gostoto moči na enoto dolžine za popolno rezanje z enakomerno in gladko površino reza. Diagram vpliva interakcij moč laserja/rezalna hitrost na Ra nakazuje, da je površinska hrapavost minimalna pri srednji ravni moči laserja in visoki rezalni hitrosti. Ta kombinacija zagotavlja ravno prav časa za delovanje laserja na material obdelovanca. Diagram vpliva interakcij rezalna hitrost/tlak plina na Ra nakazuje, da je površinska hrapavost minimalna pri kombinaciji nizkega tlaka plina in srednje rezalne hitrosti. Srednja rezalna hitrost zagotavlja dovolj dolgo izpostavitev materiala laserskemu žarku, minimalen tlak plina pa preprečuje strjevanje materiala v samem mikrokanalu za boljšo površino. Diagram vpliva interakcij frekvenca impulzov/moč laserja na Ra nakazuje, da srednja moč laserja in visoka frekvenca zagotavljata ustrezno izpostavljenost materiala laserju za minimalno hrapavost obdelane površine. Diagram vpliva interakcij tlak plina/frekvenca impulzov na Ra nakazuje, da zmeren tlak plina v kombinaciji z visoko frekvenco prav tako prispeva k ustrezni izpostavitvi obdelovanca laserju za minimalno površinsko hrapavost.

Ključne besede: laserska mikroobdelava, površinska hrapavost, nanokompozit, optimizacija parametrov, metodologija Taguchi, laser Nd:YAG

*Naslov avtorja za dopisovanje: PSG College of Technology, Coimbatore 641004, India, mrpratheesh@gmail.com

Strojniški vestnik - Journal of Mechanical Engineering 68(2022)12, SI 95

Prejeto v recenzijo: 2022-07-07
Prejeto popravljeno: 2022-10-03
Odobreno za objavo: 2022-10-17

Raziskava parametrov rezkanja tanke plošče v vpenjalu z valjastimi podpornimi glavami

Muthu Mekala Natarajan[1] – Balamurugan Chinnasamy[1] – Bovas Herbert Bejaxhin Alphonse[2]
[1] Univerza Anna, Tehniški kolidž Guindy, Indija
[2] SIMATS, Tehniška šola Saveetha, Indija

Tankostenski deli so močno razširjeni v gradbeništvu, procesni industriji, biomedicinskih instrumentih, elektroniki, avtomobilih ter v letalski in vesoljski industriji. Ti deli so med obdelavo na rezkalnih strojih podvrženi deformacijam. Glavni cilj predstavljenega raziskovalnega dela je zmanjšanje deformacij tankostenskih obdelovancev pri obdelavi na rezkalnem stroju s pomočjo predlaganega vpenjala z valjastimi podpornimi glavami.

V raziskavi so bili s steblastimi rezkarji obdelani deli iz treh različnih materialov Inconel 718, AISI 316L in Al 6061 v novem vpenjalu z valjastimi glavami, nato pa je bila opravljena primerjava površinske hrapavosti in deformacij pri različnih parametrih obdelave.

Pred eksperimenti so bile opravljene simulacije s 3D-modelom DEFORM za določitev vrednosti deformacij. Tankostenski obdelovanec iz materiala Inconel 718 je bil pritrjen na podporne glave vpenjala z različnimi orodji in podporami. Obravnavani so bili trije glavni vhodni parametri: podajanje, globina reza in hitrost. Pri eksperimentih na rezkalnem stroju s steblastimi rezkarji so bile uporabljene tri različne kombinacije vrednosti podajanja in globine reza ter različne vrednosti vrtilne frekvence vretena. Po podobnem postopku so bili obdelani tudi deli iz nerjavnega jekla AISI 316L in iz aluminijeve zlitine Al6061. Po vsakem eksperimentu so bile izmerjene vrednosti izhodnih parametrov, kot sta površinska hrapavost in odmik. Povprečna površinska hrapavost treh obdelovancev je bila izmerjena s prenosno napravo SURFTEST SJ-210. Vrednosti odmika so bile izmerjene z digitalnim merilnikom vibracij HTBB-8215.

Analiza variance (ANOVA) je razkrila vpliv posameznih spremenljivk na rezultate obdelave. Valjaste podporne glave v predlaganem vpenjalu zmanjšajo drdranje in vibracije pri rezkanju tankih plošč. Pri optimalnih vrednosti podajanja, hitrosti in globine reza se izboljša površinska hrapavost po obdelavi tankostenskih delov s steblastimi rezkarji z omejitvijo deformacij v predlaganem vpenjalu. Rezultati analize ANOVA so pokazali, da ima hitrost največji vpliv na odmik pri materialih AISI 716L in Al 6061. Podajanje ima največji vpliv na površinsko hrapavost pri materialih Inconel 718 in AISI 716L, hitrost pa ima največji vpliv na odmik in hrapavost površine pri materialu Al 6061.

Z uporabo vpenjala se znatno zmanjšajo deformacije in površinska hrapavost pri rezkanju s steblastimi rezkarji. Zasnovano in izdelano je bilo novo vpenjalo z drsnimi čeljustmi, ki zmanjšuje površinsko hrapavost obdelovancev. Eksperimentalni model je bil preverjen s tremi nivoji vhodnih parametrov podajanja, hitrosti in globine reza. Eksperimentalno določene vrednosti odmika in površinske hrapavosti se dobro ujemajo s simuliranimi vrednostmi odmika. Hitrost in podajanje imata večji vpliv kot globina reza pri zmanjševanju deformacij in površinske hrapavosti po obdelavi v predlaganem vpenjalu z valjastimi podpornimi glavami. Optimalne vrednosti parametrov podajanja, hitrosti in globine reza potrjeno izboljšajo površinsko hrapavost tankih plošč po obdelavi.

Ključne besede: obdelava s steblastim rezkarjem, vpenjalo, površinska hrapavost, deformacija, tanke plošče, parametri obdelave, odmik

*Naslov avtorja za dopisovanje: Univerza Anna, Tehniški kolidž Guindy, Indija, muthumekalagunalan@annauniv.edu

Strojniški vestnik - Journal of Mechanical Engineering 68(2022)12, SI 96

Prejeto v recenzijo: 2022-09-15
Prejeto popravljeno: 2022-11-17
Odobreno za objavo: 2022-12-16

Zasnova, izdelava in termodinamična analiza Stirlingovega motorja tipa gama na sončno energijo

Tolga Topgül*
Univerza Gazi, Oddelek za avtomobilsko strojništvo, Turčija

Onesnaževanje okolja je v zadnjih letih postalo eden od poglavitnih problemov. Med glavnimi povzročitelji tega ekološkega problema so tudi emisije motorjev z notranjim zgorevanjem. Stirlingovi motorji z zunanjim zgorevanjem so uporabna tehnologija za zmanjševanje škodljivih emisij, obratujejo pa lahko z različnimi viri toplotne energije. Uporaba Stirlingovih motorjev s sončno energijo in z drugimi obnovljivimi viri energije lahko pomaga pri zmanjševanju ogljičnega odtisa. V predstavljeni študiji je bil zato zasnovan, izdelan ter teoretično in eksperimentalno obdelan Stirlingov motor tipa gama.

Najprej je bil dvovaljni zračni V-kompresor predelan v Stirlingov motor. Izkoriščeni so bili blok motorja, ojnici in ročični mehanizem kompresorja. S samo konstrukcijo zračnega kompresorja so zato opredeljene nekatere lastnosti Stirlingovega motorja, kot so fazni kot, hod in premer valjev. Preostali deli motorja, kot so bat, glava valjev, krmilni bat in njegov valj, so bili izdelani na novo.

Predelani Stirlingov motor je bil nato preizkušen z zrakom in helijem pri različnih polnilnih tlakih. Helij v primerjavi z zrakom zagotavlja večje izboljšanje moči motorja pri vseh polnilnih tlakih. Največja moč motorja z zračno polnitvijo je znašala 9,8 W pri 123 obr./min in polnilnem tlaku 3 bar, s helijevo polnitvijo pa kar 42,5 W pri 260 obr./min in polnilnem tlaku 4 bar.

Rezultati eksperimentov s helijem pri polnilnem tlaku 2,5 bar oz. 4 bar so bili nato primerjani s teoretičnimi ugotovitvami vozliščne termodinamične analize. Eksperimentalni rezultati dajejo moč na izhodu motorja, medtem ko rezultati vozliščne termodinamične analize prikazujejo moč v valju za idealne delovne pogoje, kot so uporaba idealnega plina, popolno tesnjenje, odsotnost tlačnih padcev in druge idealne predpostavke. Rezultati teoretične analize podajajo največjo dosegljivo moč motorja oz. zgornjo mejo zmogljivosti motorja pri danih obratovalnih pogojih. V praksi je ta dosegljiva le pri brezhibnem motorju in pri popolnih obratovalnih pogojih. Eksperimenti so pokazali, da znaša maksimalna izhodna moč 20,5 W oz. 42,5 W pri polnilnem tlaku 2,5 bar oz. 4 bar. Teoretična indicirana moč v teh točkah znaša 77,1 W oz. 188,9 W.

Končno so bili preučeni še optimalni obratovalni pogoji za maksimalen toplotni izkoristek. V ta namen je bila opravljena vozliščna termodinamična analiza motorja, ki uporablja za vir toplote energijo sončnih žarkov. Za delovni medij je bil izbran helij, ki je varen in ima ustrezne termodinamične lastnosti. Za maksimalen toplotni izkoristek so bili optimizirani temperatura na vročem delu, masa delovnega medija, hitrost motorja in višina krmilnega bata. Temperaturno območje na vročem delu je bilo določeno za parabolične solarne kolektorje. Maksimalen toplotni izkoristek znaša 46,5 % pri masi delovnega medija 0,15 g, vrtilni frekvenci motorja 100 rad/s, višini krmilnega bata 190 mm in temperaturi na vročem delu 850 K. Indicirana moč v tej točki je 657,8 W. Če bi se vrtilna frekvenca motorja povišala na 300 rad/s, bi indicirana moč znašala 1141,5 W.

Teoretični rezultati tako nakazujejo, da je mogoče toplotni izkoristek izboljšati z optimizacijo obratovalnih parametrov Stirlingovega motorja. V praksi so za to potrebne še nekatere izboljšave, kot npr. zmanjšanje toplotnih, tornih in tlačnih izgub, izboljšanje učinkovitosti regeneracije in zatesnitev. Stirlingov motor mora za večjo moč obratovati z višjo vrtilno frekvenco in z najboljšo učinkovitostjo regeneratorja. Za večjo zmogljivost je treba tudi povišati temperaturo vročega dela. Končno pa so za zmanjšanje emisij ogljikovega dioksida nujni tudi do okolja prijazni viri energije. Iz navedenega sledi sklep, da se bo pomen solarnih sistemov in Stirlingovih motorjev ohranil tudi v prihodnje.

Ključne besede: Stirlingov motor tipa gama, obratovalni parametri, zmogljivost motorja, toplotni izkoristek, vozliščna termodinamična analiza, sončna energija

*Naslov avtorja za dopisovanje: Univerza Gazi, Tehnološka fakulteta, Oddelek za avtomobilski inženiring, Ankara, Turčija, topgul@gazi.edu.tr

Strojniški vestnik - Journal of Mechanical Engineering 68(2022)12, SI 97

Prejeto v recenzijo: 2022-07-14
Prejeto popravljeno: 2022-10-27
Odobreno za objavo: 2022-12-16

Adaptivno vodenje hidravličnega servoaktuatorja z nelinearnimi lastnostmi po načinu drsnega režima »super twisting«

Zhenshuai Wan[1,2*] – Yu Fu[1,2] – Longwang Yue[1] – Chong Liu[1]

[1] Tehniška univerza v Henanu, Šola za strojništvo in elektrotehniko, Kitajska
[2] Tehniška univerza v Henanu, Državni laboratorij za obdelavo in nadzor informacij o žitih, Ministrstvo za šolstvo, Kitajska

Cilj pričujočega članka je kombiniranje adaptivnega regulatorja drsnega režima vrste »super-twisting« (ASTSMC) z razširjenim opazovalnikom stanj (ESO) za kompenzacijo motenj v delovanju hidravličnega servoaktuatorja.

Pri predlagani metodi je uporabljen razširjeni opazovalnik stanj (ESO) za oceno vrednosti zbranih negotovosti. Regulator ASTSMC ne potrebuje vnaprej meja negotovosti ter poskrbi, da drseča spremenljivka in njen odvod dosežeta vrednost nič v končnem času.

Najprej je bil postavljen dinamični matematični model, ki vključuje različne nelinearnosti in negotovosti. Za posodobitve ojačenja regulatorja v realnem času je uporabljen zakon prilagoditve parametrov, s katerim se je mogoče izogniti konzervativnim umetnim nastavitvam. Vodilni signal regulatorja je zvezen, s čimer so odpravljene težave s poskakovanjem pri klasičnih regulatorjih drsnega režima. Analiza stabilnosti je pokazala, da napaka sledenja sistema v končnem času asimptotično konvergira v poljubno majhno območje okrog ničle, stopnjo konvergence in meje stacionarne napake pa je mogoče prilagoditi z izbiro parametrov.

Rezultati simulacij in eksperimentov nakazujejo, da predlagani regulator ASTSMC učinkovito obvladuje zbrane negotovosti in jasno izboljša zmogljivost sledenja.

Dinamične omejitve stanj in problem omejitev izhoda zaradi fizikalnih danosti in zahtev glede delovanja hidravličnega sistema bodo predmet prihodnjih študij.

Razširjeni opazovalnik stanj (ESO) je bil uporabljen za oceno neizmerjenega stanja sistema in zbranih negotovosti. Regulator ASTSMC je bil prilagojen za kompenzacijo motenj in dodatno izboljšanje točnosti sledenja.
Ključne besede: hidravlični servoaktuator, nelinearne lastnosti, negotovosti pri modeliranju, vodenje po načinu drsnega režima »super-twisting«, razširjeni opazovalnik stanj, adaptivna regulacija

*Naslov avtorja za dopisovanje: Tehniška univerza v Henanu, Šola za strojništvo in elektrotehniko, Zhengzhou, 450001, Kitajska, wanzhenshuai@haut.edu.cn

Guide for Authors

All manuscripts must be in English. Pages should be numbered sequentially. The manuscript should be composed in accordance with the Article Template given above. The suggested length of contributions is 10 to 20 pages. Longer contributions will only be accepted if authors provide justification in a cover letter. For full instructions see the Information for Authors section on the journal's website: http://en.sv-jme.eu .

SUBMISSION:

Submission to SV-JME is made with the implicit understanding that neither the manuscript nor the essence of its content has been published previously either in whole or in part and that it is not being considered for publication elsewhere. All the listed authors should have agreed on the content and the corresponding (submitting) author is responsible for having ensured that this agreement has been reached. The acceptance of an article is based entirely on its scientific merit, as judged by peer review. Scientific articles comprising simulations only will not be accepted for publication; simulations must be accompanied by experimental results carried out to confirm or deny the accuracy of the simulation. Every manuscript submitted to the SV-JME undergoes a peer-review process.

The authors are kindly invited to submit the paper through our web site: http://ojs.sv-jme.eu. The Author is able to track the submission through the editorial process - as well as participate in the copyediting and proofreading of submissions accepted for publication - by logging in, and using the username and password provided.

SUBMISSION CONTENT:

The typical submission material consists of:

- A **manuscript** (A PDF file, with title, all authors with affiliations, abstract, keywords, highlights, inserted figures and tables and references),
- Supplementary files:
  - a **manuscript** in a WORD file format
  - a **cover letter** (please see instructions for composing the cover letter)
  - a ZIP file containing **figures** in high resolution in one of the graphical formats (please see instructions for preparing the figure files)
  - possible **appendicies** (optional), cover materials, video materials, etc.

Incomplete or improperly prepared submissions will be rejected with explanatory comments provided. In this case we will kindly ask the authors to carefully read the Information for Authors and to resubmit their manuscripts taking into consideration our comments.

COVER LETTER INSTRUCTIONS:

Please add a **cover letter** stating the following information about the submitted paper:

1. Paper **title**, list of **authors** and their **affiliations**. **One** corresponding author should be provided.
2. **Type of paper**: original scientific paper (1.01), review scientific paper (1.02) or short scientific paper (1.03).
3. A **declaration** that neither the manuscript nor the essence of its content has been published in whole or in part previously and that it is not being considered for publication elsewhere.
4. State the **value of the paper** or its practical, theoretical and scientific implications. What is new in the paper with respect to the state-of-the-art in the published papers? Do not repeat the content of your abstract for this purpose.
5. We kindly ask you to suggest at least two **reviewers** for your paper and give us their names, their full affiliation and contact information, and their scientific research interest. The suggested reviewers should have at least two relevant references (with an impact factor) to the scientific field concerned; they should not be from the same country as the authors and should have no close connection with the authors.

FORMAT OF THE MANUSCRIPT:

The manuscript should be composed in accordance with the Article Template. The manuscript should be written in the following format:

- A **Title** that adequately describes the content of the manuscript.
- A list of **Authors** and their **affiliations**.
- An **Abstract** that should not exceed 250 words. The Abstract should state the principal objectives and the scope of the investigation, as well as the methodology employed. It should summarize the results and state the principal conclusions.
- 4 to 6 significant **key words** should follow the abstract to aid indexing.
- 4 to 6 **highlights;** a short collection of bullet points that convey the core findings and provide readers with a quick textual overview of the article. These four to six bullet points should describe the essence of the research (e.g. results or conclusions) and highlight what is distinctive about it.
- An **Introduction** that should provide a review of recent literature and sufficient background information to allow the results of the article to be understood and evaluated.
- A **Methods** section detailing the theoretical or experimental methods used.
- An **Experimental section** that should provide details of the experimental set-up and the methods used to obtain the results.
- A **Results** section that should clearly and concisely present the data, using figures and tables where appropriate.
- A **Discussion** section that should describe the relationships and generalizations shown by the results and discuss the significance of the results, making comparisons with previously published work. (It may be appropriate to combine the Results and Discussion sections into a single section to improve clarity.)
- A **Conclusions** section that should present one or more conclusions drawn from the results and subsequent discussion and should not duplicate the Abstract.
- **Acknowledgement** (optional) of collaboration or preparation assistance may be included. Please note the source of funding for the research.
- **Nomenclature** (optional). Papers with many symbols should have a nomenclature that defines all symbols with units, inserted above the references. If one is used, it must contain all the symbols used in the manuscript and the definitions should not be repeated in the text. In all cases, identify the symbols used if they are not widely recognized in the profession. Define acronyms in the text, not in the nomenclature.
- **References** must be cited consecutively in the text using square brackets [1] and collected together in a reference list at the end of the manuscript.
- **Appendix(-icies)** if any.

SPECIAL NOTES

Units: The SI system of units for nomenclature, symbols and abbreviations should be followed closely. Symbols for physical quantities in the text should be written in italics (e.g. *v*, *T*, *n*, etc.). Symbols for units that consist of letters should be in plain text (e.g. ms^{-1}, K, min, mm, etc.). Please also see: http://physics.nist.gov/cuu/pdf/sp811.pdf .

Abbreviations should be spelt out in full on first appearance followed by the abbreviation in parentheses, e.g. variable time geometry (VTG). The meaning of symbols and units belonging to symbols should be explained in each case or cited in a **nomenclature** section at the end of the manuscript before the References.

Figures (figures, graphs, illustrations digital images, photographs) must be cited in consecutive numerical order in the text and referred to in both the text and the captions as Fig. 1, Fig. 2, etc. Figures should be prepared without borders and on white grounding and should be sent separately in their original formats. If a figure is composed of several parts, please mark each part with a), b), c), etc. and provide an explanation for each part in Figure caption. The caption should be self-explanatory. Letters and numbers should be readable (Arial or Times New Roman, min 6 pt with equal sizes and fonts in all figures). Graphics (submitted as supplementary files) may be exported in resolution good enough for printing (min. 300 dpi) in any common format, e.g. TIFF, BMP or JPG, PDF and should be named Fig1.jpg, Fig2.tif, etc. However, graphs and line drawings should be prepared as vector images, e.g. CDR, AI. Multi-curve graphs should have individual curves marked with a symbol or otherwise provide distinguishing differences using, for example, different thicknesses or dashing.

Tables should carry separate titles and must be numbered in consecutive numerical order in the text and referred to in both the text and the captions as Table 1, Table 2, etc. In addition to the physical quantities, such as *t* (in italics), the units [s] (normal text) should be added in square brackets. Tables should not duplicate data found elsewhere in the manuscript. Tables should be prepared using a table editor and not inserted as a graphic.

REFERENCES:

A reference list must be included using the following information as a guide. Only cited text references are to be included. Each reference is to be referred to in the text by a number enclosed in a square bracket (i.e. [3] or [2] to [4] for more references; do not combine more than 3 references, explain each). No reference to the author is necessary.

References must be numbered and ordered according to where they are first mentioned in the paper, not alphabetically. All references must be complete and accurate. Please add DOI code when available. Examples follow.

Journal Papers:

Surname 1, Initials, Surname 2, Initials (year). Title. *Journal*, volume, number, pages, DOI code.

[1] Hackenschmidt, R., Alber-Laukant, B., Rieg, F. (2010). Simulating nonlinear materials under centrifugal forces by using intelligent cross-linked simulations. *Strojniški vestnik - Journal of Mechanical Engineering,* vol. 57, no. 7-8, p. 531-538, DOI:10.5545/sv-jme.2011.013.

Journal titles should not be abbreviated. Note that journal title is set in italics.

Books:

Surname 1, Initials, Surname 2, Initials (year). Title. Publisher, place of publication.

[2] Groover, M.P. (2007). *Fundamentals of Modern Manufacturing*. John Wiley & Sons, Hoboken.

Note that the title of the book is italicized.

Chapters in Books:

Surname 1, Initials, Surname 2, Initials (year). Chapter title. Editor(s) of book, book title. Publisher, place of publication, pages.

[3] Carbone, G., Ceccarelli, M. (2005). Legged robotic systems. Kordić, V., Lazinica, A., Merdan, M. (Eds.), Cutting Edge Robotics. Pro literatur Verlag, Mammendorf, p. 553-576.

Proceedings Papers:

Surname 1, Initials, Surname 2, Initials (year). Paper title. Proceedings title, pages.

[4] Štefanić, N., Martinčević-Mikić, S., Tošanović, N. (2009). Applied lean system in process industry. *MOTSP Conference Proceedings*, p. 422-427.

Standards:

Standard-Code (year). Title. Organisation. Place.

[5] ISO/DIS 16000-6.2:2002. *Indoor Air – Part 6: Determination of Volatile Organic Compounds in Indoor and Chamber Air by Active Sampling on TENAX TA Sorbent, Thermal Desorption and Gas Chromatography using MSD/FID.* International Organization for Standardization. Geneva.

WWW pages:

Surname, Initials or Company name. Title, from http://address, date of access.

[6] Rockwell Automation. Arena, from *http://www.arenasimulation.com,* accessed on 2009-09-07.

EXTENDED ABSTRACT:

When the paper is accepted for publishing, the authors will be requested to send an **extended abstract** (approx. one A4 page or 3500 to 4000 characters or approx. 600 words). The instruction for composing the extended abstract are published on-line: http://www.sv-jme.eu/information-for-authors/ .

COPYRIGHT:

Authors submitting a manuscript do so on the understanding that the work has not been published before, is not being considered for publication elsewhere and has been read and approved by all authors. The submission of the manuscript by the authors means that the authors automatically agree to publish the paper uder CC-BY 4.0 Int. or CC-BY-NC 4.0 Int. when the manuscript is accepted for publication. All accepted manuscripts must be accompanied by a Copyright Agreement, which should be sent to the editor. The work should be original work by the authors and not be published elsewhere in any language without the written consent of the publisher. The proof will be sent to the author showing the final layout of the article. Proof correction must be minimal and executed quickly. Thus it is essential that manuscripts are accurate when submitted. Authors can track the status of their accepted articles on https://en.sv-jme.eu/.

PUBLICATION FEE:

Authors will be asked to pay a publication fee for each article prior to the article appearing in the journal. However, this fee only needs to be paid after the article has been accepted for publishing. The fee is 380 EUR (for articles with maximum of 6 pages), 470 EUR (for articles with maximum of 10 pages), plus 50 EUR for each additional page. The additional cost for a color page is 90.00 EUR (only for a journal hard copy; optional upon author's request). These fees do not include tax.

9 770039 248001
ISSN 0039-2480

http://www.sv-jme.eu

Contents

Papers